Imperial College London

Imperial College London

Doctoral Thesis

Sumbitted in partial fulfillment of the requirements for the award of Doctor of Philosophy of Imperial College London

Topics in Complex Multiscale Systems: Theory and Computations of Noise-Induced Transitions and Transport in Heterogenous Media

Douglas Addy

supervised by
Prof. Serafim Kalliadasis

April 30, 2019

Declaration of Authorship

I, Douglas Addy, declare that the thesis titled, "**Topics in Complex Multiscale Systems: Theory and Computations of Noise-Induced Transitions and Transport in Heterogenous Media**" and the work presented herein are my own. I confirm that:

- This work was done wholly while a candidate for a research degree at this University.
- Where any part of this work has previously been submitted as part of an examination for a degree or any other qualification at this University or another institution, this has been clearly indicated.
- Where I have consulted the published work of others, this is clearly attributed.
- Where I have quoted from the work of another, the source is always given. With the exception of such quotations this thesis is entirely my own work.
- I have acknowledged all major sources of assistance.
- Where this thesis is based on work done jointly with with others, I have made clear which work was done by myself and which was contributed by others.

Signed:_____
Date:_____

Declaration of Copyright

Abstract

The present work seeks to address three different problems that have a multiscale nature, we apply different techniques from multiscale analysis to treat these problems.

We introduce the field of multiscale analysis and motivate the need for techniques to bridge between scales, presenting the history of some common methods, and an overview of the current state of the field.

The remainder of the work deals with the treatment of these problems, one motivated by reaction rate theory, and two from multiphase flow. These superficially have little relation with each other, but the approaches taken share similarities and the results are the same - an average picture of the microscopic description informs the macroscale.

In Chapter 2 we address an asymmetric potential with a microscale, showing that the interaction between this microscale and the noise causes a first-order phase transition. This induces a metastable state which we observe and characterise: showing that the stability of this state depends on the strength of the tilt, and that the phase transition is inherently different to the symmetric case.

In Chapter 3 we investigate the nucleation and coarsening process of a two-phase flow in a corrugated channel using a Cahn–Hilliard Navier–Stokes model. We show that several flow morphologies can be present depending on the channel geometry and the initial random condition. We rationalise this with a static energy model, predicting the preferential formation of one morphology over another and the existence of a first-order phase-transition from smooth slug flow to discontinuous motion when the channel is strongly corrugated.

In Chapter 4 we address a model for interfacial flows in porous geometries, formulating an finite-element model for the equations. Within this framework we solve two equations in the microscale to obtain effective coefficients decoupling the two scales from each other. Finite-difference simulations of the macroscopic flow recover results from literature, supporting robustness of the method.

Acknowledgements

This work, representing the culmination of the author's time at Imperial College London, owes its existence to a great many people:

Firstly to Prof. Serafim Kalliadasis, for support, mentoring and for asking the difficult questions. Also for introducing me to research initially and for providing me the opportunity to study demanding problems.

To members of my research group, both current and former, for support, advice, questions and explanations. My particular thanks to Dr. Marc Pradas for his time and valuable contributions to analysis and data presentation, to Dr. Petr Yatsyshin for stimulating conversations and help with visualisation and to Dr. Ben Aymard for his insights and advice on numerical methods.

To the students, volunteers, and staff who make and support music and the arts, you make the College a better place, I cannot overstate the effect you all have on students and staff.

To Laura, for without your unstinting love, support and encouragement, without your cheerleading and advice this would not have been possible.

To my parents for your support, comments, advice and guidance throughout my academic career.

I owe it to you all.

Douglas Addy

Contents

List of Figures

List of Tables

1 Introduction

Problems with multiple scales appear in all branches of science and engineering, whether it is multiple time scales in the presentation of television pictures that allow us to see a smoothly moving image, or the huge range of scales in fluid motion that allow the continuum approximation to be used to model flow. These scales can be both a blessing and a curse; in a CRT TV, for example, we cannot perceive the fastest scales corresponding to the raster rate; rather, we only perceive the image changing smoothly. In turbulent flow, however, the presence of an extensive chain of scales within turbulence makes modelling and simulating the behaviour of flows with high Reynolds numbers very difficult.

Exactly when multi-scale methods first came about is a question that is difficult to answer, but a clear avenue of study began in the late 17th century when astronomers observed that the planets did not move through space on exact ellipses [183]. This problem was important and relevant because navigation relied on the accurate determination of the position of stars, and if the Earth did not move along a perfect ellipse then travellers the world over were relying on incorrect positional information.

Including the effect of the Moon renders the equations of motion impossible to solve analytically. Euler proposed a procedure to deal with this problem, using the existing solution for the motion of the Earth and deriving a reduced-order approximation for the perturbation caused by the Moon. This resulted in a more accurate expression for the distance of the Earth-Moon barycentre from the elliptic, and hence more reliable and accurate information for navigators [64] [as cited in [183]].

$$2\mathrm{d}r\mathrm{d}\phi + r\mathrm{d}^2\phi = -\frac{1}{2}n\mathrm{d}t^2 \sin\theta \tag{1.1}$$

where r is the Earth-Moon distance, ϕ the phase, $\mathrm{d}t$ the time derivative, n the centripetal force strength and θ represents a small perturbation in the centripetal force.

Through assumptions on the motion of the Earth (either circular or elliptical,

and free from perturbation), he could solve Equation 1.1. A similar method was used to estimate the rate of elongation of the tropical year, which was measured (spuriously) by many astronomers at the time [183].

Other work was done by Clairault, Laplace and Lagrange to varying degrees of technicality and clarity throughout the latter half of the 18th century. Lagrange presents a transparent approach in his work 'Analytical Mechanics' ('Mechanique Analytique') [120] [as cited in [159]], wherein he presents most of the elements required for perturbation expansions and the averaging of ordinary differential equations (ODEs).

The driving force for the method of homogenisation, however, came from the study of materials science. With the development in the 20th century of composite materials like fibreglass, carbon fibre and reinforced concrete, there was a drive to improve modelling of these materials. Homogenisation began as a formal method for the reduction in the number of modelled scales which required proof of convergence in each application [18].

Not only does homogenisation allow for the study of the effect of reinforcement or voids in materials [85, 104], but in many cases numerical solution is made much faster as the short or fast scale tends to limit time steps in many simulations [35].

At the heart of homogenisation is the idea that when a series of scales exist, we would like to describe the behaviour of a system using only some of them. We would therefore like to extract some information from the scales that we want to discard without solving the equations in full.

Formally, if it is possible to take a family of differential operators L_ϵ with corresponding solutions u_ϵ for some spatial variable with multiple scales x_ϵ in some region Ω that satisfies:

$$L_\epsilon u_\epsilon = f \quad \forall x_\epsilon \subset \Omega \tag{1.2}$$

Then we can prove that this sequence converges in some sense to a so-called homogenised operator $\bar{L}$ and solution $\bar{u}$ for a spatial variable in one scale x:

$$\bar{L}\bar{u} = f \quad \forall x \subset \Omega \tag{1.3}$$

The form of this convergence and its proof depend on the nature of the equations, which we initially take to be spatially periodic. We can then use the method of two-scale convergence from [3] which finds the correct homogenised equation and proves convergence in one step.

1.1 Literature Review

As the field of Multiscale Methods is vast, and any attempt to summarise the state of the field would be futile, we would direct the reader, for a general review, to [54] and [131]. Horstmeyer refers to a process he calls bridging [95], and this covers most methods of interest.

1.1.1 Introduction to Different Approaches - Analytical Methods

Perturbation Methods and ODE Averaging

Historically the first approaches that are widely regarded to make use of multiple scales are perturbation methods. When it is clear that the dynamics of a system are dominated by one contribution, the simplest approach is to neglect other smaller contributions and create a "first-order" solution. When more accurate models are required, the smaller contributions must be taken into account: if these prove impossible to treat exactly then perturbation approaches can offer valuable insight. Beginning from the first-order solution, one can introduce small corrections to the governing equations and determine their effects on the solution obtained.

Subsequent development of these approaches led to the fields of Averaging and Homogenization. For ordinary differential equations (ODEs) the more general framework of Averaging allows a more flexible treatment of microscales, from very accurate treatments that are only valid for short times, to less accurate expressions that are valid for longer times. This is the characteristic trade-off of the Averaging method.

Classical perturbation theory has a wide range of books and review articles for introduction. Sanders [159] offers a clear introduction; Bender and Orszag offer much more of the mathematical background for many of these methods [17]; whilst Hinch offers an introduction that omits some of the mathematical details in favour of readability [91].

Asymptotic Expansions and Homogenization

When no one scale clearly dominates everywhere, but the number of scales or regions of distinct behaviour are small, one approach is to make use of asymptotic expansions; the so-called "Method of Matched Asymptotics" allowed Prandtl to develop an understanding of the structure of boundary layers in fluid flow problems. Recognising that the qualitative behaviour of a fluid is different close to a wall than far in the bulk, one can develop different asymptotic expansions in these two regions. These expressions are then assumed to match at some intermediate point. Careful consideration of scaling arguments in each region allow this matching process to provide a full solution in the region.

Within the literature, Hunter offers a good introduction to Perturbation Theory and the details of the Matching process [99], whilst Holmes gives a more in-depth treatment of Asymptotic Matching and more involved regimes, like corner matching [93]. Prandtl's treatment of aerodynamic boundary layers is a classical application of this method (see [7] for a review), but recent examples include matching in the Moving Contact Line problem [163], in thin film flow [105] and in acoustics [136].

When extending perturbation results for partial differential equations (PDEs) the field of Homogenization was popularized. When the coefficients within the

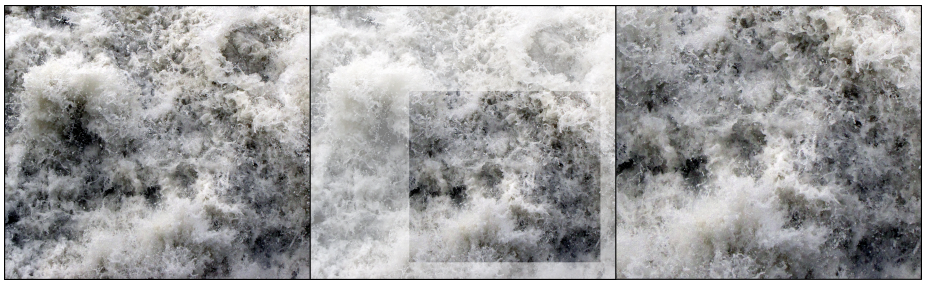

Figure 1.1: Example of self-similarity in turbulent fluid flow: The right panel is a scaled section of the left panel; the fluid looks qualitatively similar. In a similar sense the energy dissipation of fluid in the scaled section is identical to fluid in the original image. This is the basis of Kolmogorov's arguments. Image by Steven Mathey - Own work, CC BY-SA 4.0, https://commons.wikimedia.org/w/index.php?curid=45053551

equations oscillate rapidly it is desirable to avoid solving them directly (particularly given the implications for mesh and time-step size when solving numerically). To that end, homogenization formalizes the process of smoothing out these oscillations, making use of asymptotic expansions and correcting the "smoother" equations to account for the discarded information.

Homogenization is rather a technical subject, but [149] would be a good entry point to the field. Bensoussan et al. offer many of the original derivations and details in their classic text [18] which may help to augment the history of the field [159].

Self-Similar Analysis

A more modern approach that can be applicable in problems with many separate or even a continuous cascade of scales makes use of self-similarity. If the assumption can be justified that the intermediate scales are similar (when scaled their governing equations are the same) then the macroscopic equations can be corrected with effective contributions from the cascade of similar scales: these are normally found by solving a set of differential equations which may or may not permit closed-form solutions.

The most celebrated example of the application of Self-Similarity to multiscale problems is arguably Kolmogorov's classic treatment of turbulence [113]. In it he suggested that in the range of intermediate length scales the only important quantity was the mean energy dissipation rate (Figure 1.1). Through a dimensional argument he arrived at an expression for the kinetic energy density as a function of the wavenumber.

The technique has applications for PDEs that model other physical behaviour, including flow through porous solids and semi-linear heat transfer [77], but a general characteristic is the presence of extreme regions (macroscale or a finite smallest scale) with an intermediate regime. One example from astro-

physics is Narayan and Li's work on accretion [135]; they derive a self-similar solution giving insight into behaviour of hot accretion disks. In optics Kruglov et al. [117] find a self-similar solution for optical fibre amplification which gave insight into producing chirp-free pulses for data transmission.

1.1.2 Introduction to different approaches - Numerical Methods

When no analytical methods exist that permit the solution of complex problems then numerical methods must be deployed. Since the advent of scientific computing much effort has been spent developing approaches to accelerate solution of problems with multiple scales. The main driving force is the implications that oscillatory or microscopic terms have on the mesh-size and time-step requirements - the mesh must be fine enough to resolve the smallest details that are physically relevant, and the time-step is intrinsically linked to the stability of the numerical scheme.

Multi-Physics Methods

One approach has been to take a known microscale simulation such as Molecular Dynamics (MD) and use it to provide coefficients or constitutive relations for a different macroscale solver. Three methods that make use of this idea are "Equation-Free Computing", something of a misnomer, the Multi-Grid Method and the Heterogeneous Multiscale Method (HMM).

Equation-Free Computing [108] is an example of the former, where microscopic simulations are used to predict the evolution of macroscopic variables. This means that systems can be modelled with no knowledge of the macroscopic equations governing the process at all. E provides a good summary of the current gaps in this approach [55]; however, both the time acceleration scheme (projection) and the spatial discretization scheme (patching) require assumptions about the problem that cannot be known a-priori.

A more established algorithm with a similar idea is the so-called 'multi-grid' method, which is used to accelerate the solution of PDEs. When solving PDEs with an iterative method, the mesh and time-step size is limited by the fastest scale in the problem; however, the number of iterations required increases as the mesh size increases. In essence, the time-step is controlled by the fastest scales, whilst the length of the simulation is controlled by the slowest scales.

The principle of this method is to solve the problem on several different grid sizes, such that the slowest modes decay quickly on the coarse grid, whilst the finer grids resolve more detail and increase the useable time-step. The main sources of difficulty with multi-grid are the 'prolongation' and 'restriction' operations that link the different scales and the cost of storing the separate meshes (typically three or four levels) (Figure 1.2). Briggs et al. [26] provide an accessible introduction to the method and a very intuitive explanation of its damping properties. Also, [54] provides a terse summary.

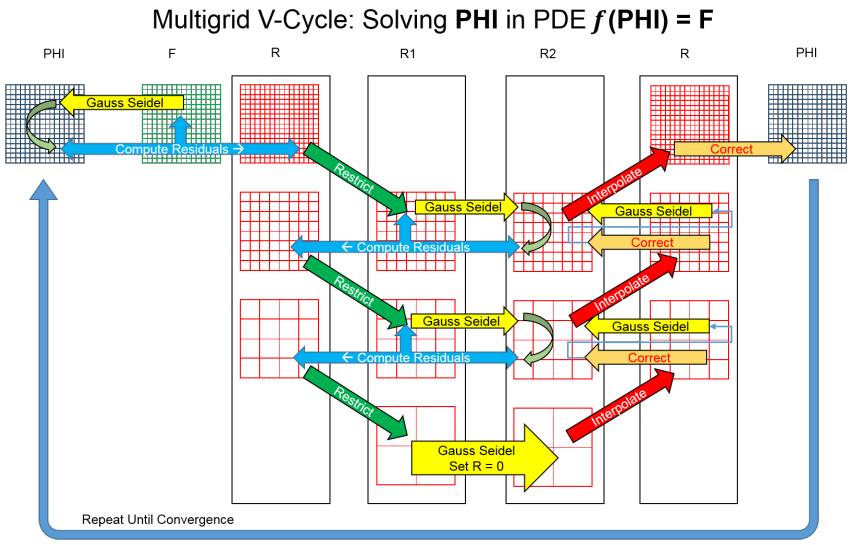

Figure 1.2: Visualization of the Multigrid Method: Initial solution ϕ is smoothed using Gauss–Siedel or similar to produce F, the residual of this process is computed on the original mesh (top panel of left R). Restriction is then performed, sampling the residual on the coarser grid (top panel of R1). The process is then repeated until the coarsest grid is achieved (bottom panel of R1). The coarse residual is then upsampled in a process called Prolongation to a finer mesh (bottom panel of right R), this corrects error in the corresponding finer residual and after smoothing the process repeats until the finest mesh is reached (top panel of right R). This process is iterated until a solution is reached. (Image by ansariddle - Own work, CC BY-SA 4.0, https://commons.wikimedia.org/w/index.php?curid=52309844)

There is also the Heterogeneous Multiscale Method (HMM), which uses microscopic simulation to provide the parameters for the macro-scale solver. It shares some of the shortcomings of the Equation-Free approach, requiring a careful choice of macro-scale solver, and does not make use of patch dynamics. That said, much more work has been done with HMM than with Equation-Free (see section 6.4.2 in [54])

Other Bridging Methods

Another promising avenue that links different solvers together involves linking MD and Dynamic Functional Theory (DFT). Since DFT makes use of assumed particle interactions, it is an attractive target for MD simulations. Extraction of the interaction parameters required for a DFT simulation could be done a-priori, leaving only the "macroscale" solution to be done for the problem. This

approach was initially popularised by Car and Parinello [31], a good introduction to the method is given by Gianozzi [75] and good examples of applications for this method come from biology, with Andreoni reviewing the field in 2001 [8].

More recently, there has been work (within this department) to link MD simulations of vapour-liquid equilibria with Dynamic DFT (DDFT) to model contact line movement [186].

Alternative approaches for computing the quantites for DFT exist. As an example, the fast multipole method (FMM) was designed to enable the fast summation of point-wise particle interactions. This problem appears in a wide range of contexts, from celestial mechanics to quantum electrodynamics. In FMM the summation is approximated by grouping points that are 'far' from the test point, and approximating their interaction as a single force. This reduces the operation count from $O(N^2)$ to $O(N \log N)$ or even $O(N)$ [15], and reduces the amount of memory required to solve the problem [144]. Recent applications of FMM include acoustics (by linking with the Boundary Element Method [102]) [182], quantum molecular dynamics [162] and elasticity [175].

Within the field of complex fluids, the "Brownian Dynamics Method" uses continuum theory to model polymeric solutions. In order to obtain the stress, polymer chain interactions are modelled with a stochastic force; see for example [19] for early work in the field, [100] for simulations in domains with obstacles and [32] for applications to different polymer shapes. Clearly, the simplicity of the model used in the micro-scale impacts the convergence behaviour and speed of the simulation, but for most dilute polymers Carlsson finds that the simple dumbbell or short chain models offer good results [32].

Moving Contact Line Problem

An excellent example of a problem that has been extensively studied and that is undergoing a revival is the Moving Contact Line problem. Classical Navier–Stokes analysis leads to a singularity at the contact line when a no-slip condition is imposed [98]. Many solutions have been proposed to resolve this, with varying degrees of physical justification and many review articles discussing the relative merits. A recent review in this field is by Bonn et al. [23], and they cite previous reviews back to the 1980s. Verlarde et al. [173] present a discussion article which covers the current field, as well as the debate still raging.

In the absence of an accepted explanation for the phenomena based on physics, many authors have turned to either MD or Phase-Field models to investigate the behaviour at the contact line. Phase-Field models have been used to reproduce physical behaviour in both spreading and receding, and in 'rolling motion' [164], as well as for more complex situations including droplet growth and 'pinch-off' [50]. Despite the success shown by these models they require parameters such as the interface width, which the model should ideally provide.

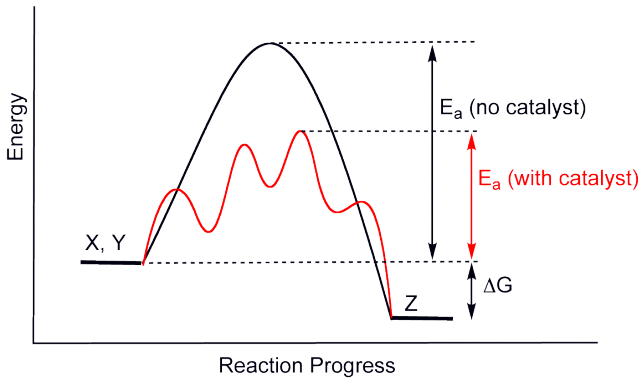

Figure 1.3: Example diagram showing Chemical Potential Energy against Reaction Coordinate: The initial state (X+Y) is energetically less favourable than the final state (Z), so the reaction will occur; the energy barrier between the two states controls the rate of reaction. In this case the catalyst reduces the energy barrier (E_a) and so the reaction rate will be faster. Studying the long-term behaviour of this system enables chemists to predict the amount of side-products (the intermediate minima), or reactants (X, Y) will be present after the reaction is allowed to occur. (Public Domain)

1.1.3 Brownian Motion in Potential Fields

Early Work–Chemical Kinetics

The confinement of particles to potential fields has a wide range of practical applications and has been well studied. Early work on the problem came from the study of nucleation and from chemical kinetics; perhaps the first analysis was by Farkas in 1927 [65], who was interested in the rate of nucleation in saturated steam. He solved the over-damped expression to obtain the current across a potential barrier in general terms. Pontryagin et al. were interested in chemical kinetics in 1933 [150] and provided the first mention and calculation of the First Passage Time. Other work in the same vein was done by Becker and Döring in 1935 [16], who gave their names to a series of equations that can be used to model phase separation.

It is perhaps a shame that it is Kramers who gets most of the credit for the early study of these systems, but he re-derived the overdamped case, admittedly with less generality, and managed to obtain a solution in the under-damped case [116] through some elegant maths which Hänggi calls 'almost acrobatic' [89]. His result was also the first to propose applications to chemical reactions, although it would be many years before applications became obvious (Figure 1.3).

In 1949 Moyal published an early review of the field of statistical physics and proposed what we now call the Kramers–Moyal (K-M) expansion as a method for analysing the behaviour of Markov chains. They showed that this reduces to the Fokker–Planck equation (FPE) when truncated and Moyal recognises

the difficulty in treating these equations in their entirety [134]. That said, the treatment of the Master Equation was to form a fruitful area of study throughout the 20th century.

Lax and van Kampen made attempts in the 1960s to systematically approximate solutions to the master equations, with Lax expanding in "orders of nonlinearity" [124], whilst van Kampen expands in terms of the reciprocal of the size of the system, achieving agreement with previous work for small noise in his examples [172]. Either method facilitated the computation of the statistical moments of the probability density function, which were the best way to study the systems at the time.

New Applications: Electronics and Optics

Applications for the results generated were still thin on the ground, but in the early 1960s Landauer and Swanson at IBM published a series of papers which not only examined transition rates and most likely states, but also investigated relaxation times in memory design and tunnel diode behaviour [168, 122, 121] in increasing sophistication. The first paper is accessible to a reader with a limited background in physics and adopts an intuitive explanation for the transition rate, whilst the latter two are more rigorous.

Early work in laser physics was carried out by Risken, amongst others, but he was the first to include noise in a full nonlinear model for a laser cavity [155]. He obtained solutions by taking limits which were physically realisable. Subsequent work by the same author extended these results, finding correlation functions in more useful regimes [156].

It was the in 1970s that widespread applications of noisy bistable systems first appeared. Chemical reactions that undergo state transitions were studied by Nitzan et al., who recognised that van Kampen's approach was invalid because the noise could not be assumed small [140]; they managed to solve the master equations in their entirety for two simple systems. A similar problem was studied by Matheson et al., but they simply neglected high order terms in the K-M equations to derive an FPE, justifying this with scaling arguments [130].

Haken played a huge role in the early 1970s in the justification of the detailed balance in models, together with the requirements on FPE coefficients to keep the balance valid. He provides a review of many different systems in his article, together with references to a number of his papers from the previous years [86]. He gives examples from hydrodynamics, a review of tunnel diodes and the Gunn effect in plasma physics, together with a good background of the theory at the time.

Nonlinear optics provided examples in the field as well with an optical bistability studied by Bonifacio and Lugiato [22], who gave a noisy quantum mechanical model for the phenomenon utilising the Kramers Approximation, which appears to be reasonable as their potential is smooth. The 1970s also began the study of neuronal behaviour, with studies by Wilson and Crown (see refs. in [86])

Technical Advances – Approximations to the Master Equation

At the same time there was renewed interest in the mathematics of the problem, with much work being done on the well relaxation time or the decay rate from metastable states. Kubo et al. base their analysis on the K-M expansion and recognise that this limits its applicability, but they find the rate and spectrum of relaxation in several example problems [118]. Meanwhile, Grabert et al. recognised that the Markov assumption was invalid for most physical systems, so set about studying the master equations for non-Markovian processes; they found a transform that turns a physical process into an exact Markov process [80, 81].

Further insights into the validity (or not) of the FPE came from Hänggi, who used Semi-Group analysis to study which families of stochastic processes admit closed form solutions [87]. On this basis, and with numerical agreement from many sources [130, 86, 94], he argued that the non-linear FPE was a consistent approximation to the Master Equation, whilst van Kampen disagreed strongly [87] (see ref. 27 in that article).

Further work on relaxation from instability followed into the early 1980s with Suzuki studying the central regime (the scaling region), where he improves on the results from the Ω expansion of van Kampen. Incidentally, he shows that at least for short times the FPE has the correct asymptotic behaviour in this case (he refers to this as the initial region) [167]. Caroli et al. confirm this scaling regime in a quartic potential by applying the WKB method and subsequently through a Functional Integral approach, but find that there is more to the intermediate time than just Suzuki's regime [33, 34].

A major shortcoming in the recognition of the central scaling regime was the lack of a clear time when the central scaling and Kramers regime should match. Hu and Zheng recognised this and proposed the use of a different scaling, which alleviated the problem [96]. They provide numerical results that show good agreement between their solution and the exact solution at long times, whilst showing that naïve scaling theory leads to greater deviations. This approach was also taken by Weiss, who derived an expression valid in all regimes by using a path integral formulation; he claims agreement with a mode decomposition calculation, although the reference is unpublished, but he does recover classical results for occupation probability [179].

Early progress on the periodic case was made by Ambegaokar and Halperin, who formulated a model for the Josephson effect and solved it in the limit of large damping to obtain approximate flux [6], their expression being an integral which required numerical evaluation. A similar analysis was carried out by Das and Schwendimann, who had the same assumption but were able to find an analytical expression of general validity [47]. Josephson junctions have found applications in many areas of physics, including as a primary voltage standard (Figure 1.4)

Fulde et al. used an adaptation of Mori's method of continued fractions to derive mobilities for a silver iodide superconductor, which showed good agreement with experimental data but resulted in a rather unwieldy expression [69].

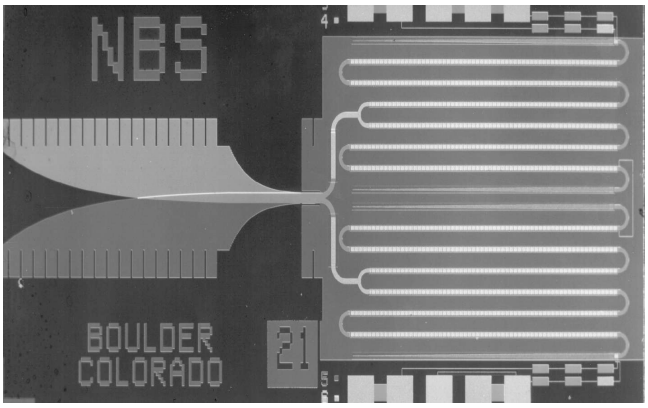

Figure 1.4: NIST primary voltage standard: microwave energy enters via the fin guides on the left, the Josephson junctions are biased with a current to generate a voltage; the junction produces alternating current at a frequency determined by this voltage. When the junctions are exposed to microwaves the oscillations lock to the microwave frequency, permitting only discrete voltages to be generated.

This method was followed by a collaborator of Fulde's, who uses it to find static and dynamic mobilities in both high and low noise regimes; again the author comments that the expansion is rather unwieldy, and it has problems with actual convergence due to the assumptions Mori made [49].

Foreshadowing the widespread adoption of homogenization theory that was to come, Fest and d'Adliano derived an expression for the diffusion coefficient in periodic potentials as a functional of the landscape which gave a generally intractable expression, but permitted the determination in one dimension [67]. Using a much simpler argument this result is reproduced by Weaver, who observes that the result is exactly that of Kramers' escape over a barrier solution [177].

Progress in the two-dimensional case was also made around this time by Zwanzig, who used a conformal mapping approach to study the eigenfunctions of the diffusion equation in channels, concluding that the effective diffusion is always reduced by the presence of periodic structures [190]. Weaver uses the same scenario of periodic channel flow and computes first passage times using a Green's function method; he then computes diffusion coefficients and compares to Zwanzig finding agreement after truncating to only one series term [178].

Recent Developments–Homogenization

The machinery of Homogenization had been around for years, but it was the introduction of two-scale convergence by Allaire in 1992 [3], who extended an idea of Nguetseng from earlier [137], that really allowed the method to become commonplace. Nguetseng proved a result for a class of integral functionals and

outlined his idea for the method, but Allaire's paper gives a better introduction to the process.

Additional motivation for the study of these periodic systems came from the study of so called 'Brownian Motors'. See Hänggi and Marchensoni's excellent review article for an introduction and progress on artificial devices demonstrating this phenomenon [88]. Related to our work, this has been analysed in a multi-scale fashion by Pavliotis, who also compared analytical results to numerical simulations in [148].

One of the easiest ways to model these systems is by assuming a periodic potential with a force applied externally. This can also be interpreted as a tilted periodic potential, and it seems clear that this should induce a current. Lindner showed in 2001 that the rate of transport (dimensionless Péclet number) was connected to both the forcing and the diffusion coefficient; he found exact and approximate relations for the Péclet number and compared to numerics [127]. He found that the Péclet number attains a maximum for moderate diffusion at strong tilts.

These results have recently been extended into two dimensions by a few authors. Generally the expressions are not analytically soluble - Kostur used a Finite-Element approach and compared to Monte Carlo simulations [115]. Approximations are also available, with Challis and Jack using machinery from quantum mechanics to treat the overdamped case. They use the tight-binding limit in their treatment and derive a condition for the validity of their expression [36]. In a different approach, Latorre et al. find a series expansion for the diffusion coefficient and use this to derive corrections for Einstein's relation which is perhaps a more straightforward representation [123].

González-Candela and Romero-Rochín applied a similar model to protein folding. They comment that their results are promising, but they need the actual numerical potential landscape to have any predictive power [79].

Random potentials have also garnered interest, although the homogenization process is substantially different - Olla provides a well organized account of previous work from different sources [145], but has to resort to proving convergence separately. Papanicolaou frames the same work in a different way, more in the framework of Homogenization, deriving the effective cell equation and stating it explicitly [147].

Combining periodic and bistable dynamics gives the problem at hand. Pavliotis has studied this problem extensively, giving the effective diffusivity in the absence of perturbations [149] as well as considering the problem of parameter estimation when separated time scales are present. This problem is also studied by Azencott et al. in [11], albeit with more general applicability. Duncan et al. consider the same problem with non separable potentials, showing that stable states are created by interactions between noise and perturbations in potential [53].

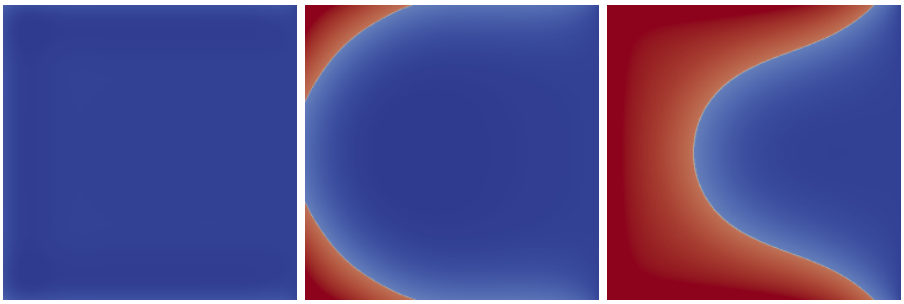

Figure 1.5: Single pore in a porous medium partially filled with condensate, pore is open on the right side. Simulation begins with a hydrophilic pore filled with vapour (left panel). Condensation begins in the corners of the pore (centre panel), droplets merge and spread along the hydrophilic walls (right panel). Red phase is condensate, blue is vapour, yellow region is the diffuse-interface. Image produced by the Author using FEniCS[5] to solve Cahn–Hilliard phase-field equations.

1.1.4 Phase-Field Modelling

The original motivation for so-called "Phase-Field" models was the study of phase separation in a process known as "Spinodal Decomposition". Cahn derived the evolution equation and the chemical potential from thermodynamic arguments, and initially applied the model to this phase separation process [29, 27, 30]. Subsequently this class of models have been applied to a wide range of systems; in Figure 1.5 they have been used to model condensation in a pore.

Technical Developments

A great deal of technical work followed, initially for Cahn–Hilliard with conventional boundary conditions. Amy Novick–Cohen made valuable contributions to the study of the mathematical properties of the equations, initially by finding equilibrium solutions and stability in [143], extended in [141] for concentration-dependent mobility. Zheng also made progress in this area, demonstrating that, in one dimension, a fixed number of solutions exist, and that each solution converges to an equilibrium solution as $t \to \infty$ [165].

Other convergence results, including compactness of solution orbits and some results on inertial manifolds, followed from Nicolaenko's work on pattern formation equations, for both Cahn–Hilliard and the related Kuramoto–Sivashinsky equations [138, 139]. Elliott and Zheng proved the existence of global attractors for some types of polynomial potential under certain constraints, as well as finding an example of a regime where negative leading order terms led to a constant steady state as opposed to finite-time blowup [63]. Together with French he also carried out initial work on Finite-Element formulations and splitting schemes

to treat the nonlinear potential term [59]

Further work in this direction has either relaxed the requirements on the potential, the function spaces or the boundary conditions. Stable solutions in potentials with walls were studied by Blowey and Elliott in [21] with numerical results in [20], motivated by taking a very low temperature, corresponding to a very deep potential, clamping the phase to $|\phi| \leq 1$. Elliott and Mikelić demonstrated existence for different forms of free-energy modifications in [62], and Kenmochi used a novel subdifferential approach to relax limitations in previous proofs [107].

Physical arguments suggest that the Mobility (M) ought to depend on the phase; this is because the phase ought not to vary substantially in the bulk. Initial existence results for this type of mobility were found by Elliott and Garcke [60], with the same authors later investigating phase transitions with the same mobility [61].

Equilibrium solutions were studied by Witelski in the context of polymer layer interactions [184], using phase-plane analysis. Subsequent work has shown that the equations reduce to simple interface evolution by the mean curvature [28], and has looked at this problem with multiple phases [112], as well as finite element formulations and weak solutions [13, 12, 180, 110, 153, 46]

More Complex Systems

Extensions into multicomponent solutions have also yielded valuable insights; Elliott and Luckhaus proved global existence and demonstrated that in the deep quench limit, Cahn–Hilliard reduces to an obstacle problem [58]. Cholewa and Dlotko found a global attractor for certain subspaces of solution in one-dimensional Hilbert Spaces $\mathcal{H}$ [38], which was subsequently extended to the two and three-dimensional spaces $\mathcal{H}^2$ and $\mathcal{H}^3$ by Dlotko in [51].

Regarding Boundary Conditions, beyond the classical Dirichlet and Neumann, recent interest has been in dynamic boundary conditions, beginning with Racke [152] and later elaborated on by Wu [185], Pruss [151] and Miranville [133] with their collaborators. More recently, progress has been made with permeable boundaries, with a view to applications in membrane science [71] and Wentzell boundary conditions, by Gal and Wu [70].

Recent progress has been made in improving the understanding of long-time behaviour, including new approaches for treating singularities with logarithmic potentials [132] leading to an exponential attractor. More recently still, Kostianko and Zelik obtained Inertial Manifolds for the 3D case with periodic boundary conditions [114].

Amongst the applications, an interesting example was put forward by Tremaine; he modelled the formation of Saturn's rings, and found that their structure could be produced using the Cahn–Hilliard equations with appropriate boundary conditions [171]

Concerning Flow–Linking to Kinematic Models

Modelling fluids using these equations is useful, but in many physically driven cases we are interested in the evolution of fluids in flow. Were the fluid one single phase it could be coupled to any of the well-studied equations of motion for a fluid via the chemical potential; making the assumption that this is also valid for multiple phases (which may have different viscosities and densities) allows these physical models to be studied with the benefits of the Cahn–Hilliard equations. The trade-off here is that the numerical solution of the equations becomes more difficult and the stability is negatively impacted.

Two related models that have bearing on this work are the connections to Navier–Stokes and, in the creeping flow limit, to Stokes' Equation. Early work on the coupled system followed from physical arguments; Joseph derived the system using Korteweg's idea that interfacial stress was proportional to the curvature in order to study bubble motion [103]. A different approach, motivated by the idea of separating balance laws by Gurtin, Polignone and Viñals, also derived the equations and carried out some numerical experiments [84].

Lowengrub and Truskinovsky investigated the sharp-interface limit of the Cahn–Hilliard–Navier–Stokes (CHNS) equations numerically, and used matched asymptotics to show that they reduce to the conventional two-phase Navier–Stokes equations [129]. Subsequently, Jacqmin [101] investigated this convergence to the sharp interface limit in more detail, providing reasonable ranges of values for the parameters.

Zhao, Wu and Huang offered strong solutions to the CHNS equations in some specific cases, together with proof of convergence from their strong solution to steady state in long time, with an estimate of convergence rate [188]. Abels showed that some strong solutions exist globally in two dimensions, and locally in time in three dimensions, for some singular free energies and unequal viscosities. He also showed regularity in long times for any weak solution [1].

Gal and Grasselli proved the existence of exponential attractors and demonstrated convergence of solutions to an equilibrium, together with convergence rate estimates in [72], and later work has relaxed restrictions and extended to three dimensions, for example [68].

Complications–Rheology and Multiple Phases

Extending the model to three phases has proven technically challenging. Boyer and Lapuerta showed that there are limitations on the choice of free-energy terms in the three-phase case that are necessary to obtain physically relevant results [24].

Boyer et al. subsequently observed that the standard formulation led to blowup in the fluid kinetic energy in certain cases; they proposed an alternative formulation to remove this issue and validated with some standard benchmark computation, including the liquid lens and heavy-liquid entrainment benchmarks [25].

There has also been progress in the modelling of flows with complex rheologies. Yue et al. replaced the conventional constitutive relationships for stress and performed some computational benchmarking [187], and Chupin presented existence and uniqueness for CHNS equations for Jeffry viscoelastic flows [41].

Other benchmarking work has been performed by Kim and Lowengrub; they studied the three-phase system using a multigrid method, and presented benchmark comparisons including liquid-lens and liquid-liquid extraction applications [109]. Kim has also applied different numerical schemes in [110, 111].

Recently Gal, Grasselli and Miranville applied Generalised Navier Boundary Conditions to the CHNS model to account for slip velocity, and derived the existence of a global energy solution and convergence to equilibrium in time [73].

Creeping Flow–Convective Cahn–Hilliard Equations

For the creeping flow regime, the problem reduces to Cahn–Hilliard coupled by a convection term to Stokes' equations. Motivated by interest from the study of crystal growth, amongst other applications (see [176] for example), Golovin et al. investigated the transition from coarsening to chaos by varying the driving force, resulting in behaviour reminiscent of the related Kuramoto–Sivashinsky Equations [78].

Eden and Kalantarov studied this model with periodic boundaries and showed the existence of a compact attractor and finite dimensional manifold; they also established regularity of solutions on the attractor [57], and subsequently achieved similar results for the global attractor and estimated its dimension in [56]. Liu established the existence of weak solutions for this problem with degenerate mobility [128].

Zhao formulated a Galerkin-Spectral approximation in two dimensions and showed the existence of global attractors to this discrete system [189], and recently, Gidey and Reddy presented an unconditionally stable operator-splitting approach using front tracking, which they claim is more efficient in some physically relevant cases than existing monolithic methods [76].

Colli et al. study models for tumor growth and the related optimal control and optimal distributed control problems; they show existence and uniqueness for solutions to the model, as well as existence of an optimal control strategy and the first-order optimality conditions thereof [43, 42, 44, 45]. Garke and Lam looked at the same application and compared the effects of different boundary conditions on the solutions [74].

Thiele and Knobloch presented a model for thin-film flow down a heated inclined plane, showing that in some regimes it reduced to either the conventional Cahn–Hilliard or Convective Cahn–Hilliard equations [169]. This is a classical benchmarking problem for fluid solvers coupled to heat transfer, so offers good comparisons for Cahn–Hilliard solvers to readily available experimental data.

1.2 Thesis Aims and Structure

The present work seeks to employ tools and techniques from the study of complex multiscale systems to three different problems. At first sight the models do not appear to share much in common, but they all have behaviour that relies on a separation of scales. In the case of Chapter 2, where the interaction between noise and a microscale causes macroscopic behaviour, this is explicit, whilst the Cahn–Hilliard and related equations make use of the scale separation between the interface width and the fluid macroscale (described by the dimensionless Cahn number Cn) to justify physical assumptions.

In Chapter 2 we investigate the motion of particles in a multiscale potential, we introduce an asymmetry into the macroscale potential and investigate the effect on the homogenised equation. We then quantify the phase transition observed and compare this with literature on the symmetric problem.

In Chapters 3 and 4 we study two variants to the classical Cahn–Hilliard equations describing a Diffuse-Interface model for fluid flow. Our goal is to understand how the interaction between the interface and the confinement affects the macroscopic flow.

In Chapter 3 we study nucleation, coarsening and flow in a corrugated channel and perform numerical simulations using a coupled Cahn–Hilliard–Navier–Stokes model. We observe different flow morphologies for long times and rationalise these with an energy-based phase-plane approach.

In Chapter 4 we use a convective Cahn–Hilliard–Stokes model to study interfacial flow in porous media. We use the machinery of Homogenisation to produce a macroscopic description of the flow and perform numerical simulations in channels.

We conclude the present work with general comments on the application of Multiscale Analysis to these areas of study, as well as recommendations for future work. In particular Chapter 2 and Chapter 3 offer many opportunities for extension and validation which we discuss.

2

Diffusion in a Tilted Multiscale Potential

Brownian motion is a very valuable tool to simulate many physical phenomena where noise of some sort is important. This setup has been used to model superconduction [69], neuronal firing [181] and surface diffusion [119], amongst others. Amongst the quantities that can be measured from these models we are normally interested in either the rate of transition from one state to another, which gives a measure of the reaction rate [89], or the static probability distribution, which gives a measure of the equilibrium between one product and reactant (see Figure 2.1).

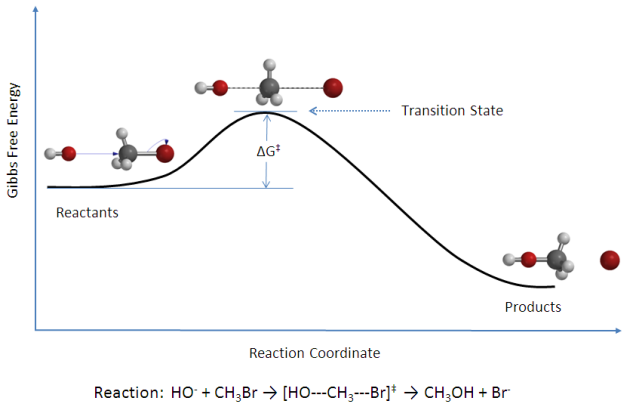

Figure 2.1: A typical reaction potential diagram, here for the hydrolysis of bromomethane. CC-by-SA license from Wikipedia

2.1 Introduction and Motivation

Motion of this sort is usually represented in one of two ways, either describing the instantaneous motion of a particle under the influence of a force and a noise term, or by the likelihood of observing a particle at a given point.

$$dX_t = -\nabla V(X_t)dt + \sqrt{2\sigma}dB_t \tag{2.1}$$

Equation 2.1 describes this motion instantaneously, where X_t is the particle's position vector, $V(x)$ is a spatially varying potential, σ is the noise intensity, and dB_t is a Brownian noise term with mean zero and variance of one. It is known as the Langevin description of particle motion and is a Stochastic Differential Equation (SDE).

$$P_t(x,t) = -\nabla_x\left(-\nabla_x V(x)P(x,t)\right) + \Delta_x\left(\sigma P(x,t)\right) \tag{2.2}$$

Equation 2.2 describes the evolution of the probability density over time, where $P_t\left(x,t\right)$ is the time-dependent probablity distribution of the process, $V(x) and \sigma$ are as above, and ∇ is the spatial derivative.

This equation is known variously as the Fokker-Planck Equation (FPE), the Forward Kolmogorov Equation, or in the context of Brownian motion usually the Smoluchowski Equation.

We define the multiscale potential in the problem to be of the following form (Equation 2.3)

$$V(x) = \frac{1}{4}x^4 - \frac{\alpha}{2}x^2 - \frac{1}{2}\sin(2\pi x/\varepsilon)x^2 + \eta x \quad \epsilon \ll 1 \tag{2.3}$$

Where α is a term that controls the height of the central energy barrier, ε is the scale separation parameter, and η is a small asymmetry that we introduce into the system.

Our model considers a simple bistable potential that is familiar from reaction rate theory and superimposes fast periodic fluctuations of some sort (2.3). We then intend to homogenize the FPE to derive an effective Langevin SDE for the particle motion. We then intend to study several parameters with physical interpretation and of physical interest and compare the homogenised and unhomogenised behaviour.

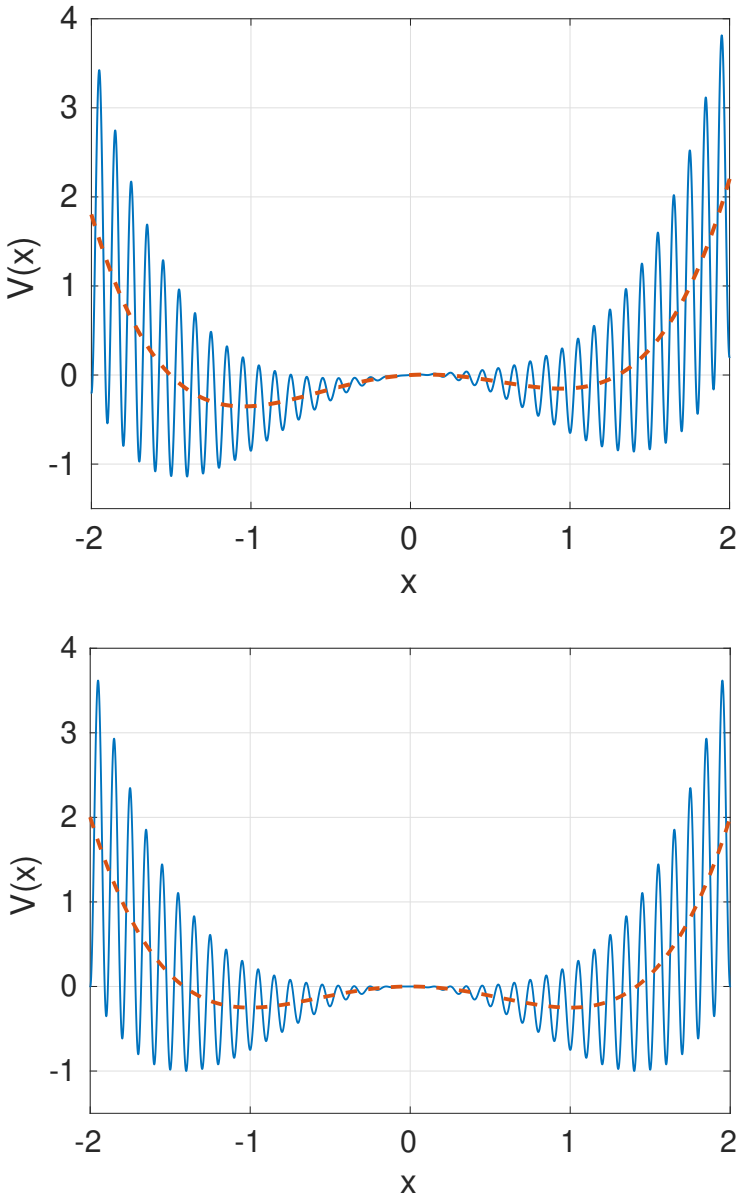

Figure 2.2: Bistable potentials (dashed) with periodic micro-scales (solid) [Equation 2.3], $\lambda = 1$, $\varepsilon = 0.1$, with $\eta = 0$ (top) and $\eta = 0.1$ (bottom)

2.2 Homogenisation

The homogenisation of systems with multi-scale potentials under the influence of noise is an area of ongoing study, a majority of models with physical applications are not known to be amenable. Recently work has been carried out on a symmetric version of the system in Equations 2.1 and 2.3 [53]. Beginning from Equation 2.1 and a generalised version of Equation 2.3, they expand in orders of ε, the scale separation parameter.

The derivation begins by writing the Backward Kolmogorov Equation (BKE) corresponding to the SDE Equation (2.1), this is another equivalent way of expressing the equation to the FPE mentioned in Equation (2.2):

$$\partial_t F^\varepsilon(x,t) = \mathcal{L}^\varepsilon F(x,t) \tag{2.4}$$

where we have defined the infinitesimal generator

$$\mathcal{L}^\varepsilon f(x) = -\nabla V^\varepsilon(x)\cdot\nabla f(x) + \sigma\Delta f(x)\ . \tag{2.5}$$

The process is to "freeze" the scales x, $\frac{x}{\varepsilon}$, $\frac{x}{\varepsilon^2}\cdots$ and to quantify the macroscopic effects of the $\mathcal{O}\left(\varepsilon^{-N}\right)$ term. We formally assume that the variable $\frac{x}{\varepsilon^N}$ is independent of the lower order terms and write $V^\varepsilon(x) = V_N^\varepsilon\left(x,\,\frac{x}{\epsilon^N}\right)$ we then have that:

$$\nabla_x V^\varepsilon(x) = \left(\nabla_x + \frac{1}{\varepsilon^N}\nabla_z\right) V_N^\varepsilon(x,\,z)\Big|_{z=\frac{x}{\varepsilon^N}}\ . \tag{2.6}$$

We look for solutions of $F^\varepsilon(x,\,t)$ of the form $F^\varepsilon(x,\,z,\,t)$ where

$$F(x,\,z,\,t) = F_0(x,\,z,\,t) + \varepsilon F_1(x,\,z,\,t) + \varepsilon^2 F_2(x,\,z,\,t) + \cdots\ . \tag{2.7}$$

The Backward Kolmogorov equation can then be rewritten as

$$\partial_t F(x,\,z,\,t) = -D_N V^\varepsilon(x,\,t)\,D_N F(x,\,z,\,t) + \sigma D_N\cdot D_N F(x,\,z,\,t)\ , \tag{2.8}$$

where $D_N = \left(\nabla_x + \varepsilon^{-N}\nabla_z\right)$. Performing a standard homogenization procedure of the above equation we can obtain the effective dynamics in the limit that $\varepsilon\to 0$. Substituting the expansion Equation (2.7) into the BKE we consider the leading order terms of the expansion in powers of $\frac{1}{\varepsilon}$. The $\mathcal{O}\varepsilon^{-2N}$ term can be written as

$$\nabla_z\cdot\left(e^{-V_N^\varepsilon(x,\,z)/\sigma}\nabla_z F_0(x,\,z,\,t)\right) = 0\,. \tag{2.9}$$

We observe that for fixed x the exponential quantity is strictly positive, this implies that F_0 is independent of the fast variable, i.e. $F_0(x,\,z,\,t) = F_0(x,\,t)$. The $\mathcal{O}\epsilon^{-N}$ equation is given by

$$\nabla_z \cdot \left(e^{-V_N^\varepsilon(x,\,z)/\sigma} \nabla_z F_1\left(x,\,z,\,t\right) \right) = \nabla_z \cdot \left(e^{-V_N^\varepsilon(x,\,z)/\sigma} \right) \partial_x F_0\left(x,\,t\right) . \quad (2.10)$$

Solutions to this equation can be constructed as follows: take $\theta_N\left(x,\,z\right)$ to be the vector-values solutions to the following Poisson equation:

$$\nabla_z \cdot \left(e^{-V_N^\varepsilon(x,\,z)/\sigma} \left(\nabla_z \theta_N\left(x,\,z\right) + I \right) \right) = 0\,, \quad (2.11)$$

where $\left(\nabla_z \theta_N\right)_{ij} = \partial_{z_i} \theta_{N,j}$ for $i,\,j = 1,\,\cdots,\,d$. We have created the solution $F_1\left(x,\,z,\,t\right) = \theta_N\left(x,\,z\right) \nabla_x F_0\left(x,\,t\right)$ which satisfies our $\mathcal{O}\epsilon^{-N}$ equation above. Finally we consider the $\mathcal{O}1$ equation which is given by

$$\begin{aligned} \nabla_z \cdot \left(e^{-V_N^\varepsilon(x,\,z)/\sigma} \nabla_z F_2\left(x,\,z,\,t\right) \right) = &- \nabla_z \cdot \left(e^{-V_N^\varepsilon(x,\,z)/\sigma} \nabla_x F_1\left(x,\,z,\,t\right) \right) \\ &- \nabla_z \cdot \left(e^{-V_N^\varepsilon(x,\,z)/\sigma} \nabla_z F_1\left(x,\,z,\,t\right) \right) \\ &- \nabla_z \cdot \left(e^{-V_N^\varepsilon(x,\,z)/\sigma} \nabla_x F_0\left(x,\,t\right) \right) \\ &- \frac{e^{-V^{\varepsilon_N}(x,\,z)/\sigma}}{\sigma} \partial_t F_0\left(x,\,t\right) \end{aligned} \quad (2.12)$$

A necessary and sufficient condition for the existence of F_2 is that the RHS have zero integral with respect to $e^{-V_N^\varepsilon(x,\,z)}\,\mathrm{d}z$:

$$\begin{aligned} Z_{N-1}\left(x\right) \partial_t F\left(x,\,t\right) &= \sigma \nabla_x \cdot \left(\int e^{-V^{\varepsilon_N}(x,\,z)/\sigma} \nabla_z F_1\left(x,\,z,\,t\right)\,\mathrm{d}z \right) \\ &\quad + \sigma \nabla_x \left(\int e^{-V^{\varepsilon_N}(x,\,z)/\sigma}\,\mathrm{d}z \nabla_x F_0\left(x,\,t\right) \right) , \quad (2.13) \\ &= \sigma \nabla_x \left(\int e^{-V^{\varepsilon_N}(x,\,z)/\sigma} \left(\nabla_z \theta_N + I \right)\,\mathrm{d}z \nabla_x F_0\left(x,\,t\right) \right) , \quad (2.14) \\ &= \nabla_x \left(K_{N-1}\left(x\right) \nabla_x F_0\left(x,\,t\right) \right) , \quad (2.15) \end{aligned}$$

where

$$Z_{N-1}\left(x\right) = \int e^{-V^{\varepsilon_N}(x,\,z)/\sigma}\,\mathrm{d}z\,,$$

and

$$K_{N-1}\left(x\right) = \sigma \int e^{-V^{\varepsilon_N}(x,\,z)/\sigma} \left(\nabla_z \theta_N\left(x,\,z\right) + I \right)\,\mathrm{d}z\,.$$

Repeating this process inductively for all intermediate scales, introducing each microscale in turn, we obtain the final coarse-grained BKE that is independent of ε:

$$\partial_t F_0\left(x,\,t\right) = \frac{1}{Z\left(x\right)} \nabla_x \cdot \left(K\left(x\right) \nabla_x\left(x,\,t\right) \right) , \quad (2.16)$$

where

$$Z(x) = \int \cdots \int e^{-V^{(x,\, x_1,\, \cdots,\, x_N)/\sigma}} \, \mathrm{d}x_1 \cdots \mathrm{d}x_N \,,$$

and

$$K(x) = \sigma \int \cdots \int \prod_{i=N}^{1} \left(1 + \nabla_{x_i} \theta_i \left(x,\, x_1,\, \cdots,\, x_i\right)\right) e^{-V^{(x,\, x_1,\, \cdots,\, x_N)/\sigma}} \, \mathrm{d}x_1 \cdots \mathrm{d}x_N \,,$$

where the correctors $\theta_1, \cdots, \theta_N$ are the solutions of the cell equations (Equation (2.11)) at each scale, known up to an additive constant. This corresponds to a new diffusion process, which we call the homogenised process, described by the new SDE:

$$dx_t^0 = \left[-\mathcal{M}\left(x_t^0\right) \nabla_x \Psi\left(x_t^0\right) + \nabla_x \cdot \mathcal{M}\left(x_t^0\right)\right] dt + \sqrt{2\mathcal{M}\left(x_t^0\right)} dW_t \,, \tag{2.17}$$

where we use the definitions:

$$\mathcal{M}(x) = \frac{K(x)}{Z(x)}$$

and

$$\Psi(x) = -\log Z(x) \,.$$

In the tilted bistable case (Equation 2.3) we admit only one micro-scale, in this case we use the fact that the homogenised dynamics are exponentially ergodic with respect to the invariant distribution. This allows us to find the steady-state distribution function ρ directly:

$$\begin{aligned} \rho(x) &= \frac{Z(x)}{\bar{Z}} \\ &= \frac{1}{\bar{Z}} e^{-V_0/\sigma} I_0\left(\frac{x^2}{2\sigma}\right) , \qquad (2.18) \\ \bar{Z} &= \int_{\mathbb{R}^1} e^{-V_0/\sigma} I_0\left(\frac{x^2}{2\sigma}\right) \mathrm{d}x \qquad (2.19) \end{aligned}$$

where I_0 is the modified Bessel function of the first kind.

This approach allows us to find the long-term behaviour of the system in the limit that $\varepsilon \to 0$, a regime where numerical simulation becomes prohibitive.

2.3 Numerical Method

In order to investigate the effect of the tilt on the stability of bifurcations we need to study Equation 2.18. Its stationary points will give us the locations of maxima and minima in the probability density function.

The principal tool to study the behaviour and bifurcation of stationary solutions to equations that do not permit analytical study is numerical continuation. A naive approach would be to solve the equation in question numerically throughout the parameter space and generate the bifurcation diagram that way. This will produce a sketch of the diagram, but it is difficult to approach limit points like this, doing so requires increasingly small steps in the principle bifurcation parameter to resolve the area around the limit point. Standard non-linear equation solvers also become less able to distinguish between the branches as they close, leading to errors in the branch locations.
These problems can partially be ameliorated by resolving the areas around limit points by solving in a transverse direction, i.e. by fixing the spatial position (x) and solving for the bifurcation parameters α, this can also be accelerated by using neighbouring fixed point locations as starting points for the non-linear solver, but in general this is an unsatisfactory solution.
The approach adopted in this work, and across literature is numerical continuation. Instead of restarting the solution process at each new value of the bifurcation parameter we use our knowledge of an existing point to predict the next location using a linear solver, we then correct this location using Newton's method (Figure 2.3).

The specific numerical continuation method we employ is called "Pseudo-arclength Continuation". We assume that we already have a solution to the equation at some point, for example we might use Newton's method at the end of the area of interest to find an initial solution. We call this point $\mathbf{u}$ and it solves the equation $F(\mathbf{u}) = 0$. We then parametrise both the principal continuation parameter α and the solution location $u(\alpha)$ in terms of the distance along the solution curve s from some point:

$$F(\mathbf{u}(s), \alpha(s)) = 0 \tag{2.20}$$

Taking the definition of arc length and the step size Δs, which we can allow to vary in order maximise accuracy or speed as necessary we close the problem. Taking $(\dot{\mathbf{u_0}}, \dot{\alpha})$ to be the tangent at the point $(\mathbf{u_0}, \alpha_0)$:

$$\dot{\mathbf{u}}(\mathbf{u} - \mathbf{u_0}) + \dot{\alpha}(\alpha - \alpha_0) = \Delta s \tag{2.21}$$

Once the branch of the solution has been identified and continued we can identify limit points. These correspond to turning points in the function being continued, and physically represent the extrema of the probability distribution of the system (regions where the probability of observing a particle once the system has reached steady state is greatest or least). These can be found by locating points where the x derivative of F is zero:

$$F(\mathbf{u}^*, \alpha^*) = 0\,, \quad \left(\frac{\partial F}{\partial x}\right)_{x^*,\alpha^*} = 0\,, \quad \left(\frac{\partial F}{\partial \alpha}\right)_{x^*,\alpha^*} \neq 0 \tag{2.22}$$

, The main avenue of study in this system is to investigate how the existence of limit points is affected by the noise intensity, this is essentially another parameter in the system, so we re-parametrise the system to include the noise intensity

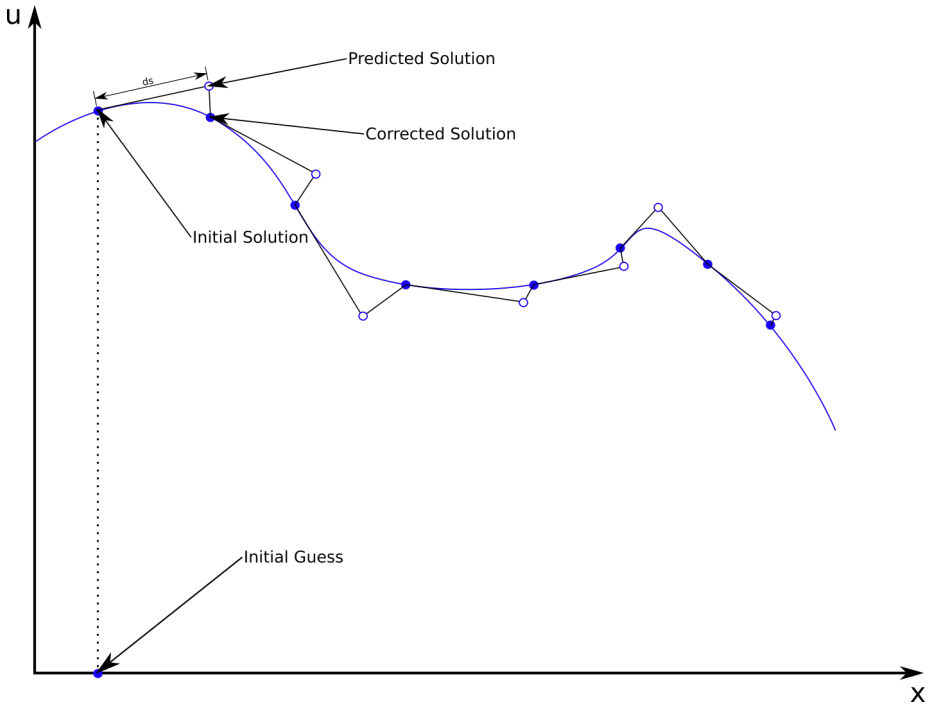

Figure 2.3: Schematic diagram of the process of Pseudo-Arclength continuation. From an initial solution a predictor step is taken along the tangent for a given step size ds to give a predicted solution (empty blue circle). Newton's method is then used to correct this to an actual solution (filled blue circle). We note that the step size can be adapted when the function's second derivative is large.

σ.

$$F\left(\mathbf{u}\left(s,\sigma\right),\alpha\left(s,\sigma\right)\right)=0 \tag{2.23}$$

The continuation approach is the same as before, we identify an initial point where we expect to see a limit point and solve the full system with a Newton solver. This is continued as before at a fixed value of σ to identify the location of the limit point. If no limit point is observed then we choose a new value of σ and try again. If we identify a limit point then we allow σ to vary, our

continuation equations now read:

$$\begin{aligned} F\left(\mathbf{u}^*, \alpha^*, \sigma^*\right) &= 0\,, \\ \left(\frac{\partial F}{\partial x}\right)_{x^*,\alpha^*,\sigma^*} &= 0\,, \\ \left(\frac{\partial F}{\partial \alpha}\right)_{x^*,\alpha^*,\sigma^*} &\neq 0\,, \\ \left(\frac{\partial F}{\partial \sigma}\right)_{x^*,\alpha^*,\sigma^*} &\neq 0\,. \end{aligned} \tag{2.24}$$

2.4 Results

Locating extrema to the homogenised probability density function (Equation 2.18) corresponds to finding the zeroes of its spatial derivative. Computing the derivative we obtain, using standard results for the derivative of the modified Bessel function of the first-kind,

$$\begin{aligned} \frac{\partial \rho\left(x\right)}{\partial x} =& \frac{\partial}{\partial x}\left(e^{-V_0/\sigma} I_0\left(\frac{x^2}{2\sigma}\right)\right) \\ =& \frac{1}{\sigma} e^{-V_0/\sigma}\left(\left(x^3 - \alpha x + \eta\right) I_0\left(\frac{x^2}{2\sigma}\right) - x I_1\left(\frac{x^2}{2\sigma}\right)\right)\,. \end{aligned} \tag{2.25}$$

Setting this to zero and rearranging we obtain:

$$x^3 - \left(\alpha + \frac{I_1\left(\frac{x^2}{2\sigma}\right)}{I_0\left(\frac{x^2}{2\sigma}\right)}\right) x + \eta = 0\,. \tag{2.26}$$

In order to carry out the continuation procedure we observe that for small values of σ the quotient I_1/I_0 approaches unity. This can be shown by taking the large z limit of the modified Bessel function [146]:

$$\lim_{z\to\infty} I_\nu\left(z\right) = \frac{e^z}{\sqrt{2\pi z}}\,, \tag{2.27}$$

this is independent of the value of the argument ν, and therefore for sufficiently small σ we can write that:

$$x^3 - \alpha x + \eta = 0 \tag{2.28}$$

We can therefore solve the approximate equation directly in order to obtain an initial solution. Given the form of the Equation 2.26 we find that there are multiple branches, and therefore we follow the stable branch first and then restart continuation on the unstable branch.

Continuation was carried out using the open-source software package AUTO-07p [52] together with interface software written by the author in MATLAB.

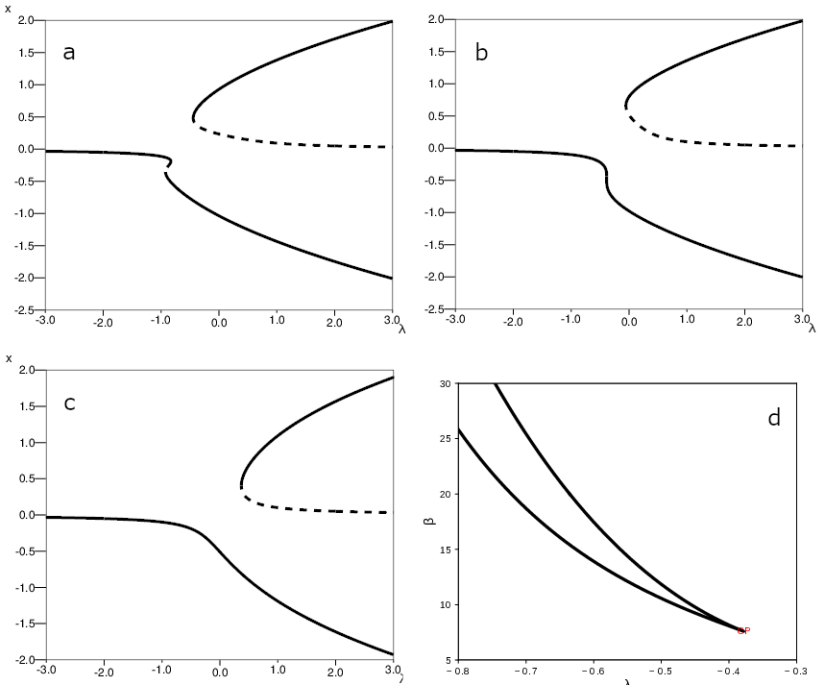

Figure 2.4: Bifurcation diagrams for $\eta = 0.1$ for different noise intensities: (a) $\sigma = 0.025$; (b) $\sigma = 7.8 \approx \sigma_c$; (c) $\sigma = 1$; (d) Cusp in $\lambda - \sigma$ space at $\sigma \cong 0.128$

In Figure 2.4 we observe three distinct regimes which are characteristic of a pitchfork bifurcation, the same transition observed for the symmetric case in [53]: as the noise is reduced the interaction between the periodic micro-scale and the noise causes a stabilised region to form on the stable branch.

When the noise intensity is very high the stable branch has no hysteresis behaviour and only one inflection point (panel c). As the noise reduces the system passes a critical point (panel b), beyond which the system exhibits hysteresis behaviour, and we observe a stable region forming on the stable branch (panel a).

Following the limit points from panel a, the noise is increased until the limit points merge, as in panel b. The cusp bifurcation observed can then be represented in $\sigma - \lambda - x$ space; the three projections into two dimensions are shown below (Figure 2.5), for different values of η. The behaviour is complex, but the general trend is for smaller critical σ with increased tilt, a narrower region of metastability in the x direction, and the limit points moving more negative in λ.

Plotting the critical noise intensity as a function of the tilt (Figure 2.6) shows this first trend; increasing the tilt serves to destabilise the metastable region, limiting the noise intensity at which it is observed.

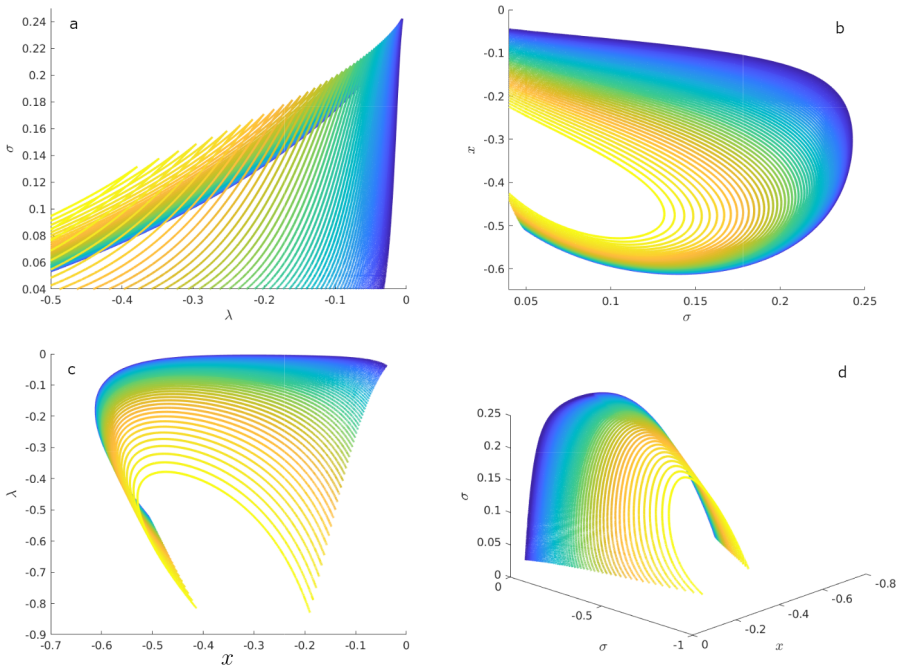

Figure 2.5: Limit point location approaching cusp for different strengths of tilt *eta*. First three panels show projections onto the coordinate axes: (a) $\lambda - \sigma$; (b) $\sigma - x$; (c) $x - \lambda$. (d) shows a portion of parameter space in 3 dimensions. In all cases η varies from 10^{-3} in blue to 10^{-1} in yellow.

The tilt also serves to narrow this metastable region as observed in panels b and c of Figure 2.5. Referring to the potential (Equation 2.3), the trend reducing the critical value of λ can be understood as the tilt reducing the depth of the local potential well, so a deeper well is needed to maintain the metastable area.

One quantifier for a change of this kind comes from the theory of phase transitions. Identifying the noise intensity as a temperature, we define a reduced temperature T_c as the controlling quantity, and we look at the response in the principal bifurcation parameter $|\lambda|$. Thermodynamically, this corresponds to the density difference between two phases as the temperature approaches criticality.

$$X \equiv \frac{\sigma_c - \sigma}{\sigma_c}, \quad Y \equiv \frac{|\alpha_c|}{N} \tag{2.29}$$

$$Y \propto |X|^{\gamma}, \tag{2.30}$$

In the rescaled space Figure 2.7 we observe straight line fit, confirming that a critical exponent of this form does describe the bifurcation process. Performing

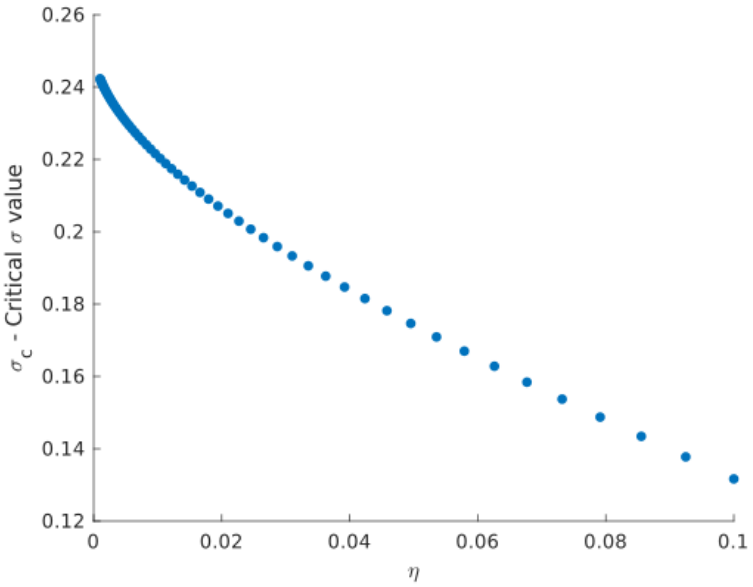

Figure 2.6: Effect of tilt (η) on critical noise intensity (σ_c)

a linear fit of these curves recovers an exponent of $\gamma \approxeq 0.66$. This exponent seems to be insensitive to the size of the tilt (Figure 2.8), suggesting that the mechanism by which the limit points are destabilised is not related to the critical exponent.

We observe that the critical exponent computed in this study is not the same as that computed by Duncan et al. in their study [53] where they recover $\gamma = 1.6$ independent of the number of scales.

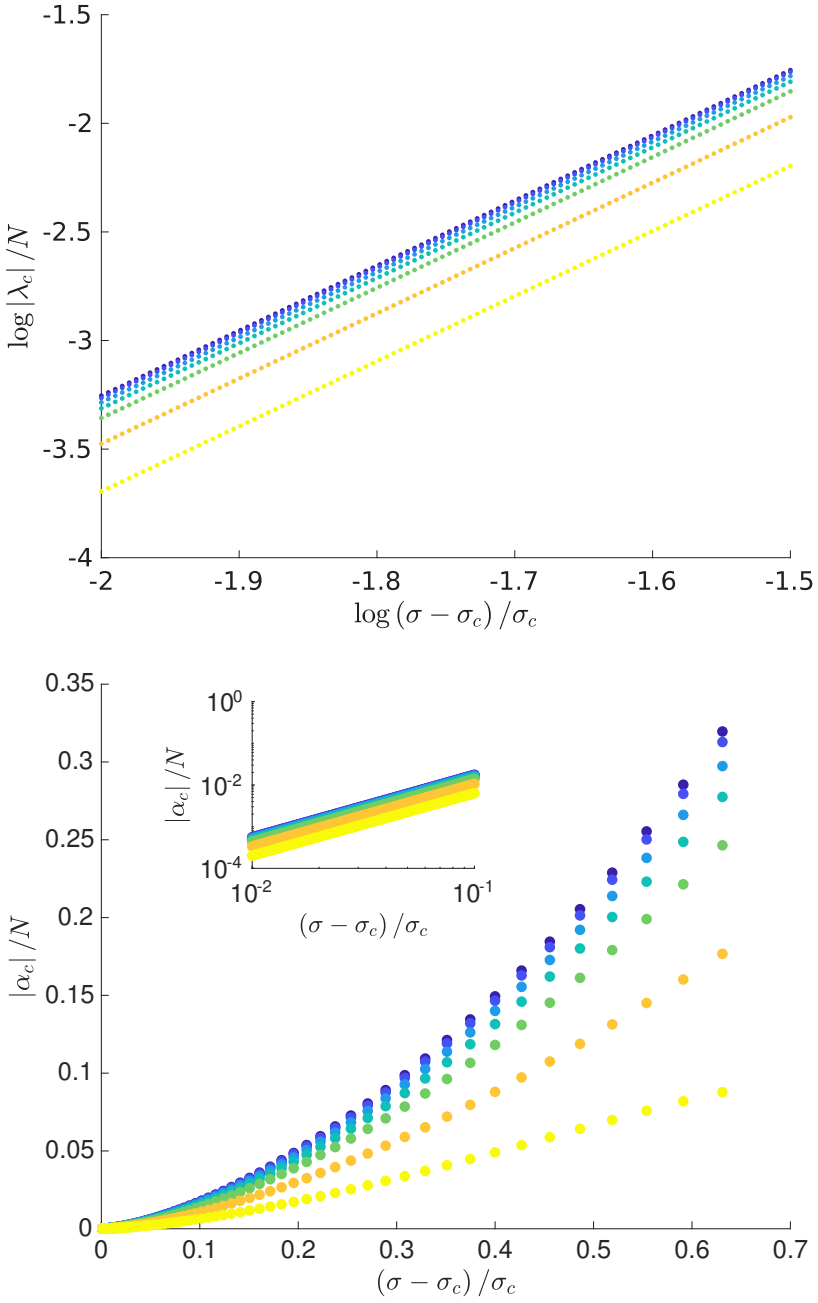

Figure 2.7: Transition from subcritical to supercritical behaviour as the noise intensity is increased.

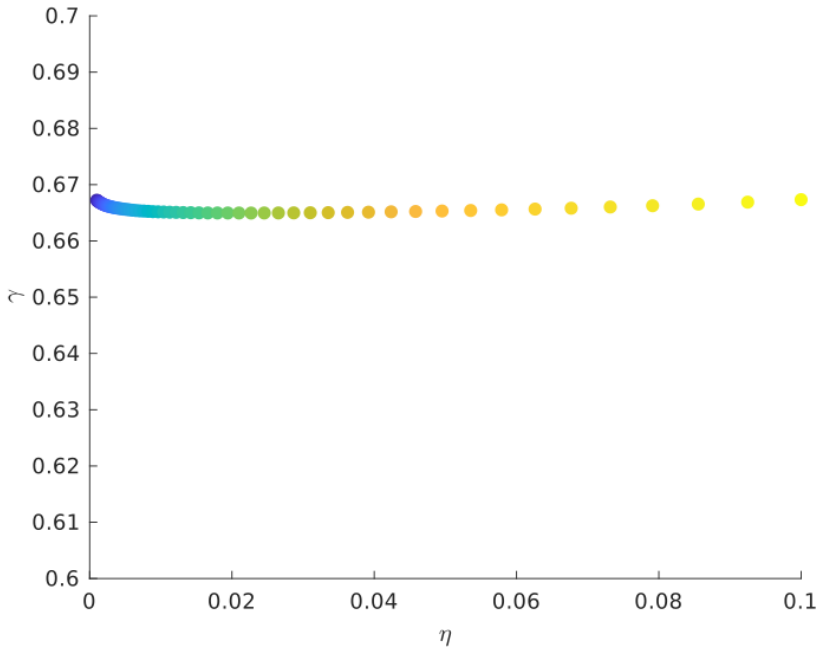

Figure 2.8: Effect of tilt (η) on critical exponent (γ)

2.5 Conclusions and Future Work

We studied the interaction between an asymmetric multiscale potential and noise. Homogenising the governing equations we found that since the macroscale potential does not enter into the microscopic governing equations it does not affect the homogenisation process, and so existing results for the macroscopic Distribution Function can be applied directly.

Study of the homogenised equations confirmed that for small tilts we can recover the symmetric result that $\sigma_c = 0.25$, whilst for increasing tilts the critical noise intensity decreases. This is explained by the tilt destabilising the induced local minima, and eventually destroying them altogether.

We quantified the bifurcation in terms of phase transitions, and confirmed that power law behaviour is observed in approach to criticality with a critical exponent of $\gamma \approxeq 0.66$. This contrasts with the result for the symmetrical case from Duncan et al. [53], suggesting that the asymmetry in the problem changes the critical behaviour of the system fundamentally.

There is ample opportunity for further work in this direction, results exist to extend this two scale result to any number of scales separated by increasing orders of the scale separation parameter. A direct extension of the current work would be to reproduce the results for multiple separated scales, the authors

expect to observe wider regions of metastability with increasing numbers of scales.

The present work only considers one kind of physically relevant macroscopic potential, the work can be extended to any confined potential within C^1, and to piecewise linear potentials, offering a wide scope for further study. An interesting problem would be to investigate the effects of periodic potentials, such as a tilted ratchet potential, this would require careful treatment of the microscale, but could yield promising results.

The authors also consider that extension of the present work into three or more dimensions could offer interesting applications, particularly in protein folding. Analytical results are no longer available, and the cell problem must be solved numerically, but the increase in applicability of the model is likely worth the computational effort involved.

3

Phase Separation in Confined Geometries

Nucleation in quenched fluids is a very classical problem for Cahn–Hilliard type models, indeed the original derivation by Cahn ([29], [30]) assumed that an alloy was quenched and crystals formed in the solid. This can be used to model engineering systems like phase separation in flash vessels, or for microfluidic separators ([158] for example). In this work we study the nucleation of a fluid in a channel which, after some time has passed, is influenced by an external force causing flow to occur along the channel, we are interested in how the transport properties are affected by the channel geometry, and to that end we corrugate the channel.

We begin by introducing the Cahn–Hilliard equations and their coupling to the Navier–Stokes equations for a description of multiphase flow with convection, we then perform a static energy analysis of different flow configurations in order to inform our numerical experiments.

We then derive a finite-element formulation including a splitting scheme for the nonlinear potential term which enables us to simulate the flow field. We draw some conclusions from the results and suggest directions for future work.

3.1 Introduction

In this section we introduce the theoretical background and justification for the coupled Cahn–Hilliard-Navier–Stokes equations as a model for multiphase flow in confined geometries.

3.1.1 The Cahn–Hilliard Equations

The Cahn–Hilliard equations were first posed as a phenomenological model for phase separation in a series of papers by Cahn and Hilliard ([29],[30] and [27]) as a model for phase separation by spinodal decomposition. In contrast to classical nucleation for phase separation, spinodal decomposition is usually encountered

when a mixture that is above its critical point is rapidly cooled to below the critical point whereupon small clusters of each constituent phase will form spontaneously throughout the fluid.
These clusters then enlarge by a process known as Ostwald Ripening, eventually forming droplets of one phase supported in the other. This process is of interest in areas such as Metallurgy[14, 154], Geology[166, 48] and Chemistry[174].
Since the original paper there have been many derivations for these equations, both physically based and phenomenological, a good review of derivations is given by Lee et al. [125].

3.1.2 The Cahn–Hilliard Navier–Stokes' Equations

The utility of the Cahn–Hilliard (C–H) equations in studies of diffusive-dominated flow is great, however only a small fraction of flow problems fall into this regime. Many more problems require the resolution of convective flow as well as diffusive, and for this the C–H equations must be coupled to some kind of momentum conservation model. Two models that have received much study are the Cahn–Hilliard Navier–Stokes (CHNS) model (Model H in the terminology of Hohenberg and Halperin [92]), and the reduced Cahn–Hilliard Stokes model (CHS), for creeping flow (Re $<<$ 1).

These models are attractive for several reasons, the stress-singularity formed at the contact line of a sharp interface model is not present, neither slip-length nor special treatment of that region is required. The smoothness of the phase-field also allows a simple unstructured mesh to be used in computation, and this can be adapted as necessary without difficulty. Lastly the use of two well-studied models allows expertise from Computational Fluid Dynamics (CFD) in the solution of the Navier–Stokes equations and existing methods to solve the C-H equations to be applied.

The addition of a characteristic length scale for the interface does, however, introduce the same problems we see with other multi-scale methods. We are interested in the macroscopic flow field and morphology, but it becomes critical to correctly resolve the behaviour of the fluids across the interface. This requires us to carefully design numerical schemes that allow for mesh and time-step adaptation, as well as dealing with very stiff equations. The scale separation has its own dimensionless number in this field, the Cahn number Cn which is the ratio of the interface width to the characteristic length scale of the flow geometry.

Within the literature the CHNS equations are currently less well applied than other models for two-phase flow, largely being relegated to modelling test-cases and benchmarks, but they show promise in these. A major reason for the lack of application has been historical: the first method for simulating free surface flows to achieve widespread adoption was the Volume of Fluid method (VOF), which is used to this day in many commercial CFD codes including Fluent and STAR-CCM. Additionally the value for the interface thickness, or equivalently the Cahn Number (C_N), must be very small ($\mathcal{O}\left(10^{-9}m\right)$) to model meaning-

ful flows accurately. That said, relaxing this requirement to simply enforce a scale separation allows simulation of fluid flow in a qualitatively reasonable way. Direct benchmarking of CHNS solvers against the widely accepted VOF method gives reasonable agreement in the rising and falling droplet benchmarks ([2],[66]). This suggests that the CHNS model can be applied to physically relevant situations with relatively large interface widths, recovering comparable results to the classical VOF method.

3.2 Derivation of The Cahn–Hilliard Navier–Stokes Equations

In order to motivate the coupled CHNS equations we follow a derivation from microforce balances first presented by Gurtin [84]. This makes the balance laws that govern the fluid flow clear, and presents a more rigorous argument than the classical derivation, this has the benefit of justifying the connection to the Navier–Stokes equations.

The basic premise of the microforce balance approach is to assert that within some region R the power exerted on atomic configurations within R for some change in the order parameter ϕ can be written as one of the following:

$$\int_{\partial R} (\xi \cdot \mathbf{n})\, \rho' \,\mathrm{d}a\,, \quad \int_R \pi \rho' \,\mathrm{d}v\,, \quad \int_R \gamma \rho' \,\mathrm{d}v\,.$$

Here we have defined a vector stress ξ and two scalar forces π and γ which represent internal and external forces respectively, distributed over the body of the fluid. The integrals represent the power expended by neighbours of R across the boundary ∂R, the power expended on the atoms by the lattice, and the power expended on the atoms by external forces.

The microforce balance can then be written for each control volume as:

$$\int_{\partial R} \xi \cdot \mathbf{n} \,\mathrm{d}a + \int_R (\pi + \gamma)\ \mathrm{d}v = 0 \tag{3.1}$$

We also identify the external work done on some control volume as:

$$\mathcal{W}(r) = \int_{\partial R} (\xi \cdot \mathbf{n})\ \mathrm{d}a + \int_R \gamma \rho' \,\mathrm{d}v \tag{3.2}$$

The kinematics of the fluid are straightforward to state: incompressibility gives:

$$\nabla \cdot \mathbf{v} = \mathrm{tr}\,(\nabla \mathbf{v}) = 0 \tag{3.3}$$

which means that the stretching $\mathbf{D}$ is traceless:

$$\mathbf{D} = \frac{1}{2}\left(\nabla \mathbf{v} + \nabla \mathbf{v}^T\right) \tag{3.4}$$

The mass balance can then be written, introducing the notation $\Phi^\bullet$ to be the material derivative of the field Φ (also represented by

$$D\left(\Phi\right))$$

in some contexts). We observe that the the change of mass within a volume must be equal to the flux through the boundary of the volume:

$$\left\{\int_R \rho_b \,\mathrm{d}v\right\}^\bullet = -\int_{\partial R} \mathbf{h}_b \cdot \mathbf{n}\,\mathrm{d}a$$

Making use of the fact that the total density is constant and that the mass flux $\mathbf{h}$ of the two phases (usually referred to as 'a' and 'b') sums to zero we can write this locally in terms of the order parameter. This represents the local composition of the field, conventionally taken to represent the local fraction of phase 'a':

$$\phi^\bullet = -\nabla \cdot \mathbf{h} \tag{3.5}$$

Writing $\mathbf{T}$ as the macroscopic stress tensor and $\mathbf{n}$ the normal of the control volume's boundary, the momentum balances for linear and angular momentum take standard form:

$$\int_{\partial R} \mathbf{T}\mathbf{n}\,\mathrm{d}a = \left\{\int_R \rho\mathbf{v}\,\mathrm{d}v\right\}^\bullet \qquad \int_{\partial R} \mathbf{x}\times\mathbf{T}\mathbf{n}\,\mathrm{d}a = \left\{\int_R \left(\mathbf{x}\times\rho\mathbf{v}\right)\,\mathrm{d}v\right\}^\bullet,$$

equivalently in local form:

$$\nabla\cdot\mathbf{T} = \rho\mathbf{v}^\bullet \qquad \mathbf{T} = \mathbf{T}^T \tag{3.6}$$

The stress can be rewritten to make the connection to the pressure clear:

$$\mathbf{S} = \mathbf{T} + p\mathbf{I} \qquad p = -\frac{1}{3}\left(\mathrm{tr}\mathbf{T}\right)\mathbf{I}\,. \tag{3.7}$$

Returning to the microscopic force balance, we restrict our treatment to the isothermal case. We note that the second law of thermodynamics states that the rate of energy increase for any control volume R cannot exceed the sum of energy transported into R plus the working given by $\mathcal{W}$. Defining the chemical potential μ_b for phase b and the difference between the two phases as μ we can write the second law as the dissipation inequality:

$$\left\{\int_R \left(\phi + k\right)\,\mathrm{d}v\right\}^\bullet \leq \int_{\partial R} \mathbf{T}\mathbf{n}\cdot\mathbf{v}\,\mathrm{d}a + \int_{\partial R} \phi^\bullet\xi\,\mathrm{d}a - \int_{\partial R}\mu\mathbf{h}\cdot\mathbf{n}\,\mathrm{d}a\,.$$

The terms in the right-hand side of this equation represent the effects of the microscopic stress, the macroscopic stress, and the diffusion of energy in the form of chemical potential respectively. As a consequence of the local forms and the definition of the material derivative we have:

$$\phi^\bullet - \mathbf{T}\cdot\nabla\mathbf{v} + \left(\pi-\mu\right)\phi^\bullet + \xi\cdot\nabla\phi^\bullet + \mathbf{h}\nabla\mu \leq 0\,,$$

Making use of equations 3.6 and 3.7 we can rewrite this as:

$$\phi^{\bullet} - [\mathbf{S} + \nabla\phi \otimes \xi] \cdot \nabla\mathbf{v} + (\pi - \mu)\,\phi^{\bullet} + \xi \cdot (\nabla\phi)^{\bullet} + \mathbf{h} \cdot \nabla\mu \leq 0\,. \tag{3.8}$$

Constitutive relations are now required in order to close the problem, thankfully the dissipation inequality provides restrictions on the form these can take, we refer the reader to the original work for the detailed restriction and justification [84]. We assume that:

$$\mathbf{P} = 2\nu\mathbf{D}\,, \qquad \mathbf{h} = -m\nabla\phi\,, \qquad \psi = f(\phi) + \frac{1}{2}\alpha\,|\nabla\phi|^2\,, \tag{3.9}$$

where the mobility m, the viscosity ν, and the free energy α are taken to be non-negative constants and we have introduced P, the thermodynamic stress which is a conjugate of the stretching D.

$$\psi = f(\phi) + \frac{1}{2}\alpha\,|\nabla\phi|^2 \tag{3.10}$$

$$\mathbf{T} = -p\mathbf{I} + 2\nu\mathbf{D} - \alpha\nabla\phi \otimes \nabla\phi \tag{3.11}$$

$$\xi = \alpha\nabla\phi \tag{3.12}$$

$$\pi = \mu - f'(\phi) \tag{3.13}$$

$$\mathbf{h} = -m\nabla\mu \tag{3.14}$$

The term $\nabla\phi\otimes\nabla\phi$, which is sometimes known as the Korteweg stress tensor, represents normal stress in the absence of flow, and acts as a surface tension.

Cahn's formula for the chemical potential is apparent substituting the constitutive equation for π into the local microscopic balance, and the generalised Navier–Stokes and Cahn–Hilliard equations can also be found by making use of the constitutive relations. The extra term on the RHS of Equation 3.16 is a result of the Korteweg stress tensor mentioned above, all the other terms are classical.

$$\mu = f'(\phi) - \alpha\Delta\phi\,, \tag{3.15}$$

$$\rho\mathbf{v}^{\cdot} = -\nabla p + \nu\Delta\mathbf{v} - \alpha\,(\Delta\phi)\,\nabla\phi\,, \tag{3.16}$$

$$0 = \nabla\cdot\mathbf{v}\,, \tag{3.17}$$

$$\phi^{\cdot} = m\Delta\left[f'(\phi) - \alpha\Delta\phi\right]\,. \tag{3.18}$$

3.2.1 Non-dimensionalisation

The form of the CHNS equations derived from the microforce balance is useful for physical modelling, where measurement of physical quantities can be made, but this also hides the fundamental quantities that control the relative importance of physical phenomena. These physical quantities are summarised, together with their units, in table 3.2.1. In order to elucidate the parameters that control different effects we rewrite the equations in terms of dimensionless groups, highlighting the relative magnitude of the contributions from each

Quantity	Unit
Free Energy (α)	J
Chemical Potential (μ)	$J \cdot m^{-3}$
Phase-Field (ϕ)	$-$
Mobility (m)	$J^{-1} \cdot m^5 \cdot s^{-1}$
Surface Tension (σ)	$J \cdot m^{-2}$
Velocity ($\mathbf{v}$)	$m \cdot s^{-1}$
Pressure (P)	$N \cdot m^{-2}$
Mass Density $\left(\rho^1, \rho^2\right)$	$kg \cdot m^{-3}$
Viscosity $\left(\eta^1, \eta^2\right)$	$Pa \cdot s$

Table 3.1: Physical quantities and their dimensions in the Cahn–Hilliard Navier–Stokes system of equations

term.

We adopt a characteristic length, velocity, viscosity and chemical potential $\bar{L}, \bar{U}, \bar{\eta}, \bar{\mu}$, this allows us to rewrite the equations in terms of the rescaled variables:

$$\tilde{\mathbf{u}} = \frac{\mathbf{u}}{\bar{U}},\ \tilde{t} = \frac{t\bar{L}}{\bar{U}},\ \tilde{\mathbf{x}} = \frac{\mathbf{x}}{\bar{L}},\ \tilde{\nabla} = \bar{L}\nabla,\ \tilde{p} = \frac{p\bar{L}}{\bar{\eta_1}\bar{U}},\ \tilde{\mu} = \frac{\mu}{\bar{\mu}} \tag{3.19}$$

Cahn–Hilliard Equation

Making use of the definition of the material derivative we begin from Equation (3.13):

$$\frac{\partial \phi}{\partial t} + (\mathbf{u} \cdot \nabla)\, \phi = m\Delta\mu \tag{3.20}$$

we substitute the dimensionless quantities from Equation (3.19), and collect the terms:

$$\begin{aligned}
\frac{\bar{U}}{\bar{L}} \left[\frac{\partial \phi}{\partial \tilde{t}} + \left(\tilde{\mathbf{u}} \cdot \tilde{\nabla} \right) \phi \right] =& \frac{\bar{m}\bar{\mu}}{\bar{L}^2} \left[\tilde{\nabla}^2 \tilde{\mu} \right], \\
\frac{\partial \phi}{\partial \tilde{t}} + \left(\tilde{\mathbf{u}} \cdot \tilde{\nabla} \right) \phi =& \left(\frac{\bar{m}\bar{\mu}}{\bar{U}\bar{L}} \right) \bar{\nabla}^2 \tilde{\mu}, \\
\frac{\partial \phi}{\partial \tilde{t}} + \left(\tilde{\mathbf{u}} \cdot \tilde{\nabla} \right) \phi =& \left(\frac{1}{\mathrm{Pe}} \right) \bar{\nabla}^2 \tilde{\mu}.
\end{aligned} \tag{3.21}$$

The Péclet number (Pe) is identified as the controlling group in this equation, which represents the balance between the advection and diffusion. When the Péclet number is small the right hand side of the equation will dominate, reducing to steady diffusive transport, when it is large the right hand side will vanish, and the advection will dominate.

Cahn's Formula for Chemical Potential

Again making use of the formula for the material derivative, and rescaling the potential term appropriately we have:

$$\mu = \bar{\mu} f'(\phi) - \alpha \Delta \phi \,, \tag{3.22}$$

similarly substituting the dimensionless quantities from Equation (3.19) and collecting terms we obtain:

$$\begin{aligned} \bar{\mu}\tilde{\mu} =& \bar{\mu} f'(\phi) - \frac{\alpha}{\bar{L}^2}\tilde{\nabla}^2\phi \,, \\ \tilde{\mu} =& f'(\phi) - \frac{\alpha}{\bar{\mu}\bar{L}^2}\tilde{\nabla}^2\phi \,, \\ =& f'(\phi) - \frac{\xi^2}{\bar{L}^2}\tilde{\nabla}^2\phi \,, \\ =& f'(\phi) - \mathrm{Cn}^2\tilde{\nabla}^2\phi \,. \end{aligned} \tag{3.23}$$

The Cahn number is identified as the controlling group in this equation, it represents the balance between interfacial thickness and the characteristic length of the domain. Large values of this group favour wide interfaces, where the diffusive term dominates, for small values the potential term dominates, and the narrow interface experiences little smoothing.

Continuity Equation

The continuity equation can be rewritten directly, since any rescaling of the equation corresponds to a simple multiplicative constant for all terms:

$$\nabla \cdot \mathbf{u} = \tilde{\nabla} \cdot \tilde{\mathbf{u}} = 0 \tag{3.24}$$

Modified Navier–Stokes Equation

The modified Navier–Stokes equation requires slightly more remarks, replacing the material derivative and substituting dimensionless quantities as before we obtain the initial dimensionless equation:

$$\rho\left[\frac{\partial \mathbf{u}}{\partial t} + (\mathbf{u}\cdot\nabla)\,u\right] = -\nabla p + \eta\nabla^2\mathbf{u} + \alpha\nabla\phi \,, \tag{3.25}$$

$$\begin{aligned} \frac{\rho\bar{U}^2}{\bar{L}}\left[\frac{\partial \tilde{\mathbf{u}}}{\partial \tilde{t}} + \left(\tilde{\mathbf{u}}\cdot\tilde{\nabla}\right)\tilde{\mathbf{u}}\right] =& -\frac{\bar{\eta_1}\bar{U}}{\bar{L}^2}\tilde{\nabla}\tilde{p} + \frac{\eta\bar{U}}{\bar{L}^2}\tilde{\nabla}^2\tilde{\mathbf{u}} + \frac{\bar{\mu}}{\bar{L}}\tilde{\mu}\nabla\phi \,, \\ \left[\frac{\partial \tilde{\mathbf{u}}}{\partial \tilde{t}} + \left(\tilde{\mathbf{u}}\cdot\tilde{\nabla}\right)\tilde{\mathbf{u}}\right] =& -\frac{\bar{\eta_1}}{\rho\bar{U}\bar{L}}\tilde{\nabla}\tilde{p} + \frac{\eta}{\rho\bar{U}\bar{L}}\tilde{\nabla}^2\tilde{\mathbf{u}} + \frac{\bar{\mu}}{\rho\bar{U}^2}\tilde{\mu}\nabla\phi \,. \end{aligned} \tag{3.26}$$

Taking the pressure term from equation (3.26), we define the density ratio $\bar{\rho} = \frac{\rho}{\rho_1}$ and identify the Reynolds number Re:

$$\frac{\eta_1}{\rho_1\bar{U}\bar{L}}\frac{\rho_1}{\rho} = \frac{1}{\bar{\rho}\mathrm{Re}} \,. \tag{3.27}$$

Defining the corresponding viscosity ratio $\bar{\eta} = \frac{\eta}{\eta_1}$ the coefficient of the viscous term can we expressed as:

$$\frac{\eta}{\rho \bar{U} \bar{L}} = \frac{\eta_1}{\rho_1 \bar{U} \bar{L}} \frac{\eta}{\eta_1} \frac{\rho_1}{\rho}\,, \tag{3.28}$$

$$= \frac{1}{\bar{\rho} \mathrm{Re}} \bar{\eta}\,. \tag{3.29}$$

For the interfacial energy term we obtain:

$$\frac{\bar{\mu}}{\rho \bar{U}^2} = \frac{1}{\bar{\rho} \mathrm{Re}} \frac{\bar{\mu} \bar{L}}{\eta_1 \bar{U}} \tag{3.30}$$

The surface tension enters via the parameter $\bar{\mu}$. Solving the Cahn–Hilliard equation in one dimension gives and expression for the interface profile, and this can be used to obtain the effective surface tension. Making use of this fact we obtain:

$$\begin{aligned} \frac{\bar{\mu}}{\rho \bar{U}^2} =& \frac{1}{\bar{\rho} \mathrm{Re}} \frac{\bar{\mu} \bar{L}}{\eta_1 \bar{U}}\,, \\ =& \frac{3}{2\sqrt{2}} \frac{1}{\bar{\rho} \mathrm{Re}} \frac{\bar{\sigma}}{\eta_1 \bar{U}} \frac{\bar{L}}{\xi}\,, \\ =& \frac{3}{2\sqrt{2}} \frac{1}{\bar{\rho} \mathrm{Re}} \frac{1}{\mathrm{Ca}} \frac{1}{\mathrm{Cn}}\,. \end{aligned} \tag{3.31}$$

The remaining dimensionless quantity we introduce is the capillary number $\mathrm{Ca} = \frac{\eta_1 \bar{U}}{\bar{\sigma}}$, this controls the balance between viscous forces and the surface tension. Small values of this group lead to large surface tensions, and the fluid is strongly convected by surface effects, large values effectively decouple the velocity field from the phase.

In our simulations and analysis we assume that both phases have identical viscosity and density, this reduces the generality of the model somewhat, but is a common assumption to make in the literature. We therefore take $\bar{\rho}$ and $\bar{\eta}$ to be one. The relative magnitudes of the viscosity and density will still enter the equations through the dimensionless groups.

The system of equations is thus parameterised by three dimensionless groups, these are summarised in the table below. The final dimensionless equations to be studied are presented below, we have dropped the tildes, and now assume that all quantities are their dimensionless equivalents.

Table 3.2: Dimensionless groups that control the behaviour of the Cahn–Hilliard Navier–Stokes equations, together with the balance of physical quantities they represent.

Name	Symbol	Balance	Expression
Reynolds' Number	Re	Viscous Forces - Inertial Forces	$\rho_1 \bar{U} \bar{L} / \bar{\eta_1}$
Cahn Number	Cn	Interfacial Length - Fluid Length	$\xi / \bar{L}$
Capillary Number	Ca	Viscous Forces - Surface Tension	$\eta_1 \bar{U} / \bar{\sigma}$

$$\frac{\partial \phi}{\partial t} + (\mathbf{u} \cdot \nabla)\, \phi = \left(\frac{1}{\mathrm{Pe}} \right) \nabla^2 \mu \,, \tag{3.32}$$

$$\mu = f'(\phi) - \mathrm{Cn}^2 \nabla^2 \phi \,, \tag{3.33}$$

$$\nabla \cdot \mathbf{u} = 0 \,, \tag{3.34}$$

$$\left[\frac{\partial \mathbf{u}}{\partial t} + (\mathbf{u} \cdot \nabla)\, \mathbf{u} \right] = -\frac{1}{\mathrm{Re}} \nabla p + \frac{1}{\mathrm{Re}} \nabla^2 \mathbf{u} + \frac{1}{\mathrm{Re}\,\mathrm{Ca}\,\mathrm{Cn}} \mu \nabla \phi \,. \tag{3.35}$$

3.3 Problem Formulation

The channel is taken to be a periodic channel in the x-direction, symmetrical about the x-axis with the upper wall given by the equation $y_{upper} = 1 + \varepsilon \cos kx$. By varying the values of k and ε we can control the strength and frequency of corrugations in the channel, this geometry is shown below in Figure 3.1.

Initial numerical simulations (See 3.4), suggest that we expect to observe:

1. Slug flow: Where phase A extends from the upper to the lower wall for some length of the channel, capped with circular section interfaces with phase B.
2. Droplet flow: Some volume of phase A is enclosed entirely by phase B, the interface is then a circle.
3. Stratified flow: A layer of phase A extends along the entire channel, separated from either wall by phase B, the interface is then two straight sections.

It is worth noting that the stratified case is only observed because the domain is periodic, we can imagine that the flow is confined to a very thin annular layer between two cylinders, like for Couette flow. This means that the interface between the two fluids has a finite length, and hence the morphology has finite energy.

3.3.1 Static Energy Analysis

In order to obtain an initial idea of the flow patterns we will encounter we formulate a simple model of the channel and suggest that the likelihood of

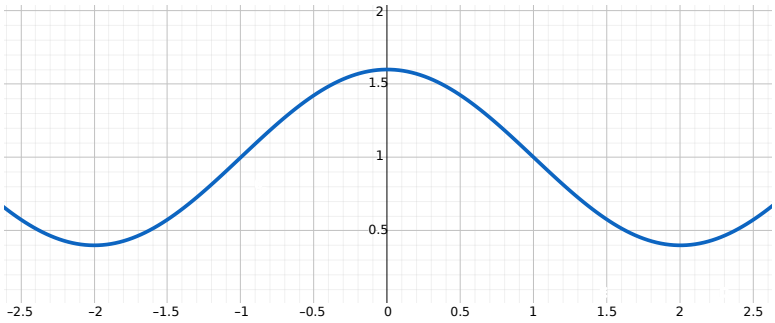

Figure 3.1: Half-channel geometry, $\varepsilon = 0.6$, channel is mirrored about the x-axis and periodic in the x-direction.

observing a state is inversely proportional to its interfacial energy. We assume that the geometry of the droplet is unaffected by the velocity, or rather that the capillary number (Ca) is small. This enables us to extract the interfacial energy as a function of the droplet's size and position, predicting the most likely morphology, as well as the energy barrier to flow down the channel.

Slug flow

The interfacial energy of the slug is a function of the interface length, both between phase A and phase B, and between phase A and the wall. This is a function of the volume and position of the droplet. We define the droplet position by its centre of mass, or barycentre, as the droplet will be asymmetrical throughout most of the channel. The profile we construct is shown in Figure 3.2.

The shape of each circular interface is found by taking some location z as the contact point between phase A and phase B. The apparent contact angle θ_a is found as a function of the static contact angle θ_0 by observing that it is related to the angle of the wall to the horizontal at z (θ_w):

$$\theta_a = \theta_0 - \theta_w \tag{3.36}$$

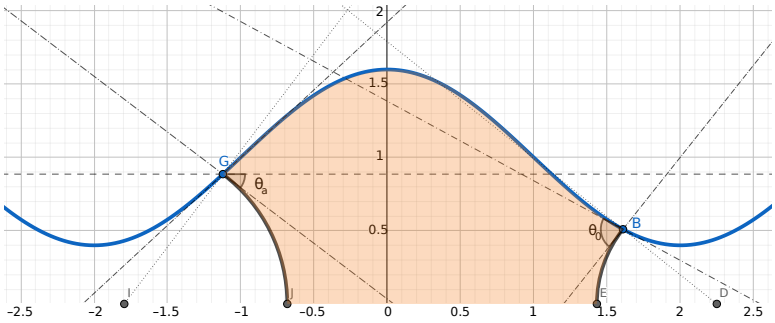

Figure 3.2: Construction of the slug geometry. Contact points at B and G, static contact angle θ_0, apparent contact angle θ_a. Centres of circular sections at D and I, radii of sections given by DE and IJ

where:

$$\theta_w = \arctan\left(k\varepsilon \sin kz\right) \tag{3.37}$$

The area and arc length of the circular cap are related to the radius and the angle subtended, the angle is found by observing that the apparent contact angle and the subtended angle form a right angle, and so:

$$\theta_s = \frac{\pi}{2} - \theta_a \tag{3.38}$$

The radius can be found by substituting the location of the contact point into the equations of a circle centred at some z_0 with unknown radius r:

$$\begin{aligned} z =& z_0 + pr\cos\theta_s\,, \\ 1 + \varepsilon\cos kz =& r\sin\theta_s\,, \end{aligned}$$

thus, making use of standard trigonometric identities:

$$z_0 = z - pr\sin\theta_a\,, \tag{3.39}$$

$$r = \frac{1+\varepsilon\cos kz}{\cos\theta_a}\,, \tag{3.40}$$

where we have defined p in the first equation as the convexity of the interface: specifically it is the value of sign $\left[\theta_a - \frac{\pi}{2}\right]$. When p is equal to 1 the interface is convex, when it is equal to -1 it is concave.

The volume and arc length can then be computed using the standard formulae, these give:

$$V_r = p \left| \frac{(1 + \varepsilon \cos kz)^2}{4 \cos^2 \theta_a} \left(2 \left(\theta_a - \frac{\pi}{2} + \sin 2\theta_a \right) \right) \right| , \tag{3.41}$$

$$s_r = 2 \frac{\left(\theta_a - \frac{\pi}{2}\right) (1 + \varepsilon \cos kz)}{\cos \theta_a} . \tag{3.42}$$

A result of using the static contact angle is that the left and right circular caps are given by slightly different expressions. We use the above equations Eqs. (3.36)-(3.41) directly for the right-hand end of the slug, but must modify them for the left-hand end. As we measure the contact angle in the opposite sense we must replace θ_0 by $\pi - \theta_0$:

$$\theta_{a,r} = \pi - \theta_0 - \theta_w , \tag{3.43}$$

we also must reverse the sign in Equation (3.40) for z_0 as convexity now corresponds to the interface left of the contact point rather than right of it:

$$z_0 = z + pr \sin \theta_{a,r} . \tag{3.44}$$

The area of the central section and the length of the phase A - wall interface are both found by integration directly:

$$\begin{aligned} V_c =& 2 \int_{z_l}^{z_r} y \, \mathrm{dx} \\ =& 2 \int_{z_l}^{z_r} (1 + \varepsilon \cos kx \, \mathrm{d}x) \\ =& 2 (z_r - z_l) + \frac{2\varepsilon}{k} (\sin kz_r - \sin kz_l) , \end{aligned} \tag{3.45}$$

$$\begin{aligned} s_c =& 2 \int_{z_l}^{z_r} \sqrt{1 + \left(\frac{dy}{dx} \right)^2} \, \mathrm{d}x \\ =& 2 \int_{z_l}^{z_r} \sqrt{1 - \frac{\varepsilon^2}{k^2} \sin^2 kx} \, \mathrm{d}x \\ =& \frac{2}{k} \left(\mathrm{E} \left(kz_r, \frac{\varepsilon}{k} \right) - \mathrm{E} \left(kz_l, \frac{\varepsilon}{k} \right) \right) , \end{aligned} \tag{3.46}$$

where we have made use of the definition of $\mathrm{E}(\varphi, k)$ as the incomplete elliptic integral of the second kind.

From Equations (3.42) and (3.46) we can compute the interfacial energy, by choosing an appropriate scaling we have that:

$$\begin{aligned}\gamma =& s_l + s_r - 2s_c \cos\theta_0 \\ =& 2\frac{\left(\theta_{a,l} - \frac{\pi}{2}\right)(1+\varepsilon\cos kz_l)}{\cos\theta_{a,l}} \\ &+ 2\frac{\left(\theta_{a,r} - \frac{\pi}{2}\right)(1+\varepsilon\cos kz_r)}{\cos\theta_{a,r}} \\ &- \frac{4\cos\theta_0}{k}\left(\mathrm{E}\left(kz_r,\,\frac{\varepsilon}{k}\right) - \mathrm{E}\left(kz_l,\,\frac{\varepsilon}{k}\right)\right).\end{aligned} \tag{3.47}$$

In order to permit comparison of slugs with droplets and stratified flow we need to find the locations of the contact lines as a function of the centre of mass of the slug and its volume. This means we must solve two equations to find the values of z_l and z_r, and hence the interfacial energy.

Firstly the volume of the droplet is defined as the sum of the contributions from the different pieces, two end caps and the slug body:

$$\begin{aligned}0 =& V_r + V_l + V_c - V \\ =& p_r\left|\frac{(1+\varepsilon\cos kz_r)^2}{4\cos^2\theta_{a,r}}\left(2\left(\theta_{a,r} - \frac{\pi}{2} + \sin 2\theta_{a,r}\right)\right)\right| \\ &+ p_l\left|\frac{(1+\varepsilon\cos kz_l)^2}{4\cos^2\theta_{a,l}}\left(2\left(\theta_{a,l} - \frac{\pi}{2} + \sin 2\theta_{a,l}\right)\right)\right| \\ &+ 2(z_r - z_l) + \frac{2\varepsilon}{k}(\sin kz_r - \sin kz_l) \\ &- V\,.\end{aligned} \tag{3.48}$$

In order to impose the centre of mass we need to compute the centres of mass for each section, for the end caps we use the standard result for the centroid of a circular segment:

$$\begin{aligned}\bar{x} =& \frac{4r\sin^3(\theta_s)}{3(2\theta_s - \sin(2\theta_s))} \\ =& \frac{4(1+\varepsilon\cos kz)\cos^2(\theta_a)}{3(\pi - 2\theta_a - \cos(2\theta_a))}\,.\end{aligned} \tag{3.49}$$

For the central slug section we integrate to find the moment of the shape and

divide by the mass, which is equivalent to the volume, to obtain the centroid:

$$\begin{aligned}\bar{x} =& \frac{1}{V}\int_{z_l}^{z_r} xy\left(x\right)\,\mathrm{d}x \\ =& \frac{1}{V}\int_{z_l}^{z_r} x + \varepsilon x\cos(kx)\mathrm{d}x \\ =& \frac{1}{V}\left(\frac{1}{2}\left(z_r^2 - z_l^2\right) + \frac{\varepsilon}{k}\left(z_r\sin kz_r - z_l\sin kz_l\right) + \frac{\varepsilon}{k^2}\left(\cos kz_r - \cos kz_l\right)\right).\end{aligned} \tag{3.50}$$

The barycentre of the slug is then found as the sum of each moment divided by the total mass, setting this equal to the desired location provides the second equation to close the problem:

$$\begin{aligned}0 =& \bar{x} - \bar{Z} \\ =& \frac{V_l\bar{x}_l + V_r\bar{x}_r + V_c\bar{x}_c}{V_l + V_r + V_c} - \bar{Z}\,.\end{aligned} \tag{3.51}$$

When the value of ε is large we observe that, for small volumes, the two circular interfaces meet. This means that at that regime, slug flow is not possible, instead the slug will split into two wetted droplets.

This will happen at the widest part of the channel, so the problem reduces to finding a point such that $r = z_0$:

$$\begin{aligned}0 =& z_0 - r \\ =& z_r - p_r r\sin\theta_{a,r} - \frac{1+\varepsilon\cos kz_r}{\cos\theta_{a,r}} \\ =& \frac{z_r}{1+\varepsilon\cos kz_r} + \frac{\sin\theta_a - 1}{\cos\theta_a}\,.\end{aligned} \tag{3.52}$$

The critical volume for which the slug is physically feasible is then computed using Equation (3.48), assuming the slug is symmetrical about the y-axis, such that $z_l = -z_r$.

Droplet Flow

Droplet flow is much more straightforward to analyse, we note that there can be an infinite number of droplets formed (the regime known as bubbly flow), but these have a higher energy than a single large drop. This is because a circle is the shape that minimises the perimeter for a given volume.

The circumference of a circle with given area is trivially found as:

$$s = 2\sqrt{\pi V}\,. \tag{3.53}$$

We observe that there is a physical limitation to the size of the droplet: the diameter of the droplet cannot exceed the minimal width of the channel. This

suggests that there are some regions where the higher energy of a multiple-droplet state would be favourable, as a single droplet would be too large. The maximal droplet volume is also trivially found:

$$\begin{aligned} r &< \min\left(1 + \varepsilon \cos kx\right) \\ &< (1 - \varepsilon) \\ V &< \pi \left(1 - \varepsilon\right)^2 . \end{aligned} \tag{3.54}$$

Stratified Flow

Stratified flow is stable statically in periodic domains and in channels with ends. With flow it is only stable in periodic domains, for N_I fluid-fluid interfaces its energy is identified as the length of the periodic domain L_{periodic}:

$$s = N_I L_{\text{periodic}} . \tag{3.55}$$

Energy results

Initially we investigate the effect of slug volume on the interfacial energy. We fix the slug's location at the origin and the contact angle as $\frac{\pi}{2}$, we then vary the volume repeatedly solving the equations to compute the contact points and the interfacial energy.

Very quickly we discovered that the equations permit multiple solutions: for some given volume there can be multiple corresponding contact points. In order to find all the possible solutions we adopted a numerical continuation approach. Solving the equation with different starting points would have been another valid approach, but the continuation method offers various advantages, including easy adaptation of the step size and a simpler algorithm overall. We elected to implement Moore–Penrose continuation, also known as Gauss–Newton continuation.

Moore–Penrose is a predictor-corrector method: from some previous solution the algorithm predicts the next solution by a linear step; a Newton solver is then used to correct the prediction. Moore–Penrose makes use of a matrix pseudo-inverse of the same name to make this corrector step quicker to evaluate [4, 126].

Solving the equations using this continuation method reveals the behaviour mentioned, for small channel perturbations ($\varepsilon < 0.7$) the droplet monotonically extends. For larger perturbations multiple configurations with equal volume exist in the vicinity of the widest part of the channel.

The bifurcation corresponds to a region where the droplet interface locally reverses direction: a local maximum volume is reached and it must be decreased to continue the motion of the contact line. It then reverses again and increases with increasing volume. The three coexisting states are shown in Figure 3.5: physically the transition across this would be discontinuous, upon reaching the lower limit point the system would transition to the corresponding state on the

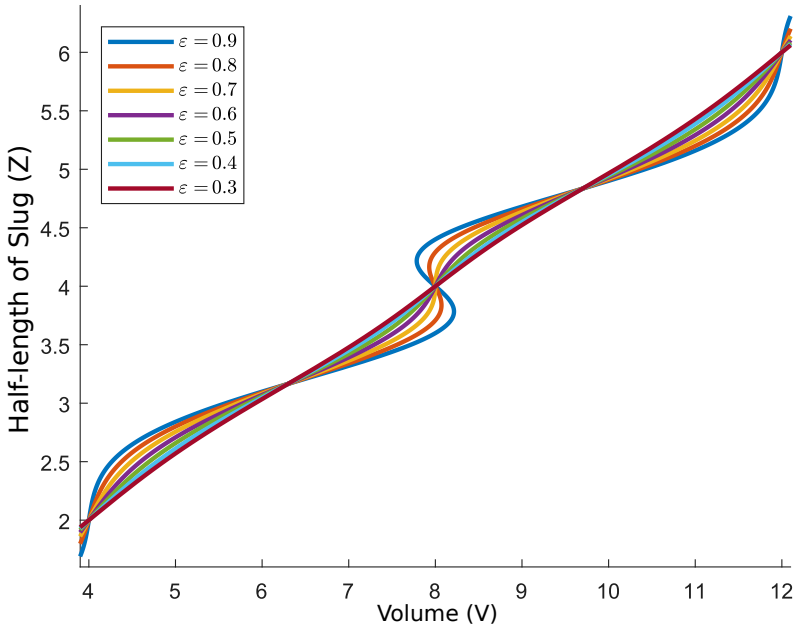

Figure 3.3: Location of right contact line, equivalently half-length of slug, as a function of slug volume. Colours correspond to different values of ε

branch directly above. In reverse the system would reach the upper limit point before dropping to the branch below.

The interfacial energy here shows the same bifurcation, but with a different profile, here a complex cusp is observed: the upper and lower branch in Figure 3.5 have equal energy and correspond to the point where the curves cross, the two cusps correspond to the limit points in Figure 3.5, and the local minimum energy corresponds to the central unstable state.

The bifurcation is controlled by the parameter ε, and it has a critical value ε_c. This corresponds to the minimum perturbation such that the interface undergoes this discontinuous motion. In order to find this value we compare the change in volume of the central slug section and the end caps (Equations 3.41 and 3.45).

A first order Taylor expansion in the parameter ε gives a critical value of $\varepsilon_c = 0.711$.

To confirm this value we use two-parameter continuation in ε and V: beginning at one of the limit points in Figure 3.5 we allow Z and ε to vary, we then move across the bifurcation surface until the limit points coincide. This happens when $\varepsilon \approxeq 0.71$, which confirms that our first-order expansion can correctly predict the cusp location and therefore the critical value of ε. As long as the

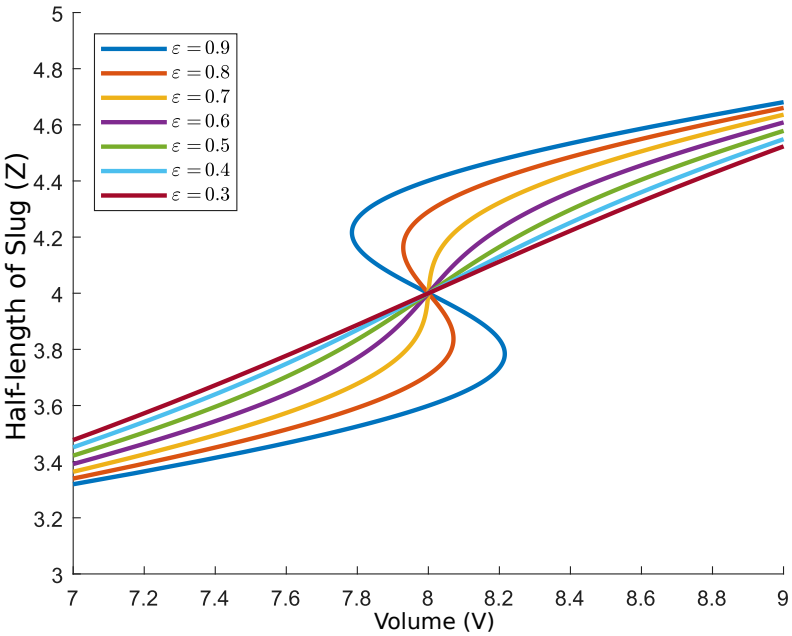

Figure 3.4: Same as Figure 3.3, zoomed on pitchfork bifurcation. Critical value of ε appears to be approximately 0.7

perturbations are less than this value we expect the interface location to vary smoothly; if we increase the perturbation above this value then the interface location will jump discontinuously.

Away from the origin the droplet is no longer symmetric, fixing the channel corrugation at a moderate value ($\varepsilon = 0.5$) we follow the droplet profile as it passes through the channel and we compute the total interfacial energy. With the contact angle $\theta_0 = \frac{\pi}{2}$ the Solid-Liquid energy is zero, so the energy profiles will be periodic in V.

The energy results suggest that the resistance to flow is related to the droplet volume, volumes that correspond to odd multiples of 2 (when the contact lines are precisely out of phase) minimise this barrier, and even multiples (when they are precisely in phase) maximise it: this is shown below in Figure 3.9.

Sampling droplet and slug energies for each volume and value of ε enables us to plot a phase diagram. We observe that for large volumes we are unable to form single droplets; here we either expect to observe multiple droplets, which complicates analysis, or slugs. We also expect to observe multiple droplets when ε is large and the volume is small; here the volume is below the critical volume and the slug will destabilise.

Where both slug and droplet flow are possible (below the blue line), slugs

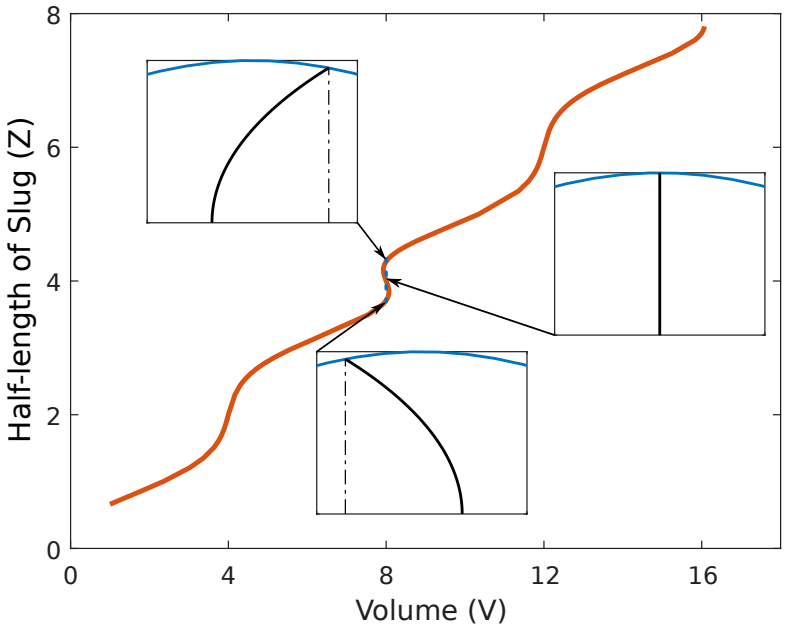

Figure 3.5: Location of right contact point, equivalently the half-length, as a function of volume for $\varepsilon = 0.8$. Insets show coexisting states along the dashed line, top and bottom are stable states, centre is unstable.

are more stable for low values of ε (in the green region). For larger values of ε the droplets are more stable than slugs at some points in the channel and less in others, and both droplets and slugs are therefore feasible (the yellow region). For very large values of ε slugs will separate into two when the channel is at its widest, and so here droplets are preferred (the blue region). Above the blue line the droplets would be too large to pass down the channel without colliding with the wall and forming slugs (the cyan region), or neither are feasible and multiple droplets must be formed (the orange region).

Equipped with this energy-based model we can predict what flow morphology we should observe for a given set of parameters, assuming that the flow velocity and, more importantly, the flow velocity gradient, is small. Larger velocity gradients will cause shear in the droplets and will increase the interface length, increasing the interfacial energy.

3.3.2 Numerical Methods

In one-dimension the non-convective Cahn–Hilliard equation Equation (4.17) can be solved analytically, however in two or more dimensions, or where convection is included, this is impossible and the equations must be solved numerically.

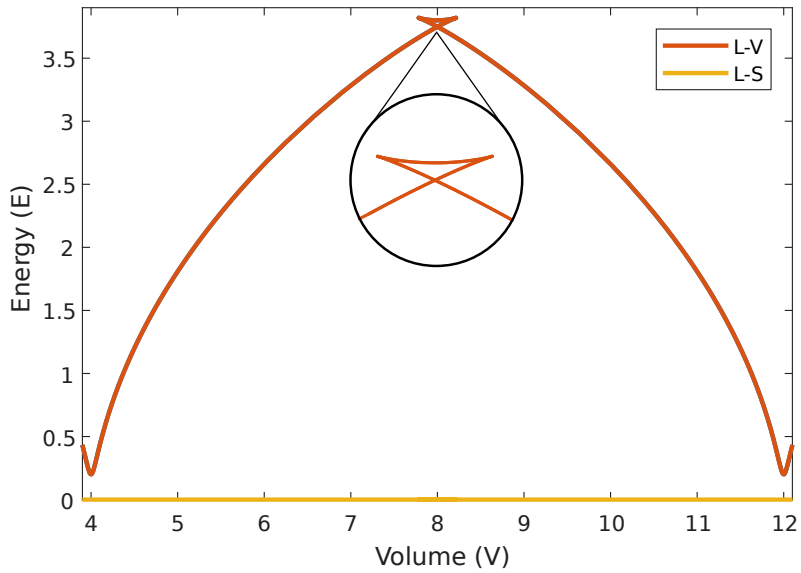

Figure 3.6: Interfacial energy as a function of slug volume for $\varepsilon = 0.8$. Pitchfork bifurcation in Figure 3.5 corresponds to a symmetric bifurcation with two cusps. Solid-Liquid interfacial energy is zero due to the contact angle.

The time dependant PDE requires a time-stepping scheme and the domain to be discretised in some fashion.

Many approaches have been used to solve the equations in the literature including classical Finite-Difference, Finite-Volume, and Spectral Methods. We discarded a Spectral Approach as we intend to simulate complex geometries for confinement, spectral methods require a smooth mapping from a square or circular domain to the domain in question. They would offer increased accuracy in simple geometries though, and they have been used widely in the literature. Finite-Difference methods are appealing for their simplicity, and they are more able to handle complex geometries, but we know that the CHNS equations tend to favour solutions with large local changes in ϕ with large areas of little interest. We therefore would like to make use of adaptive meshing to accelerate our solution, this is complex and requires manual implementation in finite-difference schemes, particularly for complex boundaries and boundary conditions.

We elected to use a Finite-Element method as it allows for arbitrarily complex geometries and boundary conditions as well as allowing for mesh adaptation.

Beginning with the non-dimensional formulation of the Cahn–Hilliard Navier–Stokes equations we must relax our problem in such a way that we can find a solution with a Finite-Element method. In the original formulation, known as the Strong Form in the language of Finite-Element solutions, we cannot hope to

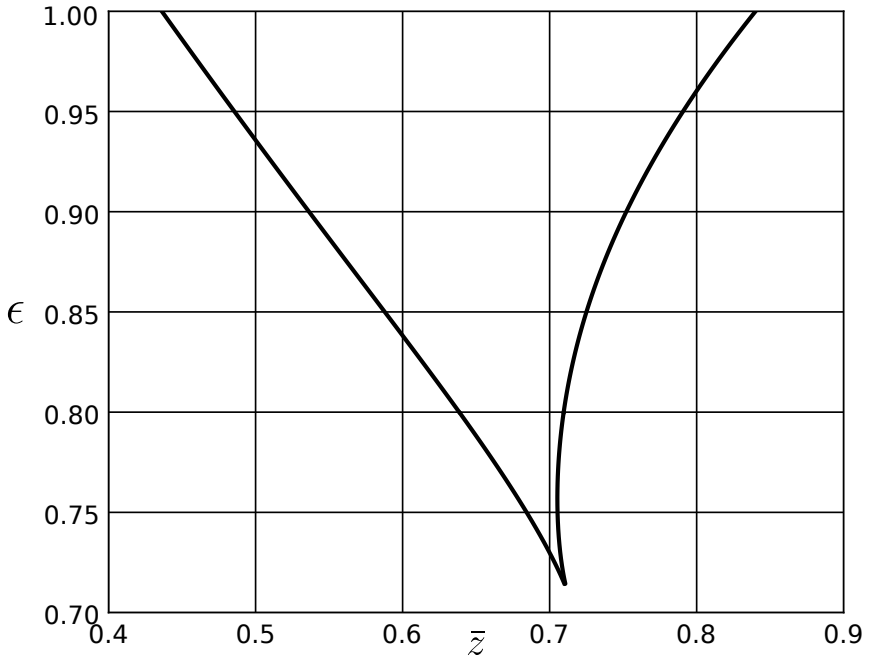

Figure 3.7: Locus of a pair of limit points from Figure 3.5 for varying ε. Shows a cusp at approximately 0.71

solve our equations with functions that are piecewise polynomial. They will have undefined derivatives in places, and unless we are careful will have insufficient continuous derivatives, we are doomed to fail.

However if we introduce a set of "test functions" from an appropriate function space we can reformulate our equations in such a way that the continuity requirements are lifted. It turns out that this procedure allows us to naturally satisfy Neumann boundary conditions within the equations themselves. We note that Dirichlet conditions need to be enforced by manipulating the equations, but this turns out to be straightforward.

Chorin's Method for Time-Stepping

We need to formulate a strategy to compute the velocity field at each time-step. The Navier–Stokes equations are not straightforward to solve in general, and in particular the presence of the convective term $(u \cdot \nabla)\, u$, when the Reynolds number is not small, lead to issues with numerical stability. We adopt a classical approach to treat the Navier–Stokes equations, which is modified to allow solution where the interfacial stress has been coupled.

Chorin's method is a splitting scheme that separates the velocity updates

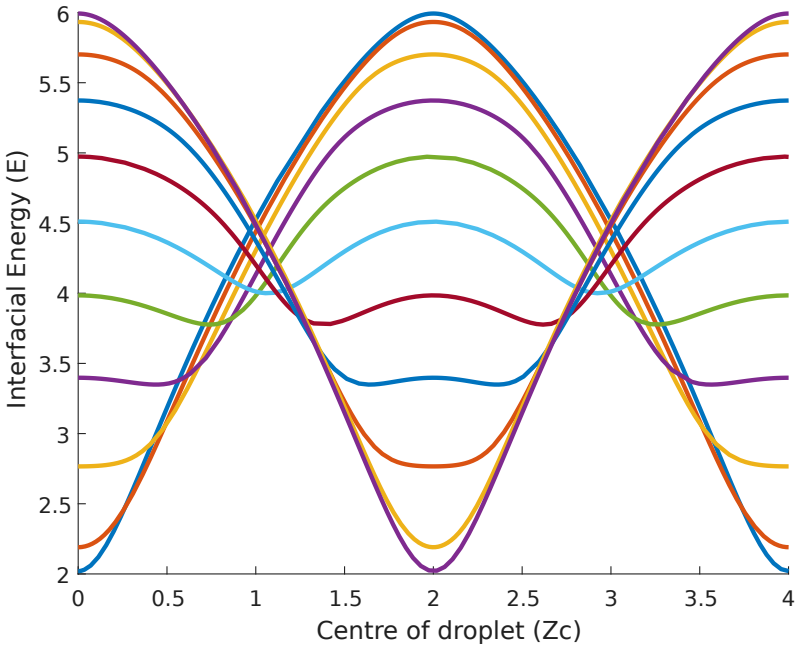

Figure 3.8: Interfacial energy as a function of slug centre for varying slug volume (Top Purple - $V = 4$, Bottom Blue - $V = 8$)). Difference between maximal and minimal energy corresponds to a resistance to flow.

into two contributions, a projection is made ignoring the pressure field, and this is then corrected by computing a new pressure field [39],[40]. Euler's method is usually adopted in time, but this can be implemented with more accurate time-stepping scheme. We elect to use Euler's method to reduce complexity in implementation and to improve simulation speed.

Formally we adopt the following scheme:

1. Compute velocity prediction.

$$\frac{\mathbf{u}^* - \mathbf{u}^n}{\Delta t} = -\left(\mathbf{u}^n \cdot \nabla\right)\mathbf{u}^n + \frac{1}{\mathrm{Re}}\Delta\mathbf{u}^n + \frac{1}{\mathrm{ReCaCn}}\mu\nabla\phi\,. \tag{3.56}$$

2. Compute updated pressure

$$\Delta p^{n+1} = \frac{1}{\Delta t}\nabla\cdot\mathbf{u}^*\,. \tag{3.57}$$

3. Correct intermediate velocity

$$\mathbf{u}^{n+1} = \mathbf{u}^* - \frac{1}{\mathrm{Re}}\Delta t\nabla p^{n+1}\,. \tag{3.58}$$

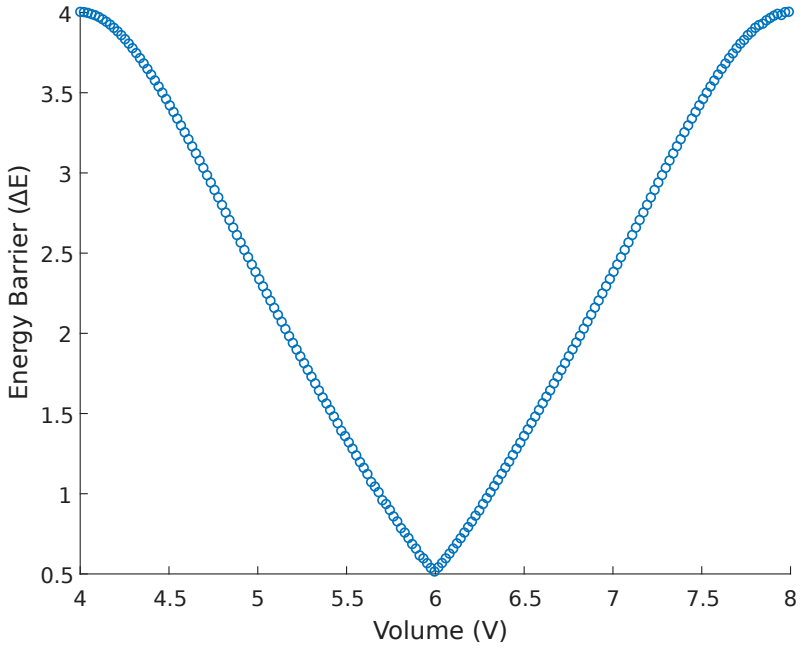

Figure 3.9: Interfacial energy barrier as a function of slug volume for $\varepsilon = 0.8$. Minimum energy barrier is observed for volumes that are odd multiples of 2, and the maximum barrier for even multiples of 2.

Operator Splitting Scheme for Cahn–Hilliard

The Cahn–Hilliard equation is also nonlinear, for any physically relevant form of the free-energy gradient term. From the application of regular solution theory, thermodynamic arguments suggest a free-energy incorporating the reduced temperature of the form [142]:

$$F(\phi) = \frac{\Theta}{2}\left[\phi \ln \phi + (1-\phi)\ln(1-\phi)\right] + \alpha\phi(1-\phi) \ . \tag{3.59}$$

This is difficult to work with as the potential is degenerate outside the region $(0, 1)$ (it is undefined at $\phi = 0$ and $\phi = 1$), additionally the multiple logarithmic terms make the evaluation at each time step computationally expensive. Instead, most authors adopt a similarly shaped quartic potential of the form:

$$F(\phi) = (\phi + 1)^2 (\phi - 1)^2 \tag{3.60}$$

This recovers qualitatively the same behaviour – two distinct phases in the low temperature regime, but has the advantage of continuity everywhere and at much reduced computational complexity.

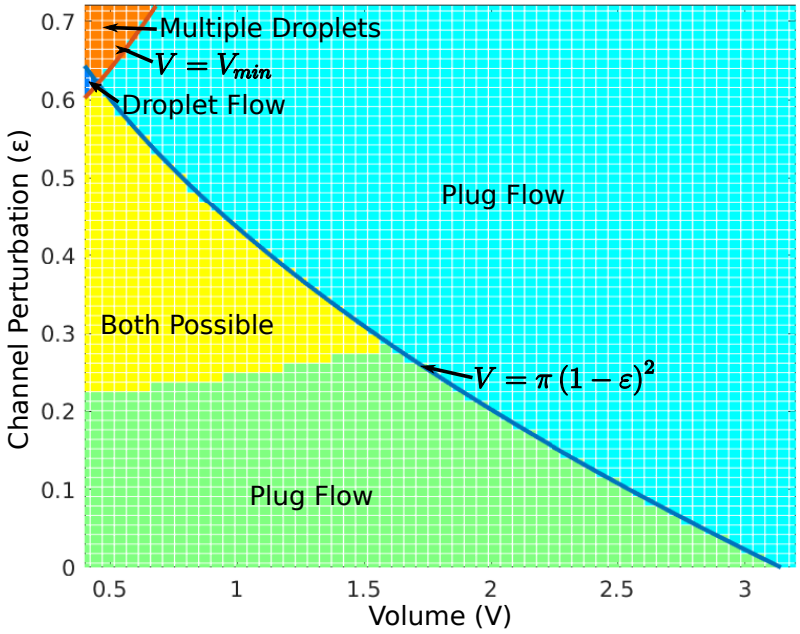

Figure 3.10: Phase plane portrait showing energy levels for different flow morphology

Explicit solution of this system, even with the polynomial free-energy, is impossible due to the stiffness of the equations at the interface ([106] amongst others), instead impliict schemes must be used which are computationally expensive. Fortunately the wide range of studies with Cahn–Hilliard models has led to much development in numerical schemes to handle this nonlinearity, and an excellent survey is given by Tierra and Guillén-González [170]. We adopt the OD2 method for its computational simplicity and accuracy without much comment, higher order methods offer little advantage, as our temporal and spatial convergence is limited by the Navier–Stokes solver.

The OD2 scheme, like several related schemes, splits the polynomial into a convex and concave part, the concave part is handled implicitly, and the convex explicitly. The splitting scheme is given below:

$$\phi\left(\phi^2 - 1\right) = \frac{1}{2}\left(\phi_n^2 \phi_{n+1} - \phi_{n+1}\right) . \tag{3.61}$$

Finite-Element Formulation

We introduce the test functions θ and ν corresponding to the trial functions ϕ and μ in the Cahn–Hilliard equation, and we introduce the test functions w and

q corresponding to the trial functions u and p

$$0 = \frac{\partial \phi}{\partial t}\rho - \frac{1}{\mathrm{Pe}}\Delta(\mu)\,\nu\,, \tag{3.62}$$

$$0 = \mu\nu - F'(\phi)\,\rho + \mathrm{Cn}^2\Delta(\phi)\,\rho\,, \tag{3.63}$$

$$\frac{\partial \mathbf{u}}{\partial t}\mathbf{w} + (\mathbf{u}\cdot\nabla)(\mathbf{u})\,\mathbf{w} = -\frac{1}{\mathrm{Re}}\nabla(p)\,q + \frac{1}{\mathrm{Re}}\nabla^2(\mathbf{u})\,\mathbf{w} + \frac{1}{\mathrm{Re}\,\mathrm{Ca}\,\mathrm{Cn}}\mu\nabla(\phi)\,\nu\,. \tag{3.64}$$

These equations are then integrated across an arbitrary domain:

$$0 = \int_R \frac{\partial \phi}{\partial t}\rho\,dx - \frac{1}{\mathrm{Pe}}\int_R \Delta(\mu)\,\nu\,dx\,, \tag{3.65}$$

$$0 = \int_R \mu\nu\,dx - \int_R F'(\phi)\,\rho\,dx + \mathrm{Cn}^2\int_R \Delta(\phi)\,\rho\,dx\,, \tag{3.66}$$

$$\int_R \frac{\partial \mathbf{u}}{\partial t}\mathbf{w}\,\mathrm{d}x + \int_R (\mathbf{u}\cdot\nabla)(\mathbf{u})\,\mathbf{w}\,\mathrm{d}x = -\frac{1}{\mathrm{Re}}\int_R \nabla(p)\,q\,\mathrm{d}x + \tag{3.67}$$

$$\frac{1}{\mathrm{Re}}\int_R \nabla^2(\mathbf{u})\,\mathbf{w}\,\mathrm{d}x + \frac{1}{\mathrm{Re}\,\mathrm{Ca}\,\mathrm{Cn}}\int_R \mu\nabla(\phi)\,\nu\,\mathrm{d}x\,. \tag{3.68}$$

In order to decouple the test functions from the trial functions in the second derivative terms we integrate those terms by parts:

$$0 = \int_R \frac{\partial \phi}{\partial t}\rho\,dx + -\frac{1}{\mathrm{Pe}}\int_R \frac{\partial \mu}{\partial x}\frac{\partial \nu}{\partial x}\,dx - \left[\frac{1}{\mathrm{Pe}}\frac{\partial \mu}{\partial x}\nu\right]_{\partial R}\,, \tag{3.69}$$

$$0 = \int_R \mu\nu\,dx - \int_R F'(\phi)\,\rho\,dx - \mathrm{Cn}^2\int_R \frac{\partial \phi}{\partial x}\frac{\partial \rho}{\partial x}\,dx + \left[\mathrm{Cn}^2\frac{\partial \phi}{\partial x}\rho\right]_{\partial R}\,, \tag{3.70}$$

$$\int_R \frac{\partial \mathbf{u}}{\partial t}\mathbf{w}\,\mathrm{d}x = -\int_R (\mathbf{u}\cdot\nabla)(\mathbf{u})\,\mathbf{w}\,\mathrm{d}x - \frac{1}{\mathrm{Re}}\int_R \nabla(p)\,q\,\mathrm{d}x + \frac{1}{\mathrm{Re}}\int_R \frac{\partial \mathbf{u}}{\partial x}\frac{\partial \mathbf{w}}{\partial x}\,\mathrm{d}x \tag{3.71}$$

$$-\left[\frac{1}{\mathrm{Re}}\frac{\partial \mathbf{u}}{\partial x}\mathbf{w}\right]_{\partial R} + \frac{1}{\mathrm{Re}\,\mathrm{Ca}\,\mathrm{Cn}}\int_R \mu\nabla(\phi)\,\nu\,\mathrm{d}x\,.$$

The time-stepping scheme and the splitting schemes for the equations can now bw implemented, and this form of equations is amenable to solution by standard finite-element methods.

Boundary Conditions

The boundary conditions in this model are physically motivated, we investigate the flow of fluids within a channel that we assume to be periodic, so we have the following

1. The channel is taken to be periodic in x

$$\mathbf{u}(0,y) = \mathbf{u}(L_x,y)\,,\; p(0,y) = p(L_x,y)\,,\; \phi(0,y) = \phi(L_x,y)\;.$$

2. The walls of the channel are solid and permit no flow through them, we also enforce no-slip

$$\mathbf{u} = 0 \quad \text{on}\,\partial R\,.$$

3. The contact angle is fixed on the wall as θ_0

$$\nabla\phi\cdot\hat{n} = -\frac{\sqrt{2}}{2\mathrm{Cn}^2}\cos\theta_0\left(1-\phi^2\right) \quad \text{on}\,\partial R\,.$$

4. The walls of the channel permit no flow of chemical potential

$$\nabla\mu\cdot\hat{n} = 0 \quad \text{on}\,\partial R\,.$$

The boundary condition imposing the contact angle is known as the Cahn Wetting Boundary Condition. This, like the nonlinear term in the chemical potential expression, must be treated with our operator splitting approach. The corresponding splitting scheme gives:

$$\nabla\phi\cdot\hat{n} = -\frac{\sqrt{2}}{2\mathrm{Cn}^2}\cos\theta_0\left(1-\phi^n\phi^{n+1}\right) \quad \text{on}\,\partial R\,.$$

Numerical Solver

The set of equations were solved using the FreeFem++ software package, an open-source Finite Element solver [90]. FreeFem provides a convenient interface in both Python and C++, removing the need to implement the actual machinery of finite-element solvers manually, it interfaces with open-source solver libraries including Petsc, and can be used in parallel environments with some work.

Convergence was measured by computing the interface width and interfacial energy during the initial nucleation and coarsening phase, the mesh adaptation eagerness and time-step adaptation parameters in the algorithm were adjusted to ensure reliable results.

3.4 Computational Results

In order to simulate the physical situation of interest we start our simulation with a non-uniform mixture of both phases, this will lead to the process of nucleation and ripening as discussed in the introduction to this chapter. A simple way to achieve this was to set the phase field to a slightly perturbed state corresponding to a quenched fluid where the temperature is slightly below the critical point ($T < T_c$). Gaussian noise was generated and used to set ϕ throughout the domain with mean μ and small variance σ.

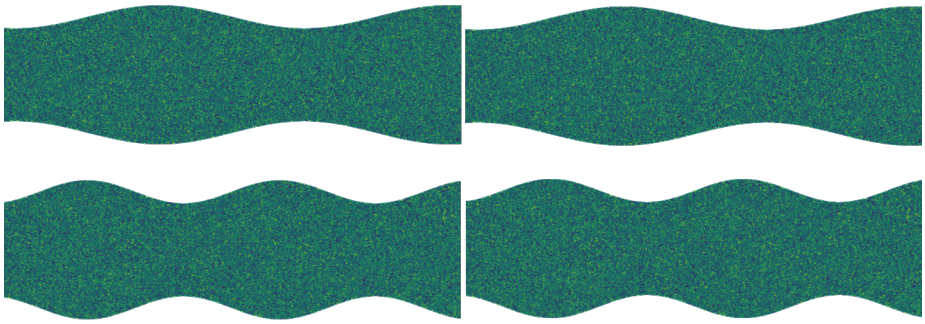

Figure 3.11: Example initial ϕ fields for two different channel geometries, colouring exaggerated, field chosen to be a Gaussian distribution: $\mathcal{N}(-0.1, 0.2)$

The equations were then solved for the initial evolution of the fluids; in all cases, initial nucleation to small droplets of each phase was observed. Coarsening then occured, whereby small droplets coalesce to form larger droplets that have lower interfacial energy. Eventually the rate of dissipation decreased and the fluid attained a steady-state: at this point, a body force was applied to the fluid and flow was generated.

We carried out a qualitative analysis of the long-time states in this driven system, observing the different flow morphologies and attempted to rationalise these with energy and flow field arguments.

3.4.1 Initial nucleation process

In order to simulate quenching of a fluid to below its critical point we set the initial phase field to a normally distributed random value. For our simulations we set the mean to be equal to zero, corresponding to no preference for one phase over the other, and we set the noise intensity, controlled by the standard deviation, to a small value (0.2).

Several sets of intial conditions are shown below in Figure 3.11. Here, green corresponds to $\phi = 0$, but we exaggerate the colouring for clarity; it is clear that the phase is perturbed, and we predict that areas where one colour predominates (yellow or blue) will lead to local droplets in the early stages of nucleation.

Shown below (Figure 3.12)is the progress of nucleation and coarsening for one set of initial conditions. The first stage involves the slightly perturbed phase relaxing to ± 1, and small droplets form of both phases in a predominantly mixed fluid (panels a-b). These droplets then grow as the bulk fluid relaxes into one phase or the other; the interfaces attain their natural width, but the droplets are still on the same length scale as the interfaces (panel c).

As the fluid continues to evolve, smaller droplets shrink by diffusion and disappear, narrow filaments of fluid separate, and large bulk areas grow. The length scale describing the droplets and slugs is now larger than the interface length scale (panels d-e). As the fluid continues to evolve, large droplets are

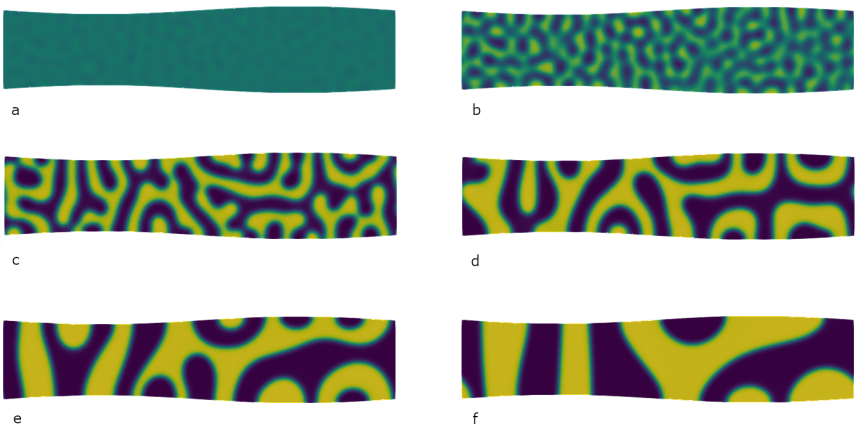

Figure 3.12: Example of nucleation and coarsening process for $\varepsilon = 0.1$, $\phi = 1$ in yellow, $\phi = -1$ in blue. Panels a-f show the same channel for $t = 0.002$, 0.005, 0.015, 0.04, 0.1, 0.3

left, together with slugs, and the interfacial energy of the system continues to relax towards equilibrium.

3.4.2 Effect of Flow Geometry

From our static analysis we predict that the shape of the channel will influence the flow morphology. We expect that strongly corrugated channels will prefer slug flow, and once the interfacial energy barrier to flow grows large enough we predict that pinning will occur, trapping a slug in the widest part of the channel.

For large corrugations this pinning was observed: in Figure 3.13, the fluid has formed a single slug which is pinned in the widest portion of the channel. The energy barrier to overcome is too large for the current forcing and the slug has stopped. In this case the fluid continues to flow, for the diffusive flux through the boundary is nonzero, which corresponds to fluid changing phase at the boundary.

The most commonly observed state was slug flow: for contact angles not equal to 90 deg one slug was observed, which was convected along the channel at varying speed, and since mass is conserved in this system the droplet length varied as in the static energy analysis. The size of the contact angle controls which phase appears to be the bulk and which the slug; the convention adopted is that the contact angle refers to the yellow phase ($\phi > 0$).

We also observed different variants of stratified flow which we did not expect to be stable. Below are two examples, where there are three strata (the minimal case), and where there are five strata, where the interfacial energy is even

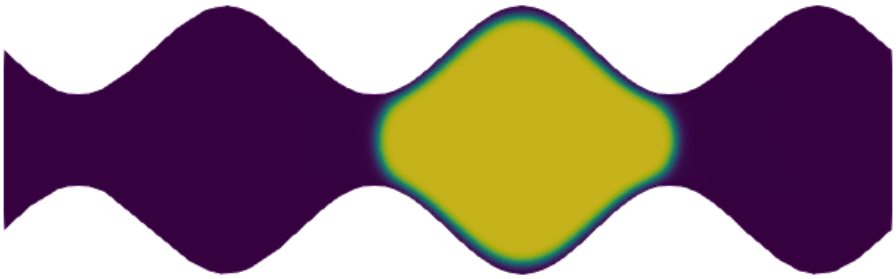

Figure 3.13:]
Large corrugations pin slugs at regions where the interfacial energy is minimised, shown for $\varepsilon = 0.6$, $\theta_0 = 140\,\text{deg}$.

Figure 3.14: Smaller corrugations allow slug flow, the left shows $\theta_0 = 140\,\text{deg}$, with the yellow phase appearing to be a slug in blue bulk ($\varepsilon = 0.2$), the right shows $\theta_0 = 40\,\text{deg}$, the blue phase as a slug in bulk yellow phase ($\varepsilon = 0.1$).

greater. We suggest that this is due to the velocity gradient within the channel causing shear, damping disturbances from this state. Here the fluid closest to the wall is controlled by the contact angle, yellow when $\theta_0 > 90\,\text{deg}$ and blue when $\theta_0 < 90\,\text{deg}$. Further study is needed to investigate the mechanism by which the flow stabilises the strata.

3.4.3 Effect of Contact Angle

When the contact angle produces exactly neutral wetting we observe a different picture. Smaller droplets no longer shrink when in contact with the wall, and a more complex picture emerges. As neither phase spreads when in contact with the wall, the forces which cause droplet coalescence are only the velocity gradient and the free energy interface width minimisation. For comparison see Figure 3.16; in the same geometry from the same intial conditions we observe that a thin layer of fluid forms immediately at the wall when the contact angle promotes spreading (panel a ii), this leads to filaments forming in the direction of the flow (panel a iv). When the contact angle is 90 deg this boundary layer does not form (panel b ii), and so there is less structure in the filament formation (panel b iii). This leads to a more complex fluid structure during the coarsening

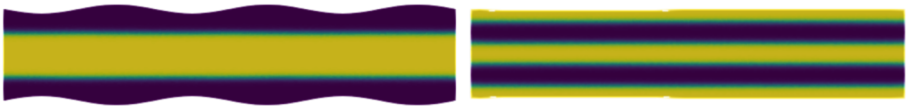

Figure 3.15: Two examples of stratified flow, left $\varepsilon = 0.1$, $k = 5\pi$ shows a yellow stratum between two blue strata, $\theta_0 = 70\,\text{deg}$, right $\varepsilon = 0.01$, $k = \frac{\pi}{5}$ shows a yellow stratum surrounded by blue strata and yellow strata, $\theta_0 = 110\,\text{deg}$.

(panel b iv), and it also makes multiple slugs much more likely (panel b v).

3.4.4 Effect of Initial Conditions

We hope that the flow morphology is affected more strongly by the geometry of the channel and the contact angle than by the initial conditions, as these parameters can be controlled in the simulations and in reality. Unfortunately, comparing the exact same parameter values for different initial conditions shows that this is not the case: the final flow morphology is strongly affected by the initial conditions (Figure 3.17).

In order to quantify the effect of the flow geometry and the contact angle on the final flow morphology, and in order to extract meaningful statistics from it, we need to compute the likely states. This involves computing the final state for a large number of initial conditions and determining likelihood of each state. This unfortunately proved impossible in the scope of this thesis, but provides an excellent opportunity for further work.

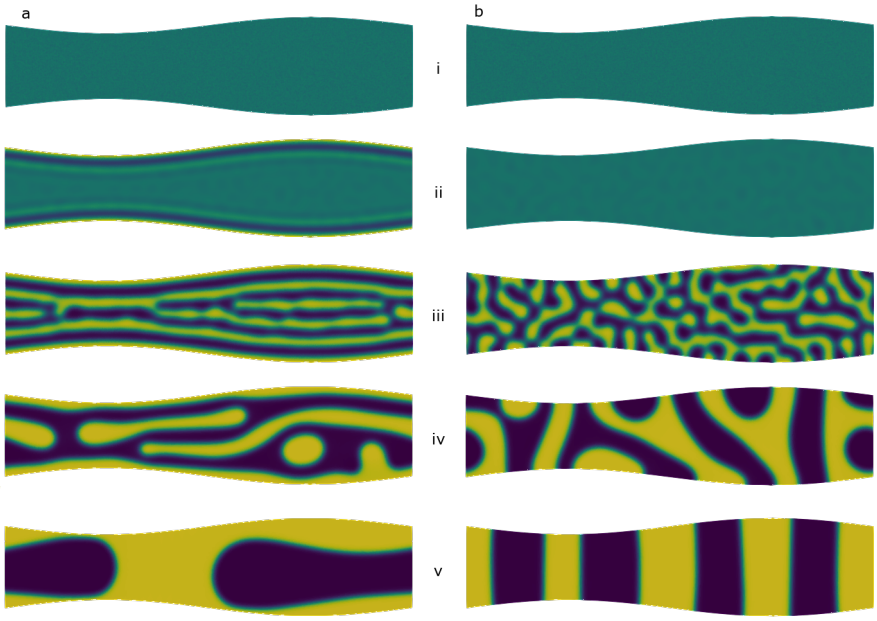

Figure 3.16: Identical channel geometries and initial conditions show marked differences in flow morphology when $\theta_0 = 90\,\text{deg}$ vs when $\theta_0 = 45\,\text{deg}$. Initial nucleation is slower (panels i, ii), no boundary layer is observed (panel iii), coarsening is less structured (panel iv), and multiple slugs are observed.

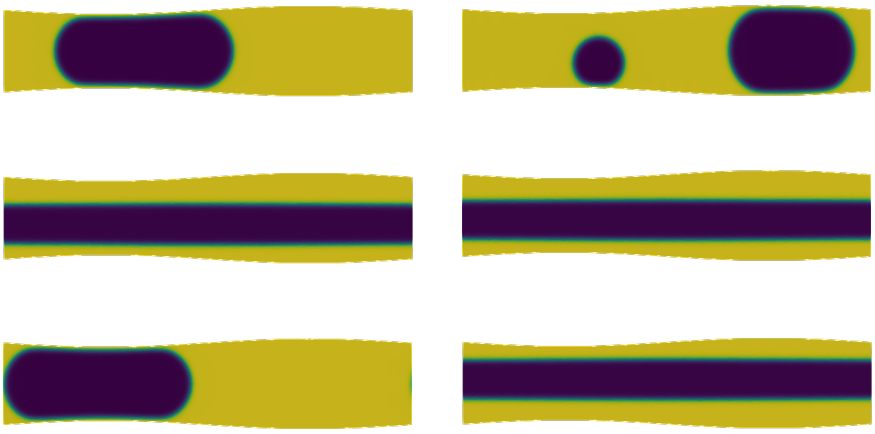

Figure 3.17: Final flow morphologies for different initial conditions, some led to stratified flow, some to slug flow, one to droplet and slug flow. $\theta_0 = 70\,\text{deg}$, $\varepsilon = 0.2$.

3.5 Conclusions and Future Work

Multi-phase flow in complex geometries is an area of research that looks to provide valuable insights into physical systems from science and engineering. Currently these flows are most commonly studied with the Volume of Fluid method in commercial CFD codes; these tend to be robust, but are computationally expensive. Phase-field models offer an attractive way to reduce the computational complexity of these types of systems, and offer a more rigorously based approach to treat the contact line.

We used a static analysis of droplet shapes to suggest likely configurations for two-phase fluids in different channel geometries, and concluded that, in general, fluids are likely to form slugs. This provided an initial idea of the parameter space that we could use to inform our numerical simulations. We also determined that the contact line motion is likely to be complex; static analysis suggests that hysteresis behaviour is expected in places, and that the motion is likely to be discontinuous. We determined the critical value for which this behaviour is to be expected analytically and confirmed it with numerical continuation, observing a cusp bifurcation.

We implemented the Cahn–Hilliard-Navier–Stokes equations in FreeFem++, obtaining a qualitative picture of the fluid flow. Whilst we were able to reproduce the flow morphologies we expected, we were unable to confirm how well the static energy analysis described the system. The final flow morphology was found to depend strongly on the random initial conditions. We propose that statistical analysis of many runs would be likely to reproduce the static analysis, but this was unfeasible within the limitations of this work.

This work offers many avenues for further study, work is needed to determine the magnitude of the effect that the initial conditions have on the final flow morphology. In order to confirm that the geometry has the effect of selecting one morphology over another it is necessary to compare the results of many simulation runs with different initial conditions, this will likely require the extension of the finite-element code to be fully parallel, as well as further computational resources. It will likely also require an automated method of flow characterisation in order to categorise the simulation results. Since the energy does not offer an unambiguous means of distinguishing between flow morphologies one would need to determine whether the interface was at the wall, and also measure the number of contiguous regions of each phase.

Another promising extension is to compare the predicted energy barrier from static analysis with the strength of the forcing introduced in the simulations, the authors predict that pinning is related to the magnitude of these two elements, but no direct link was found within the scope of this study. The analysis also assumes that only one droplet is likely, which is not justified, and the analysis could be extended to include multiple droplets. This would result in a whole family of possible solutions, and the phase portrait would be correspondinglt more complex.

The static analysis could also be extended to include systems where the two walls are not precisely out of phase, this would enable channels with different

wavelengths, and those where snaking occurs to be treated, potentially this could allow preferential selection of droplet sizes.

4

Transport in Porous Media

Porous media provide many physically interesting problems that we would wish to analyse, but difficulties in exactly treating flows in these kind of geometries are formidable. When introducing multiple phases we not only have the usual problems with contact-line stress to deal with, but we also have topological changes in the boundary and interface to treat.

Application of Cahn–Hilliard type equations to these kind of porous flow problems are attractive, not only do we gain the benefits mentioned, but we can make use of average representations of the medium to inform our fluid modelling. A classic approach to inform macroscopic flows in these media is to create a representative pore geometry which we imagine to be tiled repeatedly across the domain. We choose a classical representative pore (Figure 4.1) for our study, the kinked channel, but we note that other pores could be used.

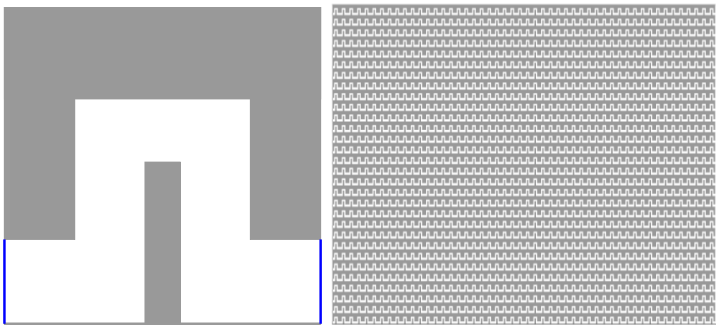

Figure 4.1: Multiscale view of a porous medium: A microscopic single pore through which fluid flow is simulated (Left); The macroscale channel geometry showing many repeated pores throughout the domain (Right)

4.1 Thermodynamic Derivation of the Convective Cahn–Hilliard Equations

In Chapter 3 we derived the Cahn–Hilliard equations using a microscopic and macroscopic force balance approach, this directly allowed us to motivate the coupling to the Navier–Stokes equations. In this chapter we recognise that flow is on a microscopic length scale and will be upscaled, we therefore present the original derivation as it highlights the thermodynamic basis for the model [29].

Cahn begins by observing that the free energy of some molecule in a non-uniform system will depend on both the local composition and the composition of the immediate vicinity. Assuming that the free energy (f) is continuous, it can be expanded with a Taylor series about the free energy of a molecule in a uniform solution (f_0) to obtain, to leading order:

$$f\left(c_i, \nabla c_i, \nabla^2 c_i\right) = f_0\left(c\right) + \sum_i L_i \frac{\partial c}{\partial x_i} + \sum_{ij} \kappa_{ij}^{(1)} \frac{\partial^2 c}{\partial x_i \partial x_j} + \frac{1}{2} \sum_{ij} \kappa_{ij}^{(2)} \left[\frac{\partial c}{\partial x_i} \frac{\partial c}{\partial x_j}\right] + \cdots , \tag{4.1}$$

where

$$L_i = \left[\frac{\partial f}{\partial \frac{\partial c}{\partial x_i}}\right]_0 , \tag{4.2}$$

$$\kappa_{ij}^{(1)} = \left[\frac{\partial f}{\partial \frac{\partial^2 c}{\partial x_i \partial x_j}}\right]_0 , \tag{4.3}$$

$$\kappa_{ij}^{(2)} = \left[\frac{\partial^2 f}{\partial \frac{\partial c}{\partial x_i} \partial \frac{\partial c}{\partial x_j}}\right]_0 . \tag{4.4}$$

In the original framework, where solid phases were considered, the tensors κ_{ij} reflect the crystal symmetry and L_i is the polarisation vector for a polar crystal. Using symmetry arguments for a cubic crystal (which are identical to assuming that the system is an isotropic liquid medium), most of the components of the tensors κ_1, κ_2 are zero, Equation 4.1 simplifies to:

$$f\left(c, \nabla c, \nabla^2 c\right) = f_0\left(c\right) + \kappa_1 \nabla^2 c + \kappa_2 \left(\nabla c\right)^2 + \cdots . \tag{4.5}$$

Integrating over some volume V gives the free energy of the volume F:

$$F = N_V \int_V \left[f_0\left(c\right) + \kappa_1 \nabla^2 c + \kappa_2 \left(\nabla c\right)^2\right] \, dV . \tag{4.6}$$

Applying the divergence theorem to Equation (4.6) yields

$$\int_V \left(\kappa_1 \nabla^2 c\right) \, \mathrm{d}V = -\int_V \left(\frac{d\kappa_1}{dc}\right) \left(\nabla c\right)^2 \, \mathrm{d}V + \int_S \left(\kappa_1 \nabla c \cdot \hat{\mathbf{n}}\right) \, \mathrm{d}S , \tag{4.7}$$

since we are interested in the behaviour of the bulk, not the edge effects, we can choose a boundary of integration such that the surface integral term vanishes.

This allows us to eliminate the $\nabla^2 c$ term from Equation (4.6). This yields an expression for the Free Energy of a system with two contributions, one representing the free energy of this volume in homogenous solution and a gradient energy term that is a function of the neighbourhood.

$$F = N_V \int_V \left[f_0 + \kappa \left(\nabla c \right)^2 \right] , \tag{4.8}$$

where

$$\begin{aligned} \kappa &= -\frac{d\kappa_1}{dc} + \kappa_2 \, , \\ &= -\left[\frac{\partial^2 f}{\partial c \partial \nabla^2 c} \right]_0 + \left[\frac{\partial^2 f}{\partial |\nabla c|^2} \right]_0 . \end{aligned} \tag{4.9}$$

The chemical potential is then introduced as the variational derivative of the free-energy. The flux of one component in the system can then be computed, permitting the use of a continuity equation. This is the classical Cahn–Hilliard equation.

$$\mu = \frac{\delta F}{\delta c} = F' \left(c \right) - \kappa \Delta c \, , \tag{4.10}$$

$$\frac{\partial c}{\partial t} = -\nabla \cdot \left(-M \nabla \mu \right) = \nabla \cdot \left(M \nabla \left(F' \left(c \right) - \kappa \Delta c \right) \right) . \tag{4.11}$$

The choice of function to model the free energy is an important one. Physically, the function should have one minimum for $T > T_c$ and two minima for $T < T_c$. Thermodynamic arguments lead to Equation (4.12) [125], but most authors replace this with a polynomial representation that is much simpler to treat Equation (4.13), this is usually fitted to the logarithmic form at a given temperature using the parameter α which can be interpreted as a reduced temperature.

$$\Delta F_{mix} \left(T, c \right) = \Omega c \left(1 - c \right) + RT \left[\left(1 - c \right) \ln \left(1 - c \right) + c \ln c \right] , \tag{4.12}$$

where R is the ideal gas constant, Ω and T are proportional to the critical temperature and the system temperature respectively.

$$\Delta F_{mix} \left(\beta, \alpha, c \right) = \frac{1}{4} \beta \left(c^2 + \alpha \right)^2 , \tag{4.13}$$

where β scales the magnitude of the free-energy and α is proportional to $T - T_c$.

In most physical systems the case of $\alpha < 0$ is relevant. This induces two minima at $c = \frac{-1}{\sqrt{-\alpha}}$ and $c = \frac{1}{\sqrt{-\alpha}}$ and corresponds to a system below the critical temperature, without loss of generality we assume that this is the case and set $\alpha = -1$. Henceforth we refer to the quantity ΔF_{mix} from equation 4.13 as F' as is convention in the literature.

Equation (4.11) is in dimensional form, in order to non-dimensionlise this we

use a result from Van der Waals [157] in [37] that the stationary solutions have constant chemical potential with a phase-field profile

$$\hat{c} = \tanh \frac{x}{\sqrt{2\xi}}\,. \tag{4.14}$$

The parameter ξ controls the width of the interface, with the form of the free potential defined in Equation 4.13 this is identified as $\xi = \sqrt{\frac{\kappa}{\beta}}$. This allows us to compute the equilibrium surface tension, it is given by

$$\sigma = \alpha \int_{-\infty}^{\infty} \left(\frac{d\hat{c}}{dx}\right)^2 dx = \frac{2\sqrt{2}}{3}\sqrt{\alpha\kappa}\,. \tag{4.15}$$

We now define non-dimensional variables:

$$\bar{\mathbf{x}} = \frac{1}{L}\mathbf{L}\,, \qquad \bar{\mathbf{u}} = \frac{1}{U}\mathbf{u}\,, \qquad \bar{t} = \frac{U}{L}t$$

Making use of the surface tension and interface width we determine that:

$$\beta = \frac{3\sigma}{2\sqrt{2}\xi} s,\,.$$

Rescaling Equation 4.11 and factoring β out of the potential we have:

$$\frac{\partial c}{\partial t} = \frac{3M\sigma}{2\sqrt{2}LU\xi}\nabla\cdot\left(\nabla\left(F'\left(c\right) - \frac{\xi^2}{L^2}\Delta c\right)\right)\,. \tag{4.16}$$

We then can identify two dimensionless groups:

$$\frac{\xi}{L} = \mathrm{Cn}, \qquad \frac{2\sqrt{2}UL\xi}{3M\sigma} = \mathrm{Pe}\,,$$

the Cahn number (Cn) controls the width of the interface relative to the characteristic length of the geometry, the Péclet number (Pe) controls the relative importance of convective and diffusive flux.

The non-dimensionlised form of the Cahn–Hilliard equation is therefore given (dropping the overbars) by:

$$\frac{\partial c}{\partial t} = \frac{1}{\mathrm{Pe}}\Delta\left(F'\left(c\right) - \mathrm{Cn}^2\Delta c\right) \tag{4.17}$$

or equivalently, as the following two equations:

$$\frac{\partial \phi}{\partial t} = \frac{1}{\mathrm{Pe}}\Delta\left(\mu\right)\,, \tag{4.18}$$

$$\mu - F'\left(\phi\right) + \mathrm{Cn}^2\Delta\phi = 0\,. \tag{4.19}$$

In the above we replace the concentration c with the more conventional order parameter ϕ (this can represent density and concentration interchangeably under our assumptions).

4.2 Upscaling in Porous Media

Within a porous medium we observe that there is a large resistance to flow, therefore the macroscopic Reynolds number of the flow is likely to be low. We can therefore model the flow at the microscale using the Stokes equations coupled with the Cahn–Hilliard equations from Section 4.1 at the macroscale. We consider a model system with a separation of scales, we admit a periodic microstructure in a macroscopic flow channel.

Much in the way that Darcy's law models flow as a pressure overcoming a constant resistance caused by the medium, we seek to quantify the medium's effect on flow. By solving Stokes' equation and then using the machinery of homogenization we seek to use a more complex model for our medium that can model anisotropy and flow-dependent effects without directly simulating the entire flow field.

This model (porous Cahn–Hilliard with Stokes' Flow or pCHS) consists of Stokes' equation, the incompressibility criterion and the Cahn–Hilliard equations from before. The velocity is coupled to the phase-field ϕ through a convection term in the Cahn–Hilliard equation. As a result of our assumption that the Reynolds' number is low we model the effect of phase on the velocity through a driving force term in the Stokes' equation. The equations read:

$$\begin{aligned} \frac{\partial \phi}{\partial t} + \mathrm{Pe}\left(\mathbf{u}\cdot\nabla\right)\phi &= \lambda\nabla\cdot\left(\mu\right)\,, \\ \mu - F'\left(\phi\right) + \mathrm{Cn}^2\Delta\phi &= 0\,, \\ \nabla\cdot\mathbf{u} &= 0\,, \\ -\eta\Delta\mathbf{u} + \nabla p &= \eta\left(\phi\right)\,. \end{aligned} \tag{4.20}$$

The driving force for the flow is a function of the elastic energy in the system, which models the effect of phase on the velocity. This is formally:

$$\eta = \gamma\nabla\cdot\left(\nabla\phi\otimes\nabla\phi\right)\,,$$

which, for simplicity, and to a reasonable physical approximation we can set to 1 in the principal direction of the flow: $\hat{\mathbf{i}}$.

Identifying a scale separation parameter $\varepsilon = \frac{l}{L}$ as the ratio of the microscopic cell size l to the macroscopic channel width L, we can rewrite the equations in their microscopic form (for the flow through the periodic microstructure). In order to derive an effective expression for flow we take the stationary version of the equations:

$$\begin{aligned} \mathrm{Pe}\left(\mathbf{u}_\varepsilon\cdot\nabla\right)\phi &= \lambda\nabla\cdot\left(\nabla\mu\right)\,, \\ \mu - F'\left(\phi_\varepsilon\right) + \mathrm{Cn}^2\Delta\phi_\varepsilon &= 0\,, \\ \nabla\cdot\mathbf{u}_\varepsilon &= 0\,, \\ -\varepsilon^2\mu\Delta\mathbf{u}_\varepsilon + \nabla p_\varepsilon &= \hat{\mathbf{i}}\,. \end{aligned} \tag{4.21}$$

Following the process from [160], we begin by expanding the Laplace operators Δ and $\nabla \cdot (M\nabla)$ into powers of ε, taking the first two terms in the expansion:

$$\begin{aligned} \Delta u_\varepsilon &= \varepsilon^{-2}\mathcal{A}_0(u) + \varepsilon^{-1}\mathcal{A}_1(u) + \mathcal{A}_2(u) , \\ \nabla \cdot (Mu_\varepsilon) &= \varepsilon^{-2}\mathcal{B}_0(u) + \varepsilon^{-1}\mathcal{B}_1(u) + \mathcal{B}_2(u) , \end{aligned} \tag{4.22}$$

where the terms are given below. We take the interface to be a moving frame, so the velocity $\mathbf{u}^\varepsilon$ is defined as $\mathbf{u}\left(x - \frac{v}{\varepsilon}, y, t\right)$

$$\begin{aligned} \mathcal{A}_0 &= -\sum_{i,j=1}^{d} \frac{\partial}{\partial y_i}\left(\delta_{ij}\frac{\partial}{\partial y_j}\right) , \\ \mathcal{A}_1 &= -\sum_{i,j=1}^{d}\left[\frac{\partial}{\partial x_i}\left(\delta_{ij}\frac{\partial}{\partial y_j}\right) + \frac{\partial}{\partial y_i}\left(\delta_{ij}\frac{\partial}{\partial x_j}\right)\right] , \\ \mathcal{A}_2 &= -\sum_{i,j=1}^{d} \frac{\partial}{\partial x_j}\left(\delta_{ij}\frac{\partial}{\partial x_j}\right) , \end{aligned} \tag{4.23}$$

$$\begin{aligned} \mathcal{B}_0 &= -\sum_{i,j=1}^{m} \frac{\partial}{\partial y_i}\left(\delta_{ij}\frac{\partial}{\partial y_j}\right) , \\ \mathcal{B}_1 &= -\sum_{i,j=1}^{m}\left[\frac{\partial}{\partial x_i}\left(\delta_{ij}\frac{\partial}{\partial y_j}\right) + \frac{\partial}{\partial y_i}\left(\delta_{ij}\frac{\partial}{\partial x_j}\right)\right] , \\ \mathcal{B}_2 &= -\sum_{i,j=1}^{m} \frac{\partial}{\partial x_j}\left(\delta_{ij}\frac{\partial}{\partial x_j}\right) , \end{aligned} \tag{4.24}$$

we also obtain the following equation for the flow velocity as a result of the above change of reference frame:

$$\frac{\partial}{\partial t}\mathbf{u}^\varepsilon = \left(\frac{\partial}{\partial t} - \frac{v \cdot \nabla_x}{\varepsilon}\right)\mathbf{u}^\varepsilon . \tag{4.25}$$

Carrying out a conventional expansion of the variables in powers of ε:

$$\begin{aligned} w^\varepsilon &= w_0 + \varepsilon w_1(x,y,t) + \varepsilon^2 w_2(x,y,t) + \cdots , \\ \phi^\varepsilon &= \phi_0 + \varepsilon\phi_1(x,y,t) + \varepsilon^2\phi_2(x,y,t) + \cdots . \end{aligned} \tag{4.26}$$

The non-linear form of the homogenous free energy admits a natural Taylor expansion in ε:

$$f(\phi^\varepsilon) = f(\phi_0) + f'(\phi_0)(\phi^\varepsilon - \phi_0) + \frac{1}{2}f''(\phi_0)(\phi^\varepsilon - \phi_0)^2 + \mathcal{O}\left((\phi^\varepsilon - \phi_0)^3\right) . \tag{4.27}$$

Substituting the expressions from Equation (4.26) into Equation (4.23) and (4.24) and collecting terms in like powers of ε we obtain three sets of equations. Considering them in order they read:

$$\begin{aligned}
\lambda\mathcal{B}_0\left[w_0 + f\left(\phi_0\right)\right] + \mathrm{Pe}_{\mathrm{mic}}\left(\mathbf{u}\cdot\nabla_y\right)\mathcal{A}_2^{-1}w_0 &= 0 \\
w_0 \quad &\text{periodic} \\
\mathcal{A}_0 w_0 &= 0 \\
w_0, \phi_0 \quad &\text{are periodic} \\
\nabla_n\phi_0 &= 0 \quad \text{on the boundary} \\
&\text{no} - \text{flux on boundary}
\end{aligned} \tag{4.28}$$

This requires that the leading order terms are independent of the micro-scale y, the second set of equations gives the reference cell problem for ϕ_0, once we identify $\phi_1 = -\sum_{k=1}^{d}\xi_\phi^k\left(y\right)\left(\dfrac{\partial\phi_0}{\partial x_k}\right)$:

$$\begin{aligned}
\lambda\mathcal{B}_0\left[w_1 + f'\left(\phi_0\right)\phi_1\right] + \mathrm{Pe}_{\mathrm{mic}}\left(\mathbf{u}\cdot\nabla_y\right)\mathcal{A}_2^{-1}w_1 = \\
-\lambda\mathcal{B}_1\left[w_0 + f\left(\phi_0\right)\right] - \mathrm{Pe}_{\mathrm{mic}}\left(\left(\mathbf{u}-\mathbf{v}\right)\cdot\nabla\right)\mathcal{A}_2^{-1}w_0 \\
\mathcal{A}_0\phi_1 = -\mathcal{A}_1\phi_0 \\
w_1, \phi_1 \quad \text{are periodic} \\
\nabla_n\phi_1 = 0 \quad \text{on the boundary} \\
\text{no} - \text{flux on boundary}
\end{aligned} \tag{4.29}$$

$$\begin{aligned}
-\sum_{i,j=1}^{d}\frac{\partial}{\partial y_i}\left(\delta_{ik} - \delta_{ij}\frac{\partial\xi_\phi^k}{\partial y_j}\right) = -\nabla\cdot\left(\mathbf{e}_k - \nabla_y\xi_\phi^k\right) = 0 \\
\mathbf{n}\cdot\left(\nabla\xi_\phi^k + \mathbf{e}_k\right) = 0 \\
\xi_\phi^k\left(y\right) \quad \text{is periodic} \\
\mathcal{M}_{Y^1}\left(\xi_\phi^k\right) = 0
\end{aligned} \tag{4.30}$$

It also yields the cell problem for w_1, this depends on both the corrector field ξ_ϕ^k from Equation 4.30 and the fluid velocity $\mathbf{u}$. Under the assumption of a scale separated potential (assuming that the potential has a non-zero derivative in only the macroscopic scale), we obtain:

$$-\sum_{i,j,k=1}^{d}\frac{\partial}{\partial y_i}\left(\delta_{ik}-\delta_{ij}\frac{\partial\xi_\phi^k}{\partial y_j}\right)f'(\phi_0)=\lambda\sum_{k,i,j=1}^{d}\frac{\partial}{\partial y_i}\left(\mathrm{m}_{ik}-\mathrm{m}_{\mathrm{ij}}\frac{\partial\xi_\phi^k}{\partial y_j}\right)f'(\phi_0)$$
$$-\mathrm{Pe}_{\mathrm{mic}}\sum_{i=1}^{d}\left(\mathbf{u}^i-\mathbf{v}^i\right) \tag{4.31}$$

$$\sum_{i,j,k=1}^{d}\mathbf{n}_i\left(\delta_{ij}\frac{\partial\xi_w^k}{\partial y_j}-\delta_{ik}\right)-\lambda\sum_{k,i,j=0}^{d}\mathbf{n}_i\frac{\partial}{\partial y_i}\left(\mathrm{m}_{ik}-\mathrm{m}_{ij}\frac{\partial\xi_\phi^k}{\partial y_j}\right)=0 \tag{4.32}$$

$$\xi_w^k(y)\quad\text{is periodic} \tag{4.33}$$

$$\mathcal{M}_{Y^1}\left(\xi_w^k\right)=0 \tag{4.34}$$

This leads to the following expressions for ξ_w^k and $\mathbf{v}^i$:

$$\mathbf{v}^i=\frac{\mathrm{Pe}_{\mathrm{mic}}}{|Y^1|}\int_{Y^1}\mathbf{u}^j(y)\,dy \tag{4.35}$$

$$-\sum_{i,j,k=1}^{d}\frac{\partial}{\partial y_i}\left(\delta_{ik}-\delta_{ij}\frac{\partial\xi_w^k}{\partial y_j}\right)=\lambda\sum_{k,i,j=1}^{d}\frac{\partial}{\partial y_i}\left(\mathrm{m}_{ik}-\mathrm{m}_{ij}\frac{\partial\xi_\phi^k}{\partial y_j}\right)$$
$$\sum_{i,j,k=1}^{d}\mathbf{n}_i\left(\left(\delta_{ij}\frac{\partial\xi_w^k}{\partial y_j}-\delta_{ik}\right)-\lambda\sum_{k,i,j=1}^{d}\frac{\partial}{\partial y_i}\left(\mathrm{m}_{ik}-\mathrm{m}_{ij}\frac{\partial\xi_\phi^k}{\partial y_j}\right)\right)=0 \tag{4.36}$$
$$\xi_w^k(y)\quad\text{is periodic}$$
$$\mathcal{M}_{Y^1}\left(\xi_w^k\right)=0$$

The last of the problems for ϕ_2 is classical and after identifying the correction tensor $\hat{\mathrm{D}}$ where $\mathrm{d}_{ij}=\frac{1}{|Y|}\sum_{j=1}^{d}\int_{Y^1}\left(\delta_{ik}-\delta_{ij}\frac{\partial\xi_\phi^k}{\partial y_j}\right)dy$ gives the upscaled equation:

$$-\Delta_{\hat{D}}\phi_0=-\nabla\cdot\left(\hat{\mathrm{D}}\nabla\phi_0\right)=\rho w_0+\tilde{g}_0 \tag{4.37}$$

Applying the Fredholm alternative (also known as the solvability criterion) to the problem for w_2 and some manipulation we define two new tensors related to the mobility and one related to the flow which makes use of Equation (4.35):

$$\mathrm{m}_{ik}^w=\frac{1}{|Y|}\sum_{j=1}^{d}\left(\mathrm{m}_{ik}-\mathrm{m}_{ij}\frac{\partial\xi_w^k}{\partial y_j}\right)dy\,, \tag{4.38}$$

$$\mathrm{m}_{ik}^\phi=\frac{1}{|Y|}\sum_{j=1}^{d}\left(\mathrm{m}_{ik}-\mathrm{m}_{ij}\frac{\partial\xi_\phi^k}{\partial y_j}\right)dy\,, \tag{4.39}$$

$$\mathrm{c}_{ik} = \frac{\mathrm{Pe}_{\mathrm{mic}}}{|Y|} \int_{Y^1} \left(\mathbf{u}^i - \mathbf{v}^i\right) \delta_{ik} \xi_\phi^k \, dy \,, \tag{4.40}$$

where the components c_{ik} form the tensor $\hat{\mathrm{C}}$, the components m_{ik}^{ϕ} form the tensor $\hat{\mathrm{M}}_\phi$ and the components m_{ik}^{w} form the tensor $\hat{\mathrm{M}}_w$.

Making use of Equation 4.37 we obtain the final upscaled macroscopic phase field equation:

$$p\frac{\partial \phi_0}{\partial t} = \nabla \cdot \left(\left[\lambda \hat{\mathrm{M}}_\phi f'\left(\phi_0\right) + \hat{\mathrm{C}} \right] \nabla \phi_0 \right) - \frac{\lambda}{p} \nabla \cdot \left(\hat{\mathrm{M}}_w \nabla \left(\nabla \cdot \left(\hat{\mathrm{D}} \nabla \phi_0 \right) - \tilde{g}_0 \right) \right) \tag{4.41}$$

We observe that the upscaling process has the effect of modifying the original Convective Cahn–Hilliard equation (Equation (4.20)), adding tensors that reflect the microscopic flow. It does not change the actual nature of the equations, and so we can presume that the upscaled equations will still have physical relevance and a physical basis.

4.3 Numerical Method

The upscaling method effectively decouples the micro-scale form the macroscopic flow equations. The result is that we have several scalar fields and tensors to compute and we can then solve CHS on only the macroscopic domain. We begin by making assumptions about the fluid and the flow which will reduce the number of tensors we need to precompute to two: we assume that the mobility is isotropic and independent of the phase. This reduces the number of tensors to compute to two: $\hat{\mathrm{D}}$ and $\hat{\mathrm{C}}$. We also further assume that the mobility is equal to 1.

4.3.1 Cell Problem Solver

The cell problem for the tensor $\hat{\mathrm{D}}$ (Equation (4.30)) is a classic Poisson equation with Neumann boundary conditions. This is solved within the reference cell to obtain the diffusion tensor for that reference cell geometry.

$$\nabla^2 \xi_\phi^k = 0 \quad \text{in } \mathrm{Y}^1 \,, \tag{4.42}$$

$$\hat{n} \cdot \nabla \xi_\phi^k = n_k \quad \text{on } \partial \mathrm{Y}^1 \,. \tag{4.43}$$

The boundary condition links the normal to each wall segment $\hat{n}$ with the unit vector in the kth direction n_k.

In order to solve the cell problem using a finite-element method it must be rewritten in its weak form. This is done by multiplying each term by a test function π and integrating over the domain, obtaining an equivalent equation that can be satisfied by piecewise constructed functions.

$$\nabla^2 \xi_\phi^k = 0\,, \tag{4.44}$$

$$\nabla^2 \xi_\phi^k \pi = 0\,, \tag{4.45}$$

$$\int_{Y^1} \nabla^2 \xi_\phi^k \pi \,\mathrm{d}x = 0\,, \tag{4.46}$$

$$\int_{Y^1} \nabla \xi_\phi^k \cdot \nabla \pi \,\mathrm{d}x - \int_{\partial Y^1} \nabla \xi_\phi^k \cdot \hat{n} \pi \mathrm{d}s = 0\,. \tag{4.47}$$

The boundary conditions (Equation 4.43) are satisfied by choosing appropriate values for the surface integral term for each wall in the microscopic geometry.

The remaining constraint for solution is that the average value of the corrector field be equal to zero, and this is satisfied by ensuring that $\int_{Y^1} \xi_\phi^k \,\mathrm{d}x = 0$. The problem was then solved by the continuous Galerkin method using the open source finite element software FEniCS [5]. Convergence was tested by comparing the interface velocity and width for various coarsenesses of mesh.

4.3.2 Stokes' Problem for the Convection Tensor

The problem for the convection tensor $\hat{\mathrm{C}}$ (Equation (4.40)) requires the solution of a periodic Stokes' problem with constant forcing (Equation (4.21). We adopt the same approach, converting the equations into their weak form to enable solution using the finite element method.

We adopt test functions v, q corresponding to the velocity and the pressure respectively and carry out the same process as for the cell problem:

$$-\mu \nabla^2 u + \nabla p = \eta \tag{4.48}$$

$$-\mu \int_{Y^1} v \nabla^2 u \,\mathrm{d}x + \int_{Y^1} v \nabla p \,\mathrm{d}x = \int_{Y^1} \eta \cdot v \,\mathrm{d}x \tag{4.49}$$

$$\nabla \cdot u = 0 \tag{4.50}$$

$$\int_{Y^1} q \nabla \cdot u \,\mathrm{d}x = 0 \tag{4.51}$$

Since these equations must be true for any arbitrary domain we can add the equations together and use integration by parts to obtain:

$$-\mu \int_{Y^1} v \nabla^2 u \,\mathrm{d}x + \int_{Y^1} v \nabla p \,\mathrm{d}x + \int_{Y^1} q \nabla \cdot u \,\mathrm{d}x = \int_{Y^1} \eta \cdot v \,\mathrm{d}x\,, \tag{4.52}$$

$$-\mu \int_{Y^1} \nabla u \nabla v \,\mathrm{d}x + \int_{Y^1} v \nabla p \,\mathrm{d}x + \int_{Y^1} q \nabla \cdot u \,\mathrm{d}x = \int_{Y^1} \eta \cdot v \,\mathrm{d}x - \mu \int_{\partial Y^1} v \nabla u \,\mathrm{d}s\,. \tag{4.53}$$

Following the assumption also made by the authors in [160] and [161], we take the microscopic driving force to be constant and unaffected by the macroscopic phase field–we assume that the Korteweg stress tensor is constant.

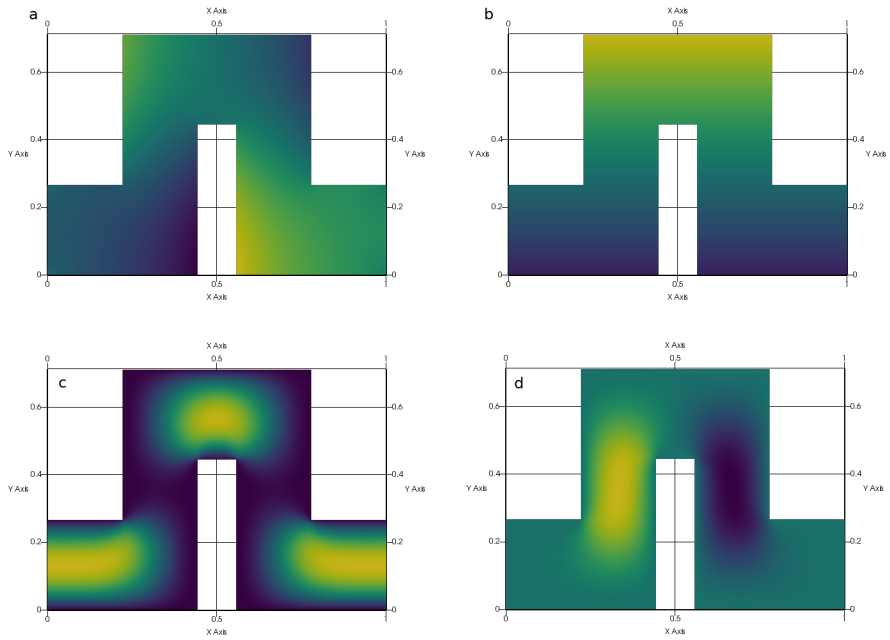

Figure 4.2: Kinked channel geometry: Panel a ξ^1 field, yellow = 0.32, blue = -0.32. b ξ^2 field, yellow = 0.41, blue = -0.4. c u_1. d) u_2.

The problem is closed by the boundary conditions, we assume that on the wall boundary we have a no slip and no flux condition, and the channel is periodic in the x direction:

$$\nabla u = 0 \quad \text{on}\, \partial Y^1\,, \tag{4.54}$$

$$u\,(1,\cdot) = u\,(0,\cdot)\ . \tag{4.55}$$

The former is neatly dealt with by dropping the last term in Equation (4.53), and the latter must be imposed in some way.

We solve Equation 4.53 in the same software–FEniCS [5], using a Continuous Galerkin method. Results for both the cell problem and the Stokes' problem are shown below for two different microscopic geometries - Figure (4.2) shows a classical kinked channel geometry, and Figure 4.3 shows an 'Inkbottle' geometry.

4.3.3 Macroscopic Problem

Once the values for the tensors $\hat{C}$ and $\hat{D}$ are computed we can solve the upscaled equation for the evolution of the phase field (4.41). We elected initially to use the same Finite-Element approach and package as for the cell and Stokes problem:

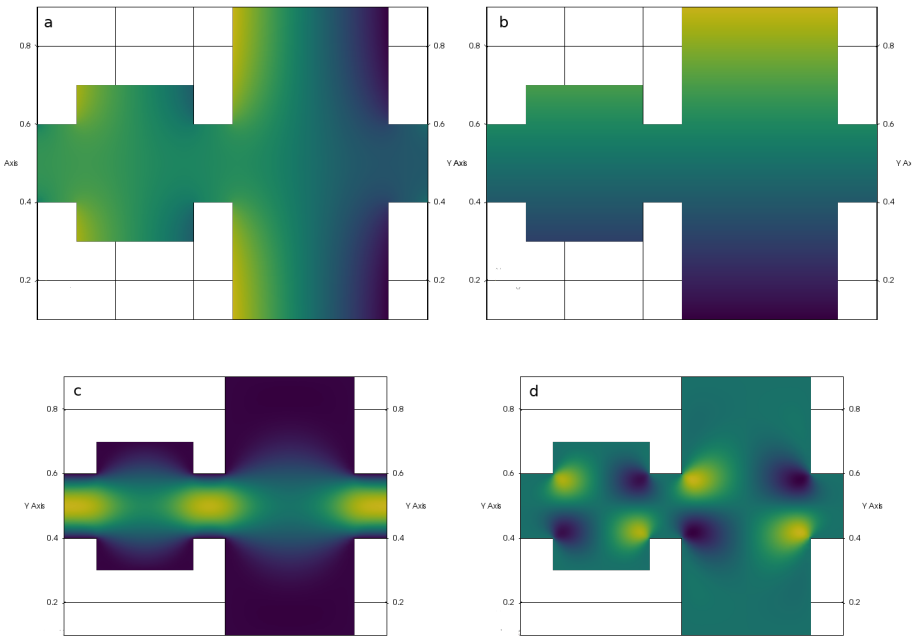

Figure 4.3: So-called 'Inkbottle' geometry: Panel a ξ^1 field, yellow = 0.15, blue = -0.21. b ξ^2 field, yellow = 0.4, blue = -0.4. c u_1. d) u_2.

$$p\frac{\partial \phi_0}{\partial t} = \nabla \cdot \left(\left[\lambda \hat{\mathrm{M}}_\phi f'\left(\phi_0\right) + \hat{\mathrm{C}} \right] \nabla \phi_0 \right) - \frac{\lambda}{p} \nabla \cdot \left(\hat{\mathrm{M}}_w \nabla \left(\nabla \cdot \left(\hat{\mathrm{D}} \nabla \phi_0 \right) - \tilde{g}_0 \right) \right) . \tag{4.56}$$

The time derivative will be dealt with later, we make initial rearrangements as a result of the constant values of $\hat{C}$ and $\hat{D}$, yielding the more classical formulation of the chemical potential and an evolution equation for the phase field:

$$p\frac{\partial \phi_0}{\partial t} = \nabla \cdot \hat{C} \nabla \phi_0 + \nabla \cdot \hat{M} \nabla \left(\mu \left(\phi_0 \right) \right) , \tag{4.57}$$

$$\mu = f'\left(\phi_0\right) - \frac{\lambda}{p} \nabla \cdot \hat{D} \nabla \phi_0 . \tag{4.58}$$

Introducing test functions as before, θ and ν corresponding to the phase (ϕ) and the chemical potential μ respectively:

$$p\int_Y \frac{\partial \phi_0}{\partial t}\theta \,\mathrm{d}x = \int_Y \nabla\cdot\hat{C}\nabla\phi_0\theta\,\mathrm{d}x + \int_Y \nabla\cdot\hat{M}\nabla\left(\mu\left(\phi_0\right)\right)\theta\,\mathrm{d}x\,, \tag{4.59}$$

$$\int_Y \mu\nu\,\mathrm{d}x = \int_Y f'\left(\phi_0\right)\nu\,\mathrm{d}x - \frac{\lambda}{p}\int_Y \nabla\cdot\hat{D}\nabla\phi_0\nu\,\mathrm{d}x \tag{4.60}$$

$$\begin{aligned} p\int_Y \frac{\partial \phi_0}{\partial t}\theta\,\mathrm{d}x =& \int_Y \hat{C}\nabla\phi_0\nabla\theta\,\mathrm{d}x + \int_Y \hat{M}\nabla\left(\mu\left(\phi_0\right)\right)\nabla\theta\,\mathrm{d}x\,, \\ &- \int_{\partial Y}\hat{C}\nabla\phi_0\theta\,\mathrm{d}s - \int_{\partial Y}\hat{M}\nabla\left(\mu\left(\phi_0\right)\right)\theta\,\mathrm{d}s \end{aligned} \tag{4.61}$$

$$\int_Y \mu\nu\,\mathrm{d}x = \int_Y f'\left(\phi_0\right)\nu\,\mathrm{d}x - \frac{\lambda}{p}\int_Y \hat{D}\nabla\phi_0\nabla\nu\,\mathrm{d}x + \frac{\lambda}{p}\int_{\partial Y}\hat{D}\nabla\phi_0\nu\,\mathrm{d}s\,. \tag{4.62}$$

The nonlinear term in the expression for the chemical potential (Equation (4.62)) presents numerical difficulties, if it is handled it its present form an iterative method must be used to solve the equation and this is computationally inefficient, it also presents severe constraints on the time and spatial resolution required [170].

In order to overcome this difficulty we adopt a splitting strategy called the OD2-BDF method, this separates the potential term into a convex and non-convex part, treating the former with the Optimal Dissipation second order scheme from [82] and the latter with a two-step backward difference method [83]. This offers a good balance of accuracy and speed, having a second order truncation error in time and second order numerical dissipation in time [170].

$$f'\left(\phi\right) = \phi\left(\phi^2 - 1\right) \tag{4.63}$$

$$= \frac{1}{2}\left(3\phi_{n-1}^2\phi_n - \phi_{n-1}^3\right) - \frac{1}{2}\left(3\phi_{n-1} - \phi_{n-2}\right)\,. \tag{4.64}$$

The time stepping was handled with the first-order Euler Method, this was chosen as to reduce the computational complexity and following most approaches taken in literature. This yields the final Finite-Element scheme:

$$\begin{aligned} \frac{p}{\Delta t}\int_Y \left(\phi_n - \phi_{n-1}\right)\theta\,\mathrm{d}x =& \int_Y \hat{C}\nabla\phi_n\nabla\theta\,\mathrm{d}x + \int_Y \hat{D}\nabla\left(\mu\left(\phi_n\right)\right)\nabla\theta\,\mathrm{d}x \\ &- \int_{\partial Y}\hat{C}\nabla\phi_n\theta\,\mathrm{d}s - \int_{\partial Y}\hat{D}\nabla\left(\mu\left(\phi_n\right)\right)\theta\,\mathrm{d}s\,, \end{aligned} \tag{4.65}$$

$$\begin{aligned} \int_Y \mu\nu\,\mathrm{d}x =& \int_Y \left(\frac{1}{2}\left(3\phi_{n-1}^2\phi_n - \phi_{n-1}^3\right) - \frac{1}{2}\left(3\phi_{n-1} - \phi_{n-2}\right)\right)\nu\,\mathrm{d}x \\ &- \frac{\lambda}{p}\int_Y \hat{D}\nabla\phi_n\nabla\nu\,\mathrm{d}x + \frac{\lambda}{p}\int_{\partial Y}\hat{D}\nabla\phi_n\nu\,\mathrm{d}s\,. \end{aligned} \tag{4.66}$$

4.3.4 Boundary Conditions

The boundary conditions for the upscaled equation that we choose to close the problem are:

1. No chemical potential flux through walls:

$$\nabla\mu \cdot \hat{n} = 0 \quad \text{on } \partial Y_w \,. \tag{4.67}$$

2. Fixed flux of chemical potential at the inlet and outlet corresponding to a pressure driven flow:

$$\nabla\mu \cdot \hat{n} = \hat{g} \quad \text{on } \partial Y_i \,. \tag{4.68}$$

3. Fixed value of phase at the inlet corresponding to purely phase A entering

$$\phi\,(0,\cdot) = \phi_i \quad \text{on } \partial Y_i \,, \tag{4.69}$$

$$\phi_i^3 - \phi_i - 1 = 0 \,. \tag{4.70}$$

4. Wetting boundary condition along wall [97]:

$$\nabla\phi \cdot \hat{n} = -\frac{3\sigma}{4}\left(1-\phi^2\right) \,. \tag{4.71}$$

In a similar way to the chemical potential term the wetting boundary condition must be split over time-steps, this can be carried out as follows [10]:

$$-\frac{3\sigma}{4}\left(1-\phi^2\right) = -\frac{3\sigma}{4}\left(1-\phi_n\phi_{n-1}\right) \tag{4.72}$$

4.4 Results

Computations were carried out using this Finite-Element formulation, results for the Stokes' problem and the cell problem are shown above.

In order to validate this Finite-Element formulation we seek to recover the results from the paper by Schmuck [160]. We take a channel with a neutral wetting and fixed inward flux and we begin with a periodically perturbed interface. Duncan et al. found that the interface would propagate along the channel, retaining the perturbation. This is in contrast to a plain Cahn–Hilliard model, where the perturbation would be smoothed out.

The authors of the previous study matched the macroscopic inlet conditions to the microscopic geometry by perforating the walls at the inlet and outlet. This enables us to change the relative size of the channel to the microscopic flow field.

We attempted to use the Finite-Element formulation derived above, but were unable to achieve convergence within the timescale of this project, and hence we are unable to present results from it. Instead we present initial simulations from

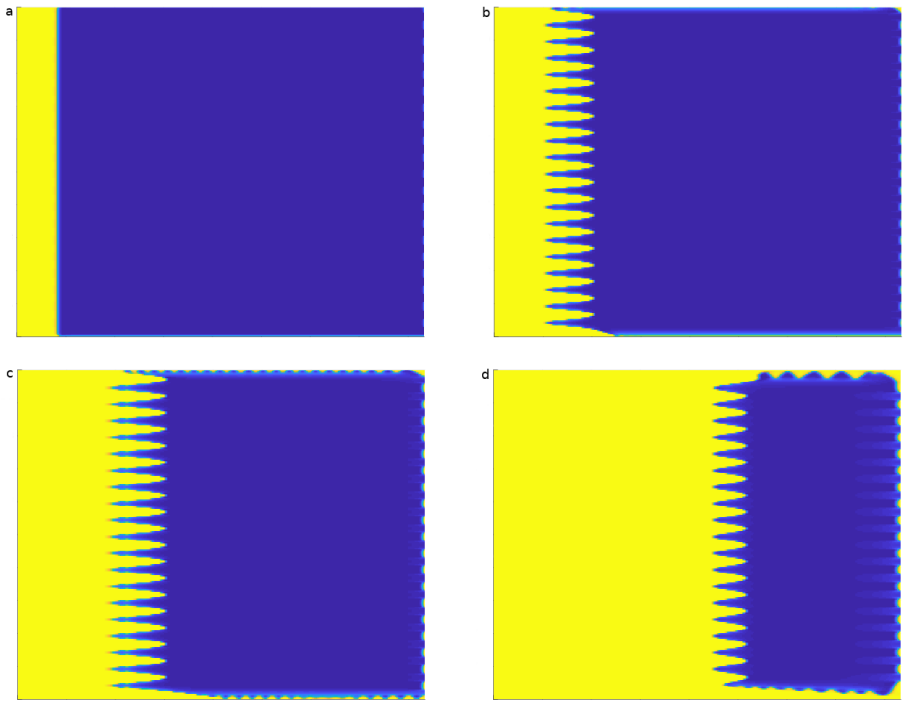

Figure 4.4: Evolution of an initially flat interface according to the Upscaled phase-field model, $\theta_0 = \frac{\pi}{2}$, Cn $= \frac{1}{240}$. Panels show phase-field over time: a) Initially $t = 0s$, b) After 10 timesteps $t = 100s$, c) after 20 steps $t = 200s$, d) after 50 steps $t = 500s$. Mesh is a regular rectangular mesh, with 400x240 elements

a Finite-Difference model of the same system [161]. We take the tensor values from that work, which compares well with experimental work by Auriault et al. [9] ($D_{11} = 0.4$, $D_{22} = 0$ and $C_{11} = 0.023$, $C_{22} = 0.015$, all off-diagonal elements are zero).

An initially straight interface is allowed to evolve under the influence of a pressure difference and we observe its motion in a channel:

The interface rapidly develops fronts in line with the inlet locations, the effect of the diffusion tensor is to remove diffusive flux in the y-direction, and this is observed as the interface is unable to relax to a flat state. Once the interface waves become large enough, convection increases the chemical potential in the areas bounded by walls and the interface begins to move as a whole. As the interface moves away from the inlet end of the channel convection is more able to transport chemical potential and the interface relaxes somewhat.

In the literature the problem was studied with an initially perturbed interface, and so we set up the same case, perturbing the straight interface with a

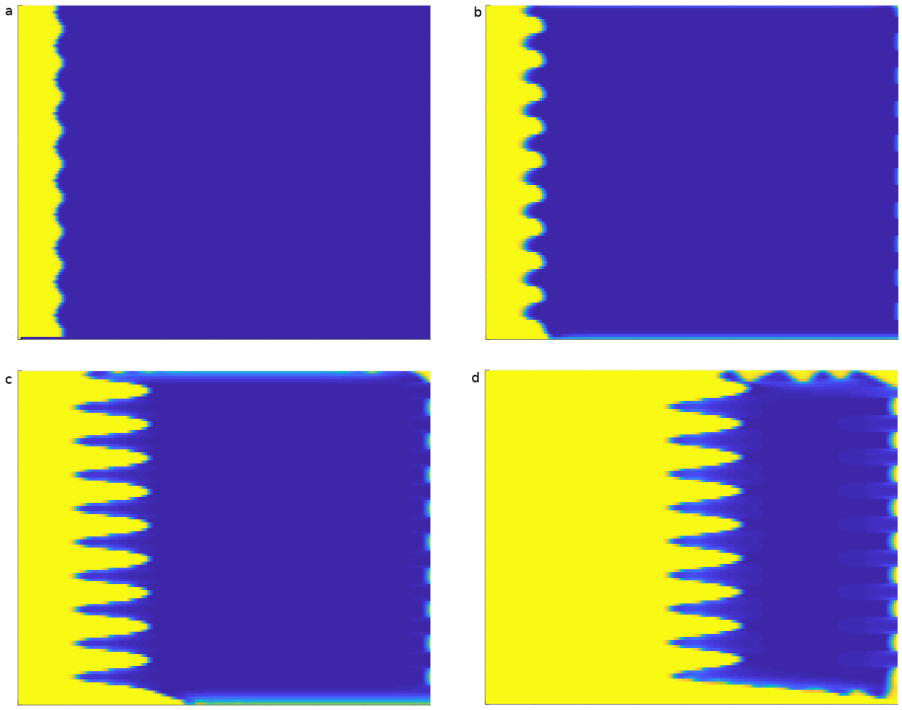

Figure 4.5: Evolution of a sinusoidally perturbed interface according to the Upscaled phase-field model, $\theta_0 = \frac{\pi}{2}$, Cn $= \frac{1}{240}$. Panels show phase-field over time: a) Initially $t = 0s$, b) After 2 timesteps $t = 20s$, c) after 10 steps $t = 100s$, d) after 20 steps $t = 320s$. Mesh is a regular rectangular mesh, with 200x120 elements

sinusoidal component. The evolution of this interface is shown in Figure 4.5:

In this case we observe that the initially perturbed interface is rapidly deformed from its sinusoidal shape due to the initial chemical potential, but subsequently returns to a sinusoidal profile before being transported along the channel as before.

We observe that the convection is the only term that allows flow in the y-direction is therefore responsible for the motion of the interface in regions where no flow occurs at the inlet of the channel. In order to visualise this and confirm that this is the case we plot the largest contribution to the phase. In the Figure 4.6 we see that in regions where the inlet allows flow the diffusive flux is dominant, in regions where the inlet is plugged we see that convection is dominant. In the vicinity of the interface the picture is more complex, and in general the diffusion is stronger, this is likely due to the larger magnitude of D_{11} versus C_{11} for this microscale geometry.

In both cases we observe nucleation along the walls, initially in the top

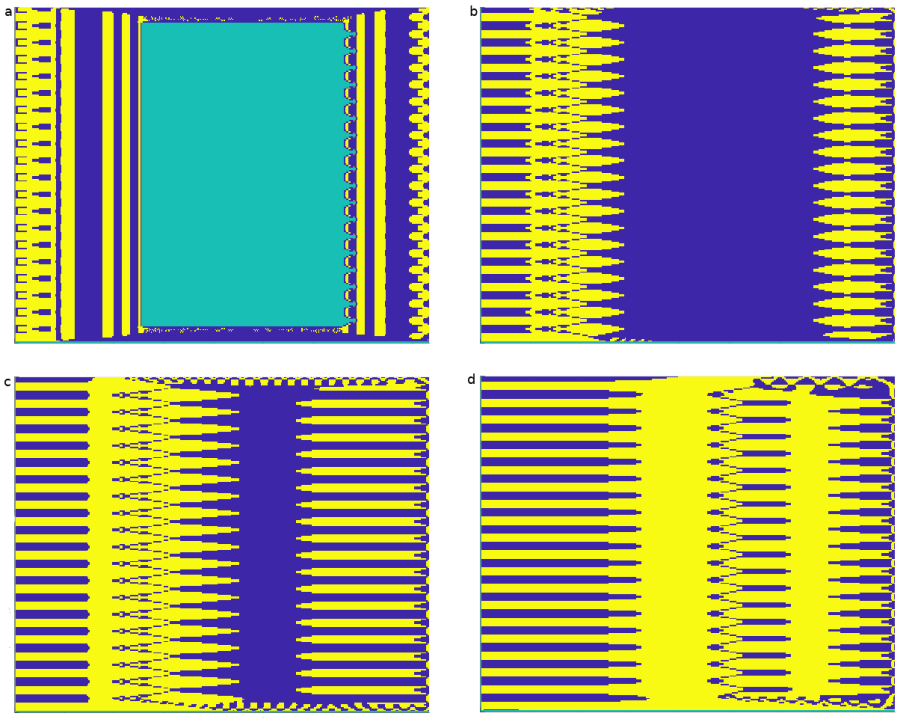

Figure 4.6: Largest contribution to phase evolution, yellow indicated diffusive flux is dominant and blue indicates that convective flux is dominant. Panels show dominant flux: a Initially $t = 0s$, b After 10 timesteps $t = 100s$, c after 20 steps $t = 200s$, d after 50 steps $t = 500s$. Mesh is a regular rectangular mesh, with 400x240 elements

right corner and then in droplets all along the top and bottom walls. We suggest that this is due to steadily increasing chemical potential throughout the channel interacting with the wetting boundary conditions on the wall promoting nucleation, but this is undetermined at present.

4.5 Conclusions and Future Work

We investigated a model for two phase flow in porous media, we assumed that the medium consisted of a periodic pore which tiled the whole macroscale geometry. Under these assumptions we adopted a convective Cahn–Hilliard approach to model the fluid flow. We made use of the machinery of homogenisation to decouple the microscale and macroscale and to derive an upscaled equation describing the average flow. In this model we obtained tensors describing the influence of the microscopic geometry on the flow.

We formulated a finite-element model for these equations, solving for the cell corrector field and the Stokes' flow field a representative microscopic geometry, this compared well in appearence with literature results. We were also able to compute these fields for other geometries that might be of interest, and we presented results for an inkbottle geometry. At this stage we were unable to reproduce the numerical values of the tensors reported in literature, and this is a work in progress at this time.

We attempted to use our finite-element formulation for the upscaled equation but were unable to achieve convergence within the limitations of the present work; in order to confirm that the model is stable for longer times we adopted a simple finite-difference method. Using this approach we confirmed that the observed behaviour in literature, that of perturbations in the interface being stable, was observed for longer times. We also confirmed that in the absence of diffusion in the cross-stream direction is balanced by the convection term, which acts to transport chemical potential.

At this stage this project is still in progress, the outlook is good however, as there are many open questions, initially we intend to investigate the effect of microscale geometry by changing the reference cell and investigating how the values of D and C are affected. The inverse problem is also of interest: given a target set of parameters can we produce a reference cell that matches, if this is possible then matching results with experiment would become much easier.

Beyond a straight channel it would be worthwhile investigating how the microstructure affects flow in more complex geometries, as well as with different wetting properties in both the macroscale channel and the microscale pore geometry.

5

Conclusions and Outlook

We have studied three different problems using the machinery of multi-scale analysis; our general approach has been to address problems that have complex behaviour as a result of the interaction between scales, and we have applied different methods to treat the scale separation.

We began by investigating a problem that arises in various physical systems such as reaction rate theory: that of particles diffusing in an external potential under the influence of thermal noise. Much literature exists with analytical results and numerical simulations, and various statistics have been studied. We chose to study the invariant probability distribution which allowed us to find the locations where particles were most likely to be.

Existing literature suggested that thermal noise and microscopic fluctuations in the potential would interact and stabilise new states, but this had not been investigated for asymmetric potentials. The appeal of this modification was that it would enable description of reaction systems where the equilibrium was not exactly central, which is a very unlikely situation for physical systems.

Through the use of Homogenisation we were able to describe the steady-state behaviour of the system using only the macro-scale. We found that we could directly apply literature results to the problem, and this enabled us to determine that an additional stable state was induced. Describing the system with the framework of Bifurcation Analysis we determined that the noise controlled transition from an Imperfect Supercritical Pitchfork Bifurcation to a Subcritical one.

In the limit of small tilt we recovered the literature result for the symmetric case and showed that the tilt has the effect of destabilising the additional state. Indeed with numerical continuation we showed that there exists a critical noise value that depends on the tilt for which the transition no longer happens.

Using terminology from Phase Transition Theory we determined that the system undergoes a first-order phase transition with a critical exponent of $\gamma \approxeq 0.66$. This extends results in literature for the symmetric case, where in [53] the

authors find that $\gamma \approxeq 1.6$ regardless of the number of microscales. This value was found to be insensitive to the magnitude of the tilt, suggesting that the difference was due to the presence of an asymmetry rather than its magnitude.

There exist several open questions with this model which would warrant further study:

1. The author expended some energy to obtaining an analytical expression for the effect of the tilt on the critical noise but was unable to do so. This would be a valuable result.

2. Existing results for the effect of multiple micro-scales in [53] could be directly applied, this would also be a valuable extension to the present work.

3. Restrictions on the form of the potential are reasonably light, other types of confined potential could be studied without much extra work.

4. Extension of the present results to three or more dimensions is also possible, the equations to be solved in the homogenisation process lend themselves to separable potentials quite straightforwardly. In the more general case the cell equation must be solved numerically, but the wider applicability of more complex potentials would render the effort worthwhile.

We subsequently studied two different problems involving multi-phase flow: these types of flow are characterised by complex dynamics and multiple competing effects. Particular problems are encountered when looking at interfacial flows in confinement, where care must be taken to accurately describe contact-line motion.

In Chapter 3 we analysed a flow relevant to microfluidic separators: a fluid was quenched within a corrugated channel and allowed to nucleate, before force was applied inducing flow. We looked to investigate the effect of the channel geometry and the wetting properties of the confining walls on the flow morphology.

We adopted a two-pronged approach, building a static model for interfacial energy and performing numerical simulations of the Cahn–Hilliard-Navier–Stokes equations. Considering each of the likely flow morphologies in turn we derived expressions for the interfacial energy and thus the likelihood of observing each.

The behaviours of droplet flow and stratified flow were described straightforwardly but slug flow presented much richer behaviour. Numerical continuation was used to solve the nonlinear equation describing the interface shape, and a first-order phase transition was observed. Large perturbations in the channel width admitted multiple configurations with equal volume, two low energy states corresponding to concave and convex interfaces and a higher energy unstable state in which the interface was flat.

The presence of this phase transition indicated that slug motion would transition from continuous, when the corrugation was small, to discontinuous jumping

motion when the walls were more corrugated. We found that the critical value of the corrugation was approximately 0.71 and confirmed this with two-parameter continuation.

By computing the interface lengths for different centres of mass we found the interfacial energy at each point. Comparing these energy values with those for droplet and stratified flow with equal volume we produced a parameter map in $V - \varepsilon$ space. Physical arguments separate the space into regions where only plug flow was possible, a region where only droplet flow was possible, and a region where either were possible depending on the precise values of V and ε.

Subsequent numerical computations using a Finite-Element formulation yielded flows in each of the expected morphologies. Unfortunately the final state proved to be very dependent on the initial conditions, which we took to be random, and therefore we were unable to draw conclusions about the accuracy of our energy model. It seems likely that statistical analysis of the effect of initial conditions will be needed to validate the parameter map we developed.

This chapter offers promising areas for future work:

1. A statistical analysis of the mapping between initial state and final state would offer a way to validate the energy analysis

2. Dimensional analysis of the energy model we developed could be used to compare the magnitude of the interfacial energy barrier with the flow forcing, this could enable prediction of regimes in which slugs become pinned.

3. Numerical simulations produced configurations that we did not consider in the static analysis, such as multiple droplets. Adding these would be straightforward, indeed we predicted the need for this when we found a region in parameter space where neither slug flow nor droplet flow were feasible.

4. Modification of the geometry would be a simple extension, either by moving the two walls out of phase with each other, or by changing the wavenumber of one relative to the other. In this way it might be possible to select for specific droplet sizes.

5. Once the implications of the geometry and contact angle on the morphology are understood it would be possible to extend the model to account for two different fluids, or a fluid and a solute. This would be a much more industrially relevant model.

Chapter 4 gave an introduction to a work that is currently in progress, we motivated the study of porous media flows with industrial applications and presented an upscaling approach to separate the dominant scales. This resulted in three separate problems to solve in order to model the interfacial flow, but the only connection between the dominant scales was through constant tensors.

We formulated a Finite-Element model for the system which we aimed to solve using open-source software, but as of writing we have been unable to

achieve success. Instead we presented validation of literature simulations for longer times using a Finite-Difference scheme. We confirmed that the model was robust and that the behaviour observed at the interface was not transient.

Some areas for further study of this problem include:

1. Full finite-element implementation for the model will allow complex geometries to be studied, offering more scope for experimental validation.

2. Computation of the tensors D and C for other microscopic geometries will permit comparison of different pore geometries, as well as possibly solving the inverse problem to predict pore geometries from tensor values.

3. Extending this model to three dimensions is fairly straightforward and would offer further applications and opportunities for comparison with experiment.

In general the field of multiscale methods is ripe for further study, the possible gains for success are huge: from acceleration of fluid simulation to direct coupling of molecular dynamics to macroscale descriptions. Industrially relevant problems are currently insoluble in reasonable time due to the limitations of microscale behaviour. Further progress in averaging, homogenisation or upscaling will hopefully lead to these kinds of problems becoming soluble.

Bibliography

[1] Abels, H. On a Diffuse Interface Model for Two-Phase Flows of Viscous, Incompressible Fluids with Matched Densities. *Archive for Rational Mechanics and Analysis 194*, 2 (nov 2009), 463–506.

[2] Aland, S., and Voigt, A. Benchmark computations of diffuse interface models for two-dimensional bubble dynamics. *International Journal for Numerical Methods in Fluids 69*, 3 (may 2012), 747–761.

[3] Allaire, G. Homogenization and Two-Scale Convergence. *SIAM Journal on Mathematical Analysis 23*, 6 (1992), 1482–1518.

[4] Allgower, E., and Georg, K. *Introduction to Numerical Continuation Methods*. John Wiley & Sons, New York, 1979.

[5] Alnæs, M. S., Blechta, J., Hake, J., Johansson, A., Kehlet, B., Logg, A., Richardson, C., Ring, J., Rognes, M. E., and Wells, G. N. The FEniCS Project Version 1.5. *Archive of Numerical Software 3*, 100 (2015), 9–23.

[6] Ambegaokar, V., and Halperin, B. Voltage due to thermal noise in the dc Josephson effect. *Physical Review Letters 22*, 25 (1969), 1364–1366.

[7] Anderson, J. Ludwig Prandtl's Boundary Layer. *Physics Today 58*, 12 (2005), 42–48.

[8] Andreoni, W., Curioni, A., and Mordasini, T. DFT-based molecular dynamics as a new tool for computational biology: first applications and perspective. *IBM journal of research and development 45*, 3/4 (2001), 397–407.

[9] AURIAULT, J.-L., AND LEWANDOWSKA, J. Effective Diffusion Coefficient: From Homogenization to Experiment. *Transport in Porous Media 27*, 2 (1997), 205–223.

[10] AYMARD, B., VAES, U., PRADAS, M., AND KALLIADASIS, S. A linear, second-order, energy stable, fully adaptive finite element method for phase-field modelling of wetting phenomena. *Journal of Computational Physics: X 2* (mar 2019), 100010.

[11] AZENCOTT, R., BERI, A., JAIN, A., AND TIMOFEYEV, I. Sub-sampling and parametric estimation for multiscale dynamics. *Communications in Mathematical Sciences 11*, 4 (2013), 939–970.

[12] BARRETT, J. J. W., BLOWEY, J. J. F., AND GARCKE, H. Finite Element Approximation of the Cahn–Hilliard Equation with Degenerate Mobility. *SIAM Journal on Numerical Analysis 37*, 1 (jan 1999), 286–318.

[13] BARRETT, J. W., AND BLOWEY, J. F. Finite element approximation of the Cahn-Hilliard equation with concentration dependent mobility. *Mathematics of Computation 68*, 226 (apr 1999), 487–518.

[14] BASTÚS, N. G., COMENGE, J., AND PUNTES, V. Kinetically Controlled Seeded Growth Synthesis of Citrate-Stabilized Gold Nanoparticles of up to 200 nm: Size Focusing versus Ostwald Ripening. *Langmuir 27*, 17 (sep 2011), 11098–11105.

[15] BEATSON, R., AND GREENGARD, L. A short course on fast multipole methods. Tech. rep., New York University, New York, 1997.

[16] BECKER, V., AND DÖRING, W. Kinetische Behandlung der Keimbildung in übersättigten Dämpfen. *Annalen der Physik 416*, 8 (1935), 719–752.

[17] BENDER, C., AND ORSZAG, S. *Advanced Mathematical Methods for Scientists I - Asymptotic Methods and Perturbation Theory*, 2 ed. Springer-Verlag New York, New York, 1999.

[18] BENSOUSSAN, A., LIONS, J.-L., AND PAPANICOLAOU, G. *Asymptotic Analysis of Periodic Structures*, 1st ed. North-Holland Publishing Company, Amsterdam, 1978.

[19] BIRD, R. Kinetic Theory and Constitutive Equations for Polymeric Liquids. *Journal of Rheology 26*, 3 (1982), 277–299.

[20] BLOWEY, J., AND ELLIOTT, C. The Cahn-Hilliard gradient theory for separation with non-smooth free energy Part II: Numerical analysis. *Euro. Jnl of Applied Mathematics 3* (1992), 147–149.

[21] BLOWEY, J. F., AND ELLIOTT, C. M. The Cahn-Hilliard gradient theory for phase separation with non-smooth free energy Part I: Mathematical analysis. *Euro. Jnl of Applied Mathematics 2* (1991), 233–279.

[22] Bonifacio, R., and Lugiato, L. Photon Statistics and Spectrum of Transmitted Light in Optical Bistability. *Physical Review Letters 40*, 15 (1978), 1023–1027.

[23] Bonn, D., Eggers, J., Indekeu, J., and Meunier, J. Wetting and spreading. *Reviews of Modern Physics 81*, 2 (2009), 739–805.

[24] Boyer, F., and Lapuerta, C. Study of a three component Cahn-Hilliard flow model. *Mathematical Modelling and Numerical Analysis 40*, 4 (jul 2006), 653–687.

[25] Boyer, F., Lapuerta, C., Minjeaud, S., Piar, B., and Quintard, M. Cahn–Hilliard/Navier–Stokes Model for the Simulation of Three-Phase Flows. *Transport in Porous Media 82*, 3 (apr 2010), 463–483.

[26] Briggs, W., Henson, V., and McCormick, S. *A Multigrid Tutorial*, 2 ed. Society for Industrial and Applied Mathematics, Philadelphia, 2000.

[27] Cahn, J. W. Free Energy of a Nonuniform System. II. Thermodynamic Basis. *The Journal of Chemical Physics 30*, 5 (may 1959), 1121–1124.

[28] Cahn, J. W., Elliott, C. M., and Novick-Cohen, A. The Cahn–Hilliard equation with a concentration dependent mobility: motion by minus the Laplacian of the mean curvature. *European Journal of Applied Mathematics 7*, 03 (jun 1996), 287–301.

[29] Cahn, J. W., and Hilliard, J. E. Free Energy of a Nonuniform System. I. Interfacial Free Energy. *The Journal of Chemical Physics 28*, 2 (feb 1958), 258–267.

[30] Cahn, J. W., and Hilliard, J. E. Free Energy of a Nonuniform System. III. Nucleation in a Two-Component Incompressible Fluid. *The Journal of Chemical Physics 31*, 3 (sep 1959), 688–699.

[31] Car, R., and Parrinello, M. Unified approach for molecular dynamics and density-functional theory. *Physical Review Letters 55*, 22 (1985), 2471–2474.

[32] Carlsson, T. *Brownian Dynamics Simulations of Macromolecules*. Phd, Uppsala University, 2012.

[33] Caroli, B., Caroli, C., and Roulet, B. Diffusion in a bistable potential: A systematic WKB treatment. *Journal of Statistical Physics 21*, 4 (1979), 415–437.

[34] Caroli, B., Caroli, C., and Roulet, B. Diffusion in a bistable potential: The functional integral approach. *Journal of Statistical Physics 26*, 1 (1981), 83–111.

[35] Ceniceros, H., and Roma, A. A nonstiff, adaptive mesh refinement-based method for the Cahn-Hilliard equation. *Journal of Computational Physics 225* (2007), 1849–1862.

[36] Challis, K. J., and Jack, M. Tight-binding approach to overdamped Brownian motion on a multidimensional tilted periodic potential. *Physical Review E 87*, 5 (2013), 052102.

[37] Chella, R., and Vinals, J. Mixing of a Two-phase Fluid by Cavity Flow. *Physical Review E, Statistical Physics, Plasmas, Fluids, and Related Interdisciplinary Topics 53*, 4 (1996), 3832–3840.

[38] Cholewa, J., and Dlotko, T. GLOBAL ATTRACTOR FOR THE CAHN-HILLIARD SYSTEM. *Bull. Austral. Math. Soc. 49* (1994), 277–292.

[39] Chorin, A. A Numerical Method for Solving Incompressible Viscous Flow Problems. *Journal of Computational Physics 2*, 1 (1967), 12–26.

[40] Chorin, A. J. Numerical solution of the Navier-Stokes equations. *Mathematics of Computation 22*, 104 (1968), 745–745.

[41] Chupin, L. Existence result for a mixture of non Newtonian flows with stress diffusion using the Cahn-Hilliard formulation. *Discrete and Continuous Dynamical Systems - Series B 3*, 1 (nov 2003), 45–68.

[42] Colli, P., Farshbaf-Shaker, M. H., Gilardi, G., and Sprekels, J. Optimal Boundary Control of a Viscous Cahn–Hilliard System with Dynamic Boundary Condition and Double Obstacle Potentials. *SIAM Journal on Control and Optimization 53*, 4 (jan 2015), 2696–2721.

[43] Colli, P., Gilardi, G., and Hilhorst, D. On a Cahn-Hilliard type phase field system related to tumor growth. *Discrete and Continuous Dynamical Systems 35*, 6 (dec 2014), 2423–2442.

[44] Colli, P., Gilardi, G., Rocca, E., and Sprekels, J. Optimal distributed control of a diffuse interface model of tumor growth. *Nonlinearity 30* (2017), 2518–2546.

[45] Colli, P., Gilardi G., and Sprekels, J. Optimal velocity control of a convective Cahn-Hilliard system with double obstacles and dynamic boundary conditions: A 'deep quench' approach. *Journal of Convex Analysis 26*, 2 (2019), 485–514.

[46] Dai, S., and Du, Q. Weak Solutions for the Cahn-Hilliard Equation with Degenerate Mobility. *Arch. Rational Mech. Anal 219*, 3 (mar 2016), 1161–1184.

[47] Das, A., and Schwendimann, P. Fokker-Planck Equation for a Periodic Potential. *Physica A 89*, 3 (1977), 605–612.

[48] de Chalendar, J. A., Garing, C., and Benson, S. M. Pore-scale Considerations on Ostwald Ripening in Rocks. *Energy Procedia 114* (jul 2017), 4857–4864.

[49] Dieterich, W., Peschel, I., and Schneider, W. Diffusion in Periodic Potentials. *Zeitschrift für Physik B 27*, 2 (1977), 177–187.

[50] Ding, H., Gilani, M., and Spelt, P. Sliding, pinch-off and detachment of a droplet on a wall in shear flow. *Journal of Fluid Mechanics 644* (2010), 217–244.

[51] Dlotko, T. Golbal Attractor for the Cahn-Hilliard Equation in H2 and H3. *Journal of Differential Equations 113* (1994), 381–393.

[52] Doedel, E. J., Fairgrieve, T. F., Sandstede, B., Champneys, A. R., Kuznetsov, Y. A., and Wang, X. Auto-07p: Continuation and bifurcation software for ordinary differential equations. Tech. rep., 2007.

[53] Duncan, A. B., Kalliadasis, S., Pavliotis, G. A., and Pradas, M. Noise-induced transitions in rugged energy landscapes. *Physical Review E 94*, 3 (sep 2016), 032107.

[54] E, W. *Principles of Multiscale Modeling*, 1 ed. Cambridge University Press, Cambridge UK, 2011.

[55] E, W., and Vanden-Eijnden, E. Some Critical Issues for the "Equation-Free" Approach to Multiscale Modeling, 2008.

[56] Eden, A., and Kalantarov, V. 3D convective Cahn–Hilliard equation. *Communications on Pure & Applied Analysis 6*, 4 (2007), 1075–1086.

[57] Eden, A., and Kalantarov, V. K. The convective Cahn-Hilliard equation. *Applied Mathematics Letters 20* (2007), 455–461.

[58] Elliott, C., and Luckhaus, S. A generalized diffusion equation for phase separation of a multicomponent mixture with interfacial energy. 1991.

[59] Elliott, C. M., French, D. A., and Milner, F. A. A second order splitting method for the Cahn-Hilliard equation. *Numerische Mathematik 54*, 5 (sep 1989), 575–590.

[60] Elliott, C. M., and Garcke, H. On the Cahn–Hilliard Equation with Degenerate Mobility. *SIAM Journal on Mathematical Analysis 27*, 2 (mar 1996), 404–423.

[61] Elliott, C. M., and Garcke, H. Diffusional phase transitions in multicomponent systems with a concentration dependent mobility matrix. *Physica D: Nonlinear Phenomena 109*, 3-4 (nov 1997), 242–256.

[62] Elliott, C. M., and Mikelić, A. Existence for the Cahn-Hilliard phase separation model with a nondifferentiable energy. *Annali di Matematica Pura ed Applicata 158*, 1 (dec 1991), 181–203.

[63] Elliott, C. M., and Songmu, Z. On the Cahn-Hilliard equation. *Archive for Rational Mechanics and Analysis 96*, 4 (dec 1986), 339–357.

[64] Euler, L. Quantum motus terrae e lune perturbetur accuratis inquiritur. *Novi Commentarii Academiae Scientiarum Petropolitanae 1*, 1 (1750), 428–443.

[65] Farkas, L. Keimbildungsgeschwindigkeit in übersättigten Dämpfen. *Zeitschr. f. phys. Chemie 125* (1927), 236–242.

[66] Feng, X., Kou, J., and Sun, S. A Novel Energy Stable Numerical Scheme for Navier-Stokes-Cahn-Hilliard Two-Phase Flow Model with Variable Densities and Viscosities. In *Lecture Notes in Computer Science (including subseries Lecture Notes in Artificial Intelligence and Lecture Notes in Bioinformatics)* (2018), Y. et al. Shi, Ed., vol. 10862 LNCS, Springer, Cham, pp. 113–128.

[67] Festa, R., and D'Agliano, E. Diffusion coefficient for a Brownian particle in a periodic field of force. *Physica A 90*, 2 (1978), 229–244.

[68] Frigeri, S., Gal, C. G., Grasselli, M., and Sprekels, J. Two-dimensional nonlocal Cahn-Hilliard-Navier-Stokes systems with variable viscosity, degenerate mobility and singular potential. *Nonlinearity 32*, 2 (feb 2019), 678.

[69] Fulde, P., Pietronero, L., Schneider, W., and Strässler, S. Problem of Brownian Motion in a Periodic Potential. *Physical Review Letters 35*, 26 (1975), 1776–1779.

[70] Gal, C., and Wu, H. Asymptotic behavior of a Cahn-Hilliard equation with Wentzell boundary conditions and mass conservation. *Discrete and Continuous Dynamical Systems 22*, 4 (sep 2008), 1041–1063.

[71] Gal, C. G. A Cahn–Hilliard model in bounded domains with permeable walls. *Mathematical Methods in the Applied Sciences 29*, 17 (nov 2006), 2009–2036.

[72] Gal, C. G., and Grasselli, M. Asymptotic behavior of a Cahn–Hilliard–Navier–Stokes system in 2D. *Annales de l'Institut Henri Poincare (C) Non Linear Analysis 27*, 1 (jan 2010), 401–436.

[73] Gal, C. G., Grasselli, M., and Miranville, A. Cahn-Hilliard-Navier-Stokes systems with moving contact lines. *Calculus of Variations and Partial Differential Equations 55*, 3 (jun 2016), 50.

[74] Garcke, H., and Lam, K. F. On a Cahn–Hilliard–Darcy System for Tumour Growth with Solution Dependent Source Terms. In *Trends in Applications of Mathematics to Mechanics*, E. Rocca, U. Stefanelli, L. Truskinovsky, and A. Visintin, Eds. Springer International Publishing, 2018, ch. 12, pp. 243–264.

[75] Gianozzi, P. DFT and Molecular Dynamics. In *Mettodo Numerici per la Struttura Elettronica - Lecture Notes*, 1 ed. Università di Udine, Udine, IT, 2012, ch. 6, pp. 34–42.

[76] Gidey, H., and Reddy, B. Operator-splitting methods for the 2D convective Cahn–Hilliard equation. *Computers & Mathematics with Applications* (feb 2019).

[77] Giga, M.-H., Giga, Y., and Saal, J. Self-Similar Solutions for Various Equations. In *Nonlinear Partial Differential Equations: Asymptotic Behaviour of Solutions and Self-Similar Solutions*, H. Brezis, Ed., 1 ed. Springer Science+Business Media, New York, 2010, ch. 3, p. 294.

[78] Golovin, A. A., Nepomnyashchy, A. A., Davis, S. H., and Zaks, M. A. Convective Cahn-Hilliard Models: From Coarsening to Roughening. *Physical Review Letters 86*, 8 (feb 2001), 1550–1553.

[79] González-Candela, E., and Romero-Rochín, V. Overdamped thermal ratchets in one and more dimensions. Kinesin transport and protein folding. *Physica A 372*, 2 (2006), 249–262.

[80] Grabert, H., Talkner, P., and Hänggi, P. Microdynamics and Time-Evolution of Macroscopic Non-Markovian Systems. *Zeitschrift für Physik 26*, 4 (1977), 389 –395.

[81] Grabert, H., Talkner, P., Hänggi, P., and Thomas, H. Microdynamies and Time-Evolution of Macroscopic Non-Markovian Systems. II. *Zeitschrift für Physik 29*, 3 (1978), 273–280.

[82] Guillén-González, F., and Tierra, G. On linear schemes for a Cahn–Hilliard diffuse interface model. *Journal of Computational Physics 234* (feb 2013), 140–171.

[83] Guillén-González, F., and Tierra, G. Second order schemes and time-step adaptivity for Allen–Cahn and Cahn–Hilliard models. *Computers & Mathematics with Applications 68*, 8 (oct 2014), 821–846.

[84] Gurtin, M. E. Generalized Ginzburg-Landau and Cahn-Hilliard equations based on a microforce balance. *Physica D: Nonlinear Phenomena 92*, 3-4 (may 1996), 178–192.

[85] Haasemann, G. Multi-Scale Modelling and Simulation of Textile Reinforced Materials. *Computers, Materials and Continua 1*, 1 (2005), 101–115.

[86] Haken, H. Cooperative phenomena in systems far from thermal equilibrium and and in nonphysical systems. *Reviews of Modern Physics 47*, 1 (1975), 67–121.

[87] Hänggi, P. On Derivations and Solutions of Master Equations and Asymptotic Representations. *Zeitschrift für Physik B 30*, 1 (1978), 85–95.

[88] Hänggi, P., and Marchesoni, F. Artificial Brownian motors: Controlling transport on the nanoscale. *Reviews of Modern Physics 81*, 1 (2009), 387–442.

[89] Hänggi, P., Talkner, P., and Borkovec, M. Reaction-rate theory: fifty years after Kramers. *Reviews of Modern Physics 62*, 2 (1990), 251–342.

[90] Hecht, F. New development in FreeFem++. *Journal of Numerical Mathematics 20*, 3-4 (2012), 251–266.

[91] Hinch, E. *Perturbation Methods*, 1 ed. Cambridge University Press, Cambridge UK, 1991.

[92] Hohenberg, P. C., and Halperin, B. I. Theory of dynamic critical phenomena. *Reviews of Modern Physics 49*, 3 (jul 1977), 435–479.

[93] Holmes, M. Matched Asymptotic Expansions. In *Introduction to Perturbation Methods*, 1 ed. Springer Science+Business Media, New York, 2013, ch. 2, pp. 57–137.

[94] Horsthemke, W., and Brenig, L. Non-Linear Fokker-Planck Equation as an Asymptotic Representation of the Master Equation. *Zeitschrift für Physik B 27*, 4 (1977), 341–348.

[95] Horstmeyer, M. Multiscale Modeling : A Review. In *Practical Aspects of Computational Chemistry*, J. Leszczynsk and M. Shukla, Eds., 1 ed. Springer Science+Business Media, New York, 2009, ch. 7, pp. 87–135.

[96] Hu, G., and Zheng, Q. The initial value problem of a Fokker-Planck equation with a bistable potential. *Physics Letters A 110*, 2 (1985), 68–72.

[97] Huang, J.-J., Huang, H., and Wang, X. Wetting boundary conditions in numerical simulation of binary fluids by using phase-field method: some comparative studies and new development. *International Journal for Numerical Methods in Fluids 77*, 3 (jan 2015), 123–158.

[98] Huh, C., and Scriven, L. Hydrodynamic model of steady movement of a solid/liquid/fluid contact line. *Journal of Colloid and Interface Science 35*, 1 (1971), 85–101.

[99] Hunter, J. Asymptotic Analysis and Singular Perturbation Theory - Lecture Notes. Tech. rep., University of California Davis, Davis, CA, 2004.

[100] Ianniruberto, G., Marrucci, G., and Hinch, E. Brownian dynamics of concentrated polymers in two dimensions. *Journal of Non-Newtonian Fluid Mechanics 76*, 1-3 (1998), 27–42.

[101] Jacqmin, D. Calculation of Two-Phase Navier–Stokes Flows Using Phase-Field Modeling. *Journal of Computational Physics 155*, 1 (oct 1999), 96–127.

[102] Jawson, M. Integral equation methods in potential theory. I. *Proceedings of the Royal Society A 275*, 1360 (1963), 23–32.

[103] Joseph, D. D. Fluid dynamics of two miscible liquids with diffusion and gradient stresses, 1990.

[104] Kalamkarov, A., Andrianov, I., and Danishevs'kyy, V. Asymptotic Homogenization of Composite Materials and Structures. *Applied Mechanics Reviews 62*, May 2009 (2009), 030802.

[105] Kalliadasis, S., Bielarz, C., and Homsy, G. Time-dependent free-surface thin film flows over topography. *Physics of Fluids 12*, 8 (2000), 1889–1898.

[106] Kay, D., and Welford, R. Efficient numerical solution of Cahn-Hilliard-Navier-Stokes fluids in 2D. *SIAM J. Sci. Comput. 29*, 6 (2007), 2241–2257.

[107] Kenmochi, N., Niezgodka, M., and Pawlow, I. Subdifferential Operator Approach to the Cahn-Hilliard Equation with Constraint. *Journal of Differential Equations 117*, 2 (apr 1995), 320–356.

[108] Kevrekidis, I., and Samaey, G. Equation-free multiscale computation: algorithms and applications. *Annual review of physical chemistry 60* (2009), 321–344.

[109] Kim, J. A continuous surface tension force formulation for diffuse-interface models. *Journal of Computational Physics 204*, 2 (apr 2005), 784–804.

[110] Kim, J. A numerical method for the Cahn–Hilliard equation with a variable mobility. *Communications in Nonlinear Science and Numerical Simulation 12*, 8 (dec 2007), 1560–1571.

[111] Kim, J. Phase field computations for ternary fluid flows. *Computer Methods in Applied Mechanics and Engineering 196*, 45-48 (sep 2007), 4779–4788.

[112] Kim, J. A generalized continuous surface tension force formulation for phase-field models for multi-component immiscible fluid flows. *Computer Methods in Applied Mechanics and Engineering 198*, 37-40 (aug 2009), 3105–3112.

[113] Kolmogorov, A. The Local Structure of Turbulence in Incompressible Viscous Fluid for Very Large Reynolds Numbers. *Dokl. Akad. Nauk SSSR 30*, 4 (1941).

[114] Kostianko, A., and Zelik, S. Inertial manifolds for the 3D Cahn-Hilliard equations with periodic boundary conditions. *Communications on Pure and Applied Analysis 14*, 5 (jun 2015), 2069–2094.

[115] Kostur, M., and Schimansky-Geier, L. Numerical study of diffusion induced transport in 2D systems. *Physics Letters A 265*, 5-6 (2000), 337–345.

[116] Kramers, H. Brownian motion in a field of force and the diffusion model of chemical reactions. *Physica 7*, 4 (1940), 284–304.

[117] Kruglov, V., Peacock, A., Dudley, J., and Harvey, J. Self-similar propagation of high-power parabolic pulses in optical fiber amplifiers. *Optics letters 25*, 24 (2000), 1753–1755.

[118] Kubo, R., Matsuo, K., and Kitahara, K. Fluctuation and Relaxation of Macrovariables. *Journal of Statistical Physics 9*, 1 (1973), 51–96.

[119] Lacasta, A., Sancho, J., Romero, A., Sokolov, I., and Lindenberg, K. From subdiffusion to superdiffusion of particles on solid surfaces. *Physical Review E 70* (2004), 1–10.

[120] Lagrange, J.-L. *Méchanique Analitique*, 1st ed. Jaques Gabay, Paris, 1788.

[121] Landauer, R. Fluctuations in Bistable Tunnel Diode Circuits. *Journal of Applied Physics 33*, 7 (1962), 2209–2216.

[122] Landauer, R., and Swanson, J. Frequency factors in the thermally activated process. *Physical Review 121*, 6 (1961), 1668–1674.

[123] Latorre, J., Pavliotis, G., and Kramer, P. Corrections to Einstein's Relation for Brownian Motion in a Tilted Periodic Potential. *Journal of Statistical Physics 150* (2013), 776–803.

[124] Lax, M. Fluctuations from the Nonequilibrium Steady State. *Reviews of Modern Physics 32*, 1 (1960), 25–64.

[125] Lee, D., Huh, J. Y., Jeong, D., Shin, J., Yun, A., and Kim, J. Physical, mathematical, and numerical derivations of the cahn-hilliard equation. *Computational Materials Science 81* (jan 2014), 216–225.

[126] Léger, S., Deteix, J., and Fortin, A. A Moore–Penrose continuation method based on a Schur complement approach for nonlinear finite element bifurcation problems. *Computers & Structures 152* (may 2015), 173–184.

[127] Lindner, B., Kostur, M., and Schimansky-Geier, L. OPTIMAL DIFFUSIVE TRANSPORT IN A TILTED PERIODIC POTENTIAL. *Fluctuation and Noise Letters 1*, 1 (2001), 15.

[128] Liu, C. On the convective Cahn–Hilliard equation with degenerate mobility. *Journal of Mathematical Analysis and Applications 344*, 1 (aug 2008), 124–144.

[129] Lowengrub, J., and Truskinovsky, L. Quasi–incompressible Cahn–Hilliard fluids and topological transitions. *Proceedings of the Royal Society of London. Series A: Mathematical, Physical and Engineering Sciences 454*, 1978 (oct 1998), 2617–2654.

[130] Matheson, I., Walls, D., and Gardiner, C. Stochastic models of firstorder nonequilibrium phase transitions in chemical reactions. *Journal of Statistical Physics 12*, 1 (1975), 21–34.

[131] Mielke, A., Ed. *Analysis, Modeling and Simulation of Multiscale Problems*, 1 ed. Springer Verlag, Heidelberg, 2006.

[132] Miranville, A., and Zelik, S. Robust exponential attractors for Cahn-Hilliard type equations with singular potentials. *Mathematical Methods in the Applied Sciences 27*, 5 (mar 2004), 545–582.

[133] Miranville, A., and Zelik, S. Exponential attractors for the Cahn-Hilliard equation with dynamic boundary conditions. *Mathematical Methods in the Applied Sciences 28*, 6 (apr 2005), 709–735.

[134] Moyal, J. Stochastic Processes and Statistical Physics. *Journal of the Royal Statistical Society. Series B 11*, 2 (1949), 150–210.

[135] Narayan, R., and Li, I. ADVECTION-DOMINATED ACCRETION: A SELF-SIMILAR SOLUTION. *The Astrophysical Journal 428* (1994), L13–L16.

[136] Naugolnykh, K. Nonlinear collapse of vortex. *Journal of the Acoustical Society of America 135*, 4 (2014), 2313.

[137] Nguetseng, G. A GENERAL CONVERGENCE RESULT RELATED TO THE THEORY OF HOMOGENIZATION. *SIAM Journal on Mathematical Analysis 20*, 3 (1989), 608–623.

[138] Nicolaenko, B., and Scheurer, B. Low dimensional behaviour of the pattern formation equations. In *Trends and practice of nonlinear analysis* (Amsterdam, 1985), V. Lakshmikantham, Ed., Elsevier Science Publishers b.v., pp. 323–336.

[139] Nicolaenko, B., Scheurer, B., and Temam, R. Some Global Dynamical Properties of a Class of Pattern Formation Equations. *Communications in Partial Differential Equations 14*, 2 (1987), 245–297.

[140] Nitzan, A., Ortoleva, P., Deutch, J., and Ross, J. Fluctuations and transitions at chemical instabilities: The analogy to phase transitions. *The Journal of Chemical Physics 61*, 3 (1974), 1056–1074.

[141] Novick-Cohen, A. On the viscous Cahn-Hilliard equation. In *Material instabilities in continuum and related problems*, J.M. Ball, Ed. Oxford University Press, Oxford, 1988, pp. 329–342.

[142] Novick-Cohen, A. Chapter 4 The Cahn–Hilliard Equation. *Handbook of Differential Equations: Evolutionary Equations 4* (jan 2008), 201–228.

[143] Novick-Cohen, A., and Segel, L. A. Nonlinear aspects of the Cahn-Hilliard equation. *Physica D: Nonlinear Phenomena 10*, 3 (mar 1984), 277–298.

[144] Of, G. An Introduction to Fast Multipole Boundary Element Methods. Tech. rep., Graz University of Technology, Ostrava, 2012.

[145] Olla, S. Homogenization of Diffusion Processes in Random Fields, 1994.

[146] Olver, F., Olde Daalhuis, A., Lozier, D., Schneider, B., Boisvert, R., Clark, C., Miller, B., Saunders, B., Cohl, H., and McClain, M. NIST Digital Library of Mathematical Functions. http://dlmf.nist.gov/, Release 1.0.25 of 2019-12-15.

[147] Papanicolaou, G. Diffusion in Random Media. In *Surveys in Applied Mathematics* (1995), G. Papanicolaou, Ed., Plenum Press, pp. 205–255.

[148] Pavliotis, G. A multiscale approach to Brownian motors. *Physics Letters, Section A: General, Atomic and Solid State Physics 344* (2005), 331–345.

[149] Pavliotis, G., and Stuart, A. *Multiscale Methods: Averaging and Homogenization*, 1 ed. Springer Science+Business Media, New York, 2008.

[150] Pontryagin, L., Andronov, A., and Vitt, A. On the statistical treatment of dynamical systems. *Zh. Eksp. Teor. Fiz. 3* (1933), 165–180.

[151] Prüss, J., Racke, R., and Zheng, S. Maximal regularity and asymptotic behavior of solutions for the Cahn–Hilliard equation with dynamic boundary conditions. *Annali di Matematica Pura ed Applicata 185*, 4 (oct 2006), 627–648.

[152] Racke, R., and Zheng, S. The Cahn-Hilliard equation with dynamic boundary conditions. *Advances in Differential Equations 8*, 1 (2003), 83–110.

[153] Rajagopal, A., Fischer, P., Kuhl, E., and Steinmann, P. Natural element analysis of the Cahn–Hilliard phase-field model. *Computational Mechanics 46*, 3 (aug 2010), 471–493.

[154] Ratke, L., and Voorhees, P. W. Growth and coarsening: Ostwald ripening in materials processing. *Choice Reviews Online 39*, 11 (2013), 39–6445–39–6445.

[155] Risken, H. Distribution- and correlation- functions for a Laser Amplitude. *Zeitschrift für Physik 186*, 1 (1965), 85–98.

[156] Risken, H. Correlation Function of the Amplitude and of the Intensity Fluctuation for a Laser Model near Threshold. *Zeitschrift für Physik 191*, 3 (1966), 302–312.

[157] Rowlinson, J., and Widom, B. *Molecular Theory of Capillarity*. Dover Publications, Mineola, New York, 1982.

[158] Roydhouse, M. D., Pradas, M., Al-Rifai, N., Azizi, B., Cao, E., Kalliadasis, S., and Gavriilidis, A. Operating ranges of gas–liquid capillary microseparators: Experiments and theory. *Chemical Engineering Science 114* (jul 2014), 30–39.

[159] Sanders, J., Verhulst, F., and Murdock, J. The History of the Theory of Averaging. In *Averaging Methods in Nonlinear Dynamical Systems*, 2nd ed. Springer Science+Business Media, New York, 2007, ch. Appendix A, pp. 337–343.

[160] Schmuck, M., Pradas, M., Pavliotis, G. A., and Kalliadasis, S. Upscaled phase-field models for interfacial dynamics in strongly heterogeneous domains. *Proceedings of the Royal Society A: Mathematical, Physical and Engineering Sciences 468*, 2147 (2012), 3705–3724.

[161] Schmuck, M., Pradas, M., Pavliotis, G. A., and Kalliadasis, S. Derivation of effective macroscopic Stokes-Cahn-Hilliard equations for periodic immiscible flows in porous media. *Nonlinearity 26* (2013), 3259–3277.

[162] Schwörer, M., Lorenzen, K., Mathias, G., and Tavan, P. Utilizing fast multipole expansions for efficient and accurate quantum-classical molecular dynamics simulations. *The Journal of Chemical Physics 142*, 10 (2015), 104108.

[163] Sibley, D., Nold, A., and Kalliadasis, S. The asymptotics of the moving contact line : cracking an old nut. *Journal of Fluid Mechanics 764* (2015), 445–462.

[164] Sibley, D., Nold, A., Savva, N., and Kalliadasis, S. On the moving contact line singularity: Asymptotics of a diffuse-interface model. *European Physical Journal E 36*, 3 (2013), 7.

[165] Songmu, Z. Asymptotic behavior of solution to the Cahn-Hillard equation. *Applicable Analysis 23*, 3 (dec 1986), 165–184.

[166] Steefel, C. I., and Van Cappellen, P. A new kinetic approach to modeling water-rock interaction: The role of nucleation, precursors, and Ostwald ripening. *Geochimica et Cosmochimica Acta 54*, 10 (oct 1990), 2657–2677.

[167] Suzuki, M. Scaling Theory of Transient Phenomena Near the Instability Point. *Journal of Statistical Physics 16*, 1 (1977), 11–32.

[168] Swanson, J. Physical versus Logical Coupling in Memory Systems. *IBM Journal of Research and Development 4*, 3 (1960), 305–310.

[169] Thiele, U., and Knobloch, E. Thin liquid films on a slightly inclined heated plate. *Physica D: Nonlinear Phenomena 190*, 3-4 (apr 2004), 213–248.

[170] Tierra, G., and Guillén-González, F. Numerical Methods for Solving the Cahn–Hilliard Equation and Its Applicability to Related Energy-Based Models. *Archives of Computational Methods in Engineering 22*, 2 (apr 2015), 269–289.

[171] Tremaine, S. On the Origin of Irregular Structure in Saturn's Rings. *The Astronomical Journal 125*, 2 (feb 2003), 894–901.

[172] Van Kampen, N. A power series expansion o f the master equation. *Canadian Journal of Physics 39*, 1960 (1961), 551–567.

[173] Verlarde, M. e. Discussion and Debate: Wetting and Spreading Science - quo vadis? *European Physical Journal: Special Topics 197* (2011), 345.

[174] Vetter, T., Iggland, M., Ochsenbein, D. R., Hänseler, F. S., and Mazzotti, M. Modeling Nucleation, Growth, and Ostwald Ripening in Crystallization Processes: A Comparison between Population Balance and Kinetic Rate Equation. *Crystal Growth & Design 13*, 11 (nov 2013), 4890–4905.

[175] Wang, Y., Wang, Q., Deng, X., Xia, Z., Yan, J., and Xu, H. Graphics processing unit (GPU) accelerated fast multipole BEM with level-skip M2L for 3D elasticity problems. *Advances in Engineering Software 82* (2015), 105–118.

[176] Watson, S. J., Otto, F., Rubinstein, B. Y., and Davis, S. H. Coarsening dynamics of the convective Cahn-Hilliard equation. *Physica D: Nonlinear Phenomena* (2003).

[177] Weaver, D. Effective diffusion coefficient of a Brownian particle in a periodic potential. *Physica A: 98*, 1-2 (1979), 359–362.

[178] Weaver, D. Effective Diffusion Coefficient for Two-Dimensional Periodic Channels. *Physica A 128*, 3 (1984), 565–570.

[179] Weiss, U. Decay of Unstable States in Macroscopic Systems. *Physical Review A 25*, 4 (1982), 2444–2447.

[180] Wells, G. N., Kuhl, E., and Garikipati, K. A discontinuous Galerkin method for the Cahn–Hilliard equation. *Journal of Computational Physics 218*, 2 (nov 2006), 860–877.

[181] Wiesenfeld, K., Pierson, D., Pantazelou, E., Dames, C., and Moss, F. Stochastic resonance on a circle. *Physical Review Letters 72*, 14 (1994), 2125–2129.

[182] Wilkes, D., and Duncan, A. Acoustic coupled fluid–structure interactions using a unified fast multipole boundary element method. *The Journal of the Acoustical Society of America 137*, 4 (2015), 2158–2167.

[183] Wilson, C. Perturbations and solar tables from Lacaille to Delambre: the rapprochement of observation and theory, part I. *Archive for History of Exact Sciences 22*, 1-2 (1980), 53–188.

[184] Witelski, T. Equilibrium interface solutions of a degenerate singular Cahn-Hilliard equation. *Applied Mathematics Letters 11*, 5 (sep 1998), 127–133.

[185] Wu, H., and Zheng, S. Convergence to equilibrium for the Cahn–Hilliard equation with dynamic boundary conditions. *Journal of Differential Equations 204*, 2 (sep 2004), 511–531.

[186] Yatsyshin, P., and Morciano, M. Talk on Linking DDFT with MD simulations for the Moving Contact Line Problem, 2015.

[187] Yue, P., Feng, J., Liu, C., and Shen, J. A diffuse-interface method of simulating two-phase flows of complex fluids A diffuse-interface method for simulating two-phase flows of complex fluids. *Journal of Fluid Mechanics 515* (2004), 293–317.

[188] Zhao, L., Wu, H., and Huang, H. Convergence to equilibrium for a phase-field model for the mixture of two viscous incompressible fluids. *Communications in Mathematical Sciences 7*, 4 (2009), 939–962.

[189] Zhao, X. Fourier Spectral Approximation to Global Attractor for 2D Convective Cahn–Hilliard Equation. *Bulletin of the Malaysian Mathematical Sciences Society 41*, 2 (apr 2018), 1119–1138.

[190] Zwanzig, R. Effective Diffusion Coefficient for a Brownian Particle in Two-Dimensional Periodic Channel. *Physica A 117*, 1 (1983), 277–280.